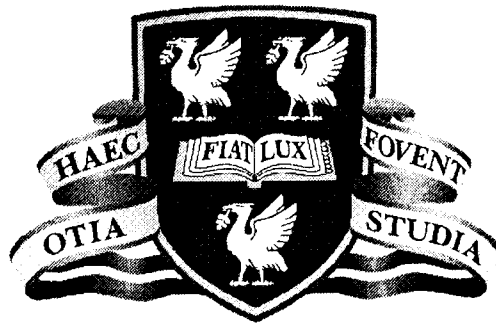# A Search for the Standard Model Higgs Boson in the neutrino channel using the DELPHI detector at LEP2

Thesis submitted in accordance with the requirements

of the University of Liverpool

for the degree of Doctor in Philosophy

by

Gavin James McPherson

September 1999

A Search for the Standard Model Higgs Boson in the neutrino channel using the DELPHI detector at LEP2

Gavin James McPherson

Abstract

A search for the Standard Model Higgs boson is performed using 51.6 pb^{-1} of data collected by the DELPHI detector in 1997 at a centre-of-mass energy of 183 GeV. A search is made for Higgs bosons produced in association with a Z boson, where the Higgs decays to b-quarks and the Z to neutrinos. Different statistical search methods are investigated and compared, with 95% confidence level cross-section limits set as a function of the Higgs boson mass. No significant excess is observed in the data, allowing a lower mass limit of 73.0 GeV/c^2 to be set for the Higgs boson.

Acknowledgements

I would like to offer my gratitude to Professors Paul Booth and Erwin Gabathuler for allowing me to carry out my Ph.D. at Liverpool, and for subsequent encouragement. I am grateful to my supervisor Dr. Leo Carroll for proof reading this thesis and his help with all the simple things that I insisted on making difficult.

Sincere thanks to my colleagues at CERN for patience in the face of persistent ignorance – particularly Reino Keranen, Duncan Reid, Bill Murray and Alex Read – and to Andre Augustinus for calm advice and an introduction to Stroopwafels.

Of my Liverpool colleagues, thanks go to Ali for putting up with *me* for three years, and to Chris Green, Ulrich Parzefall, Andy Galloni, Moshe Hanlon, Julia Cowell, Chris Anderson, Davy Milstead, Mike McAndrew and 18 Farmdale Close for – in various measure – help, fun, food and floorspace. I may have some things for which to thank Mark Smith, but the completion of this thesis is hardly one of them.

I am indebted to many others for essential distraction but I'd be astonished if they ever got around to reading about it. They'd have to learn to read for a start. Of you all, I particularly thank Jane and David Barney for making my visits to Geneva so comfortable.

Of those who will at least brave it as far as these acknowledgements, a huge "thank you" to Mum and Dad for everything.

Put most simply, science is a way of dealing with the world around us. It is a way of baffling the uninitiated with incomprehensible jargon. It is a way of obtaining fat government grants. It is a way of achieving mastery over the physical world by threatening it with destruction.

Science represents mankind's deepest aspirations - aspirations to power, to wealth, to the satisfaction of sheer animal lusts.

Tom Weller

Contents

List of Figures

List of Tables

Introduction

In the Standard Model of particle physics, the proposed solution for the generation of mass is through the *Higgs mechanism*, suggested by Peter Higgs in 1964 [1]. One prediction of this model is the existence of an as yet unobserved massive particle, the *Higgs boson*, which couples to particles according to their mass.

At the Large Electron-Positron (LEP) collider the Higgs boson (H) is expected to be produced via the process $e^+e^- \rightarrow Z^* \rightarrow HZ^0$. Since 1995, successive upgrades have allowed LEP to operate at higher collision energies; up to 200 GeV in 1999. Each advance in collision energy opens the search for the Higgs boson in an unexplored mass range, with the motivation of finding the last undiscovered particle to be predicted by the Standard Model.

The Higgs tends to decay to the heaviest particles permitted by kinematic constraints, which means a pair of b-quarks in the mass range accessible to LEP. This thesis describes a search for b quark jets from the Higgs boson, accompanied by missing energy from the decay of the associated Z boson to neutrinos ($H\nu\bar{\nu}$).

Chapter 1 provides the theoretical motivation for the Higgs boson search, along with a discussion of current limits. The LEP collider is introduced in Chapter 2, before a more detailed description of the components of the DELPHI detector relevant to the $H\nu\bar{\nu}$ search. Chapter 3 gives a brief introduction to the statistical methods used in a new particle search, and a motivation for the analysis method applied in this thesis. The data selection described in Chapter 4 provides data for the analysis techniques investigated in Chapter 5, from which a lower limit on the Higgs mass is derived in Chapter 6.

Chapter 1

Theory

All the fifty years of conscious brooding have brought me no closer to the answer to the question, 'What are light quanta?' Of course today every rascal thinks he knows the answer, but he is deluding himself

Albert Einstein (1951)

1.1 Introduction

This chapter presents a brief overview of the Standard Model of particle physics in § 1.2 before a motivation for the search for the Higgs particle; § 1.3 provides an introduction to the Higgs mechanism and § 1.4 a description of Higgs production and decay at LEP2. § 1.5 presents a summary of current theoretical and experimental bounds on the Higgs boson mass, m_H.

1.2 The Standard Model

Current understanding of elementary particle physics is supported by a canonical theory known as the Standard Model. This model developed out of many disparate strands of classical and early quantum physics, and as such is difficult to motivate in anything but the most advanced physics courses. Readers seeking an overview of the historical development should consult [2–4], while more comprehensive guides to the modern field theoretic approach are available in references [5–8]. For a thorough exposition of field theory, Hamiltonian mechanics and perturbation theory in the context of classical mechanics, see Goldstein [9].

2

The Standard Model describes the interaction between matter particles, or *fermions*, mediated by the exchange of force particles, or *gauge bosons*. Fermions are particles of half-integral spin (in units of $\hbar$) obeying Fermi-Dirac statistics, while bosons have integral spin and follow Bose-Einstein statistics. Fermions are divided into *quarks* and *leptons*: quarks come in 6 flavours (up (u), down (d), strange (s), charm (c), bottom (b) and top (t)), while the 6 leptons are the electron (e), muon (μ) and tau (τ) and their associated neutrinos (ν_e, ν_μ and ν_τ). The fermions are further divided into 3 *generations*, as shown in table 1.1

Fermions	Generation			Q	I_3^W	Y
	1	2	3			
Leptons	$\begin{pmatrix} \nu_e \\ e \end{pmatrix}_L$	$\begin{pmatrix} \nu_\mu \\ \mu \end{pmatrix}_L$	$\begin{pmatrix} \nu_\tau \\ \tau \end{pmatrix}_L$	$\begin{matrix}0 \\ -1\end{matrix}$	$\begin{matrix}+\frac{1}{2} \\ -\frac{1}{2}\end{matrix}$	-1
	e_R	μ_R	τ_R	-1	0	-2
Quarks	$\begin{pmatrix} u \\ d' \end{pmatrix}_L$	$\begin{pmatrix} c \\ s' \end{pmatrix}_L$	$\begin{pmatrix} t \\ b' \end{pmatrix}_L$	$\begin{matrix}+\frac{2}{3} \\ -\frac{1}{3}\end{matrix}$	$\begin{matrix}+\frac{1}{2} \\ -\frac{1}{2}\end{matrix}$	$\frac{1}{3}$
	u_R	c_R	t_R	$+\frac{2}{3}$	0	$+\frac{4}{3}$
	d'_R	s'_R	b'_R	$-\frac{1}{3}$	0	$-\frac{2}{3}$

Table 1.1: The elementary fermions and their electroweak quantum numbers, where Q is the charge, I_3^W is the third component of weak isospin and Y is the weak hypercharge. Subscripts L and R refer to left and right-handed helicity states, respectively.

Forces between fermions are mediated by gauge bosons: the photon γ, carrier of the *electromagnetic force*; the W^+, W^- and Z^0 which mediate the *weak interaction* and 8 gluons, g_i (i =1,8), which carry the *strong* or *colour* force. The gauge bosons and their properties are summarised in table 1.2. The postulated *graviton* – mediator of the gravitational force – is also included, although it has yet to be experimentally verified due to the relative weakness of gravity at the quantum scale. For the same reason, gravitational effects are negligible at the elementary particle level.

Interaction	Strong	Weak		Electromagnetic	Gravity
Gauge boson	gluon, $g_i(i = 1,8)$	$W^{\pm}$	Z^0	photon (γ)	graviton (?)
Mass (GeV/c^2)	0	80.35	91.19	0	0
Spin ($\hbar$)	1	1		1	2

Table 1.2: The gauge bosons

1.3 The Higgs Mechanism

The Standard Model is built on $SU(3)_C \otimes SU(2)_L \otimes U(1)_Y$ local gauge invariance, where C denotes colour, L refers to left-handed helicity states and Y is the weak hypercharge. Each symmetry introduces an interaction term into the Lagrangian, associated with a massless gauge boson. However, as table 1.2 shows, the weak $W^{\pm}$ and Z^0 bosons are far from massless. The mass can be put into the theory by hand, but at the expense of destroying gauge invariance. This is undesirable because gauge invariance ensures *perturbative renormalisability* of a theory: a feature which justifies the use of low order perturbative calculations in evaluating cross-sections. There is no overriding principle which demands that the physics of elementary particles be perturbatively calculable, however the success of this approach in QED led physicists to seek a model where gauge invariance and massive bosons could happily co-exist.

The solution was built on an analogy with solid state physics. It is a well known property of metals that in the presence of a magnetic potential $\vec{A}$, a current $\vec{j}_{sc}$ proportional to $\vec{A}$ develops near the surface of the metal:

$$\vec{j}_{sc} = \alpha^2 \vec{A} \tag{1.1}$$

This is known as the *screening current*, because its effect is to produce an opposing field, preventing $\vec{A}$ from penetrating the metal. In the Lorentz gauge, the electromagnetic 4-potential A^{μ} satisfies the Maxwell equation:

$$\Box A^{\nu} = j^{\nu} \tag{1.2}$$

Clearly, if j includes a screening current, such that $j = j_{sc} + j_0$, then equation 1.2
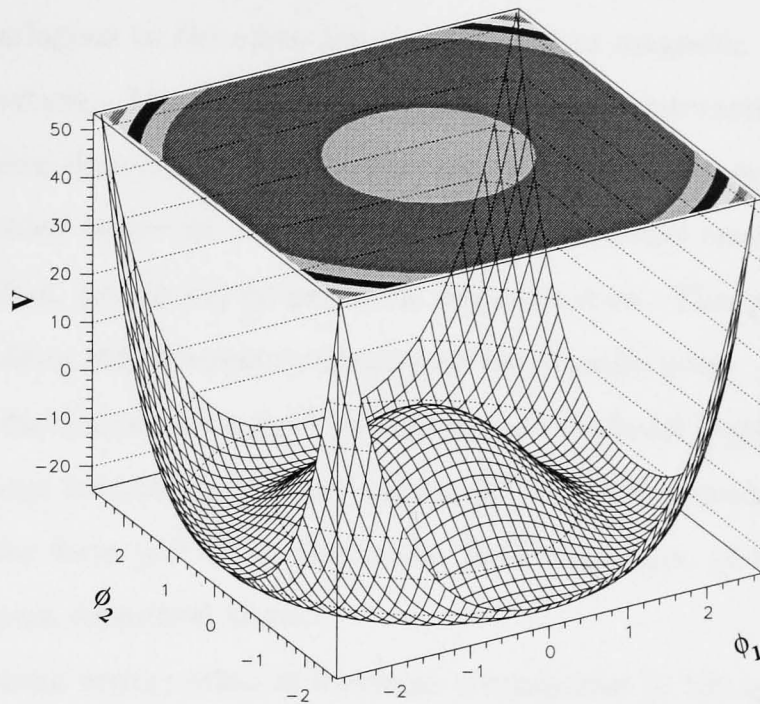
Figure 1.1: The symmetric potential V of equation 1.4 (arbitrary scale).

can be rewritten:

$$\Box A^\nu = j^\nu_{sc} + j^\nu_0$$

$$(\Box - \alpha^2)A^\nu = j^\nu_0 \tag{1.3}$$

This is just the Klein Gordon equation for a boson field of mass α. So the electric field inside a conductor acquires an effective mass, and the symmetry associated with the massless gauge field is hidden. If one lived inside a conductor it would require a leap of imagination to postulate a massless electromagnetic field, since all observable photons would be massive.

To see how this corresponds to a breaking of symmetry, consider the potential V, dependent on real fields ϕ_1 and ϕ_2:

$$V(\phi) = -\frac{1}{2}\mu^2\phi^2 + \frac{1}{4}\lambda^2\phi^4 \tag{1.4}$$

where $\phi^2 = \phi_1^2 + \phi_2^2$ and μ and λ are real. This potential is symmetric under rotations between ϕ_1 and ϕ_2, as illustrated in figure 1.1, but the ground (or minimum energy)

state lies on a circle of non-zero ϕ, radius μ/λ. The system chooses a ground state somewhere on this potential minimum and the underlying symmetry is hidden.

This is analogous to the situation encountered in magnetic materials below the Curie temperature. Magnetism arises from spin-spin interactions within a solid; the Hamiltonian describing these interactions is rotationally symmetric, but if the material is cooled below its Curie Temperature it becomes energetically favourable for spins to align, producing spontaneous magnetisation. This picks out a direction in space, breaking the inherent symmetry of the Hamiltonian.

The introduction of such a field into the Standard Model Lagrangian leads, on the demand of gauge invariance (directly via the principle of minimum substitution [5]), to terms of the form $|\phi|^2 A^\mu$ in the vector field equations, providing the required screening current described above.

The minimum energy state of a system corresponds to the quantum mechanical *vacuum*. Up to 1960, perturbations were generally taken about an *empty* vacuum, where all fields had zero expectation value. Mass generation through interaction with a non-empty vacuum was an idea first explicitly mentioned in a paper by Schwinger in 1957 [10] [1]. In 1960, Nambu [12] showed how symmetry breaking could give rise to nucleon mass, in an extension of Anderson's work on superconductors [13]. Nambu noted the appearance of massless boson states in the theory, and Goldstone showed that spontaneous symmetry breaking is always associated with the appearance of massless bosons [14]. This was inconvenient, since such states were not observed in nature, but in 1964 Higgs showed that these massless degrees of freedom can be absorbed into existing gauge boson fields, allowing them to acquire mass.

Another prediction of the Higgs mechanism was the existence of a massive scalar particle, the Higgs boson, which coupled to bosons and fermions according to their mass. This theory was developed in the context of nucleon interactions and abelian theories, but was extended to cover the non-abelian case by Kibble (1967) [15], and incorporated into Glashow's electroweak theory [16] by Weinberg (1967) [17] and Salam (1968) [18]. In 1971, 't Hooft showed that mass generation by this mechanism did indeed lead to a renormalisable theory [19] and the program was complete.

---

[1]Schwinger also questioned the view that electromagnetic gauge invariance required the photon to be massless [11]

Higgs boson mass is a free parameter in the theory, though demands of unitarity and perturbative renormalisability (discussed in § 1.5) lead to upper and lower bounds on $m_{\rm H}$.

1.4 Higgs in the neutrino channel at LEP2

1.4.1 Higgs production at LEP2

The main production mechanism for Higgs particles at LEP2 is known as *Higgsstrahlung* [20]

$$e^+e^- \xrightarrow{\;Z^*\;} HZ^0,$$

where Z^* is a virtual Z^0, here with a mass equal to the collision centre-of-mass energy ($\sqrt{s}$). The Feynman diagram for this process is shown in figure 1.2, with the on-mass-shell Z^0 decaying to neutrinos and the Higgs boson decaying to a $b\bar{b}$ pair. This is the final state investigated in this thesis.
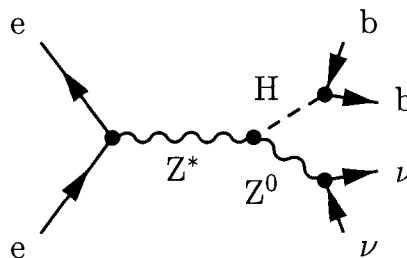
Figure 1.2: Feynman diagram for the Higgs-strahlung process

The cross-section for this process is

$$\sigma(e^+e^- \to HZ^0) = \frac{G_{\rm F}^2 m_{\rm Z}^4}{96\pi s}(v_e^2 + a_e^2)\lambda^{\frac{1}{2}}\frac{\lambda + 12m_{\rm Z}^2/s}{(1 - m_{\rm Z}^2/s)^2}, \qquad (1.5)$$

where λ is the two-body phase space coefficient [2], $G_{\rm F}$ is the Fermi constant, $m_{\rm Z}$ is the Z^0 mass, s is the square of the centre-of-mass energy and v_e and a_e are the vector and axial vector couplings of the electron and positron to the Z^*. The HZ^0 cross-section rises from threshold before falling as s^{-1}, as shown in figure 1.3. At given s, σ decreases monotonically with $m_{\rm H}$ through λ.

---

[2] $\lambda = (1 - (m_{\rm H} + m_{\rm Z})^2/s)(1 - (m_{\rm H} - m_{\rm Z})^2/s)$
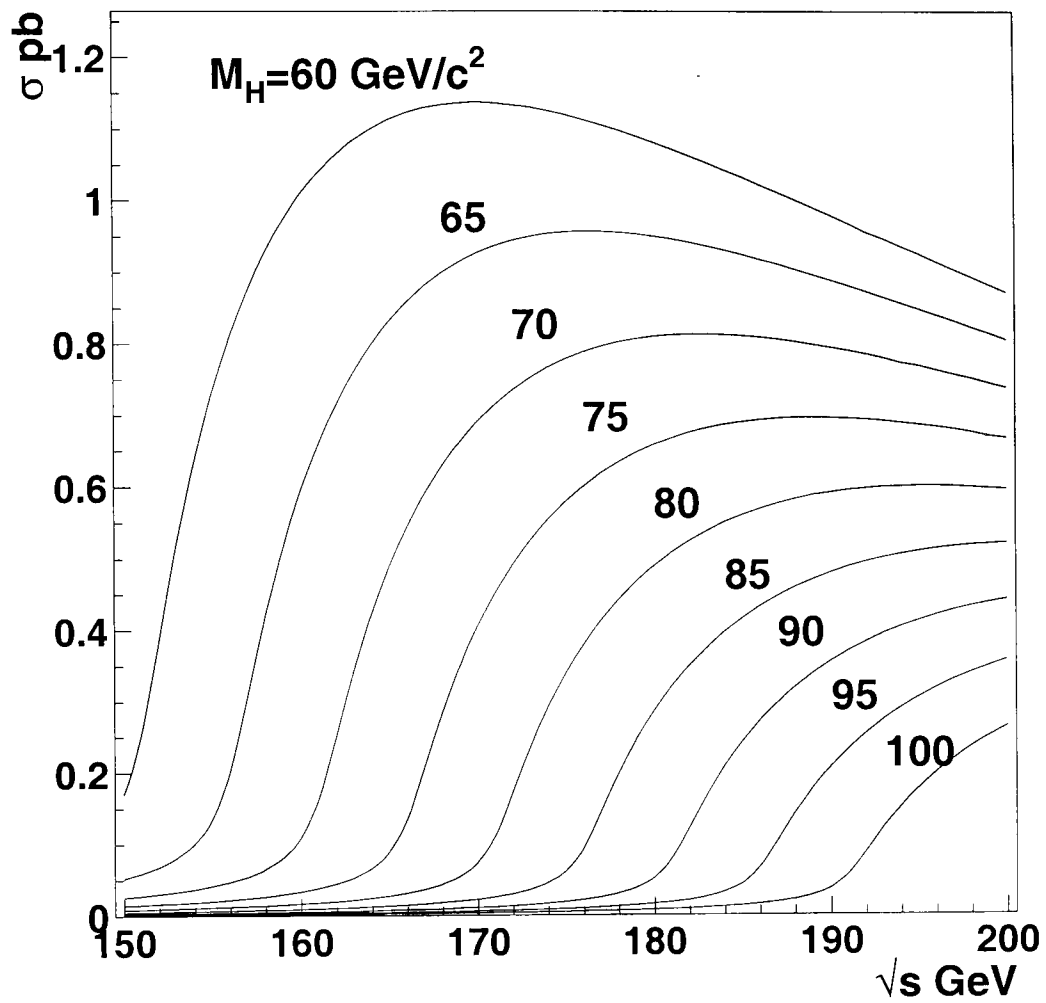
Figure 1.3: The Higgs-strahlung cross-section σ as a function of centre-of-mass energy $\sqrt{s}$ for a range of Higgs boson masses.
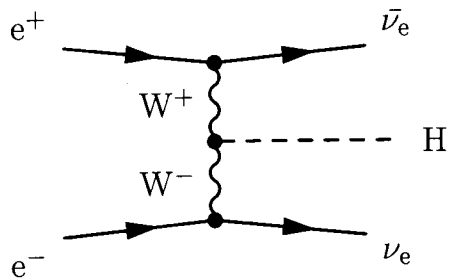
Figure 1.4: Feynman diagram for the W boson fusion processes
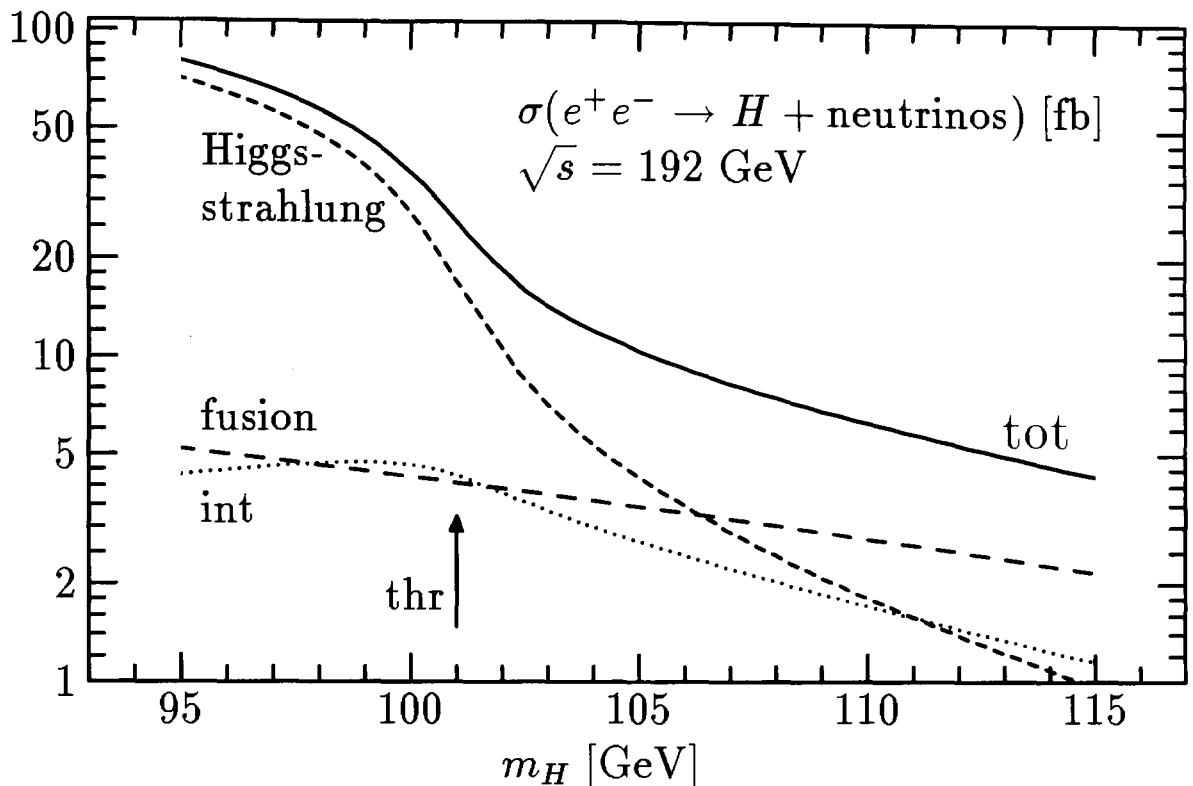
Figure 1.5: Higgs-strahlung (dashed) and WW fusion (long-dashed) processes for Higgs production in the cross-over region. The solid line shows the total cross-section for both processes including the (dotted line) interference term

The Higgs boson can also be produced via WW fusion as shown in figure 1.4. This process is suppressed by an extra power of the electroweak coupling constant and contributes little to the total Higgs cross-section at current LEP energies, as can be seen in figure 1.5. However, it does extend the reach of the Higgs search above the $m_{\mathrm{H}} = \sqrt{s} - m_z$ kinematic threshold (marked *thr* on the diagram).

1.4.2 Higgs decay modes

The branching ratios of Higgs to various final states as a function of Higgs mass are shown in figure 1.6. The Higgs couples to fermion mass, according to the formula

$$\Gamma(\mathrm{H} \to f\bar{f}) = \frac{G_{\mathrm{F}} N_{\mathrm{C}}}{4\sqrt{2}\pi} m_{\mathrm{f}}^2 (m_{\mathrm{H}}^2) m_{\mathrm{H}} \tag{1.6}$$

where G_{F} is the Fermi constant, N_{C} is the colour factor (1 for leptons; 3 for quarks) and $m_{\mathrm{f}}(m_{\mathrm{H}}^2)$ is the fermion mass at the Higgs boson energy scale. The branching ratio to tau leptons is higher than that to charm quarks because of their relative

9
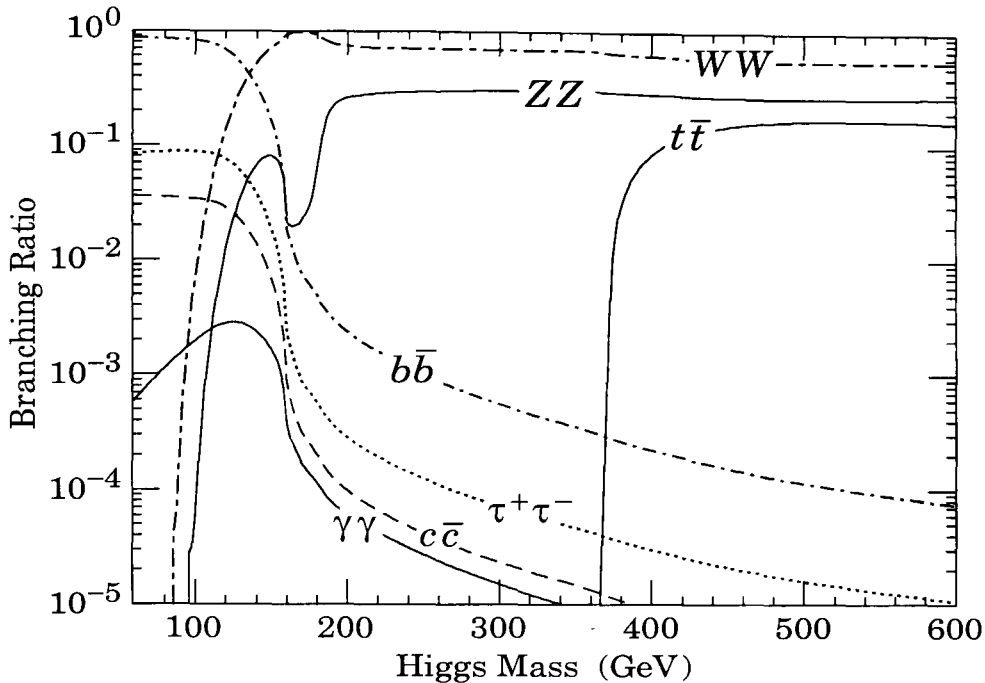
Figure 1.6: Branching ratios of the Higgs boson as a function of the Higgs mass [21].

masses (1.77 GeV versus 1.25 GeV at the Z^0 mass scale). The running of quark mass to lower values with higher mass scales accounts for the relative increase of tau production over charm.

As expected, the Higgs decays predominantly to the heaviest particles available. For the mass range accessible at LEP2 (up to ~ 110 GeV/c^2), the main decay mode is to a $b\bar{b}$ pair. Increased collision energy at future experiments such as the LHC will allow searches for higher mass Higgs, where bosonic decay modes dominate. The partial width for Higgs decay to W bosons at LEP2 energies ($m_H < 2m_W$) is given by [22]

$$\Gamma(\mathrm{H} \to \mathrm{WW}^*) = \frac{3G_{\mathrm{F}^2}m_W^4}{16\sqrt{2}\pi^3} m_H R(x) \tag{1.7}$$

where R is a steeply rising function of $x = m_W^2/m_H^2$ and W^* a virtual W, with $m_{W^*} < m_W$. This leads to a rapid increase in branching fraction to the WW* decay mode as m_H approaches the threshold for real W pair production, as shown in figure 1.6. Decays to ZZ* final states are suppressed due to the larger Z mass (phase space factors dominate over Higgs coupling).

10

1.4.3 The process $Z^0 \rightarrow \nu\bar{\nu}$

The coupling of the Z^0 to fermions can be expressed in terms of vector (v_f) and axial vector (a_f) components. To lowest order, the partial width for the decay $Z^0 \rightarrow \nu\bar{\nu}$ is given by [4]:

$$\Gamma(Z^0 \rightarrow \nu\bar{\nu}) = \frac{G_F m_Z^3}{12\pi\sqrt{2}} \qquad (1.8)$$

Multiplied by 3 for each of the 3 neutrino flavours, this corresponds to a branching fraction of 20.0%.

1.5 Current Higgs limits

1.5.1 Theoretical bounds

Upper bound

A light Higgs is very narrow, with width $\Gamma_H < 3$ MeV for $m_H < 100$ GeV/c^2 [22]. The introduction of strong vector boson couplings with increasing m_H increases the width dramatically, with Γ scaling as m_H^3 for $m_H > 2m_Z$. This leads to a Higgs self-coupling proportional to m_H^2, which eventually grow strong enough to render the theory non-renormalisable. The demand that perturbation theory remain applicable (discussed in § 1.3) places an upper bound on $m_H < 700$ GeV/c^2 [23] [3].

Lower bound

Theoretical lower bounds to m_H were first considered by Weinberg (1975) [24]. Weinberg showed that higher-order effects at low Higgs mass raise the potential minimum illustrated in figure 1.1 *above* the field-free value for an empty vacuum ($\phi = 0$), so the true ground state would no longer support the observed massive vector bosons. The limit set at $m_H > 3$ GeV/c^2 has long been overtaken by experiment, but recent lower bounds based on vacuum stability have increased this limit to $m_H > 50$ GeV/c^2 [25].

1.5.2 Experimental bounds

Since 1990, experimental bounds on m_H have been set by the combination of direct searches at the 4 LEP experiments. Results from the 1998 running of LEP at

---

[3]Reference [23] also discusses bounds and predicted Higgs mass ranges inside a number of different theoretical models.

189 GeV, where each experiment collected approximately 175 pb^{-1} of data, yield a lower mass limit of 95.2 GeV/c^2 for the Standard Model Higgs at 95% confidence level (CL) [26].

Like the top quark, the Higgs can also reveal itself at low energy through loop corrections to electroweak measurements [26]. Leading order corrections have a logarithmic dependence on Higgs mass, so the constraints are not particularly strong (relative to the mass scale accessible at LEP2). Figure 1.7 shows the result of a χ^2 fit to the combined electroweak data from LEP, SLD and other experiments (including the direct Tevatron measurement of m_{top}) as a function of Higgs mass. The solid curve is the fit result using the ZFITTER [27] Monte Carlo for Standard Model predictions. The shaded band represents uncertainty due to uncalculated higher order corrections. A 95% CL upper limit on m_H (taking errors into account) is set at 262 GeV/c^2. The vertical shaded area shows the lower limit from direct searches (not taken into account in the fit). An additional uncertainty in $\alpha(m_Z^2)$ arises from the contribution of light quarks to the photon vacuum polarisation ($\Delta\alpha_{had}^{(5)}(m_Z^2)$). The dashed curve represents the result obtained using a new evaluation of $\Delta\alpha_{had}^{(5)}$ [28].
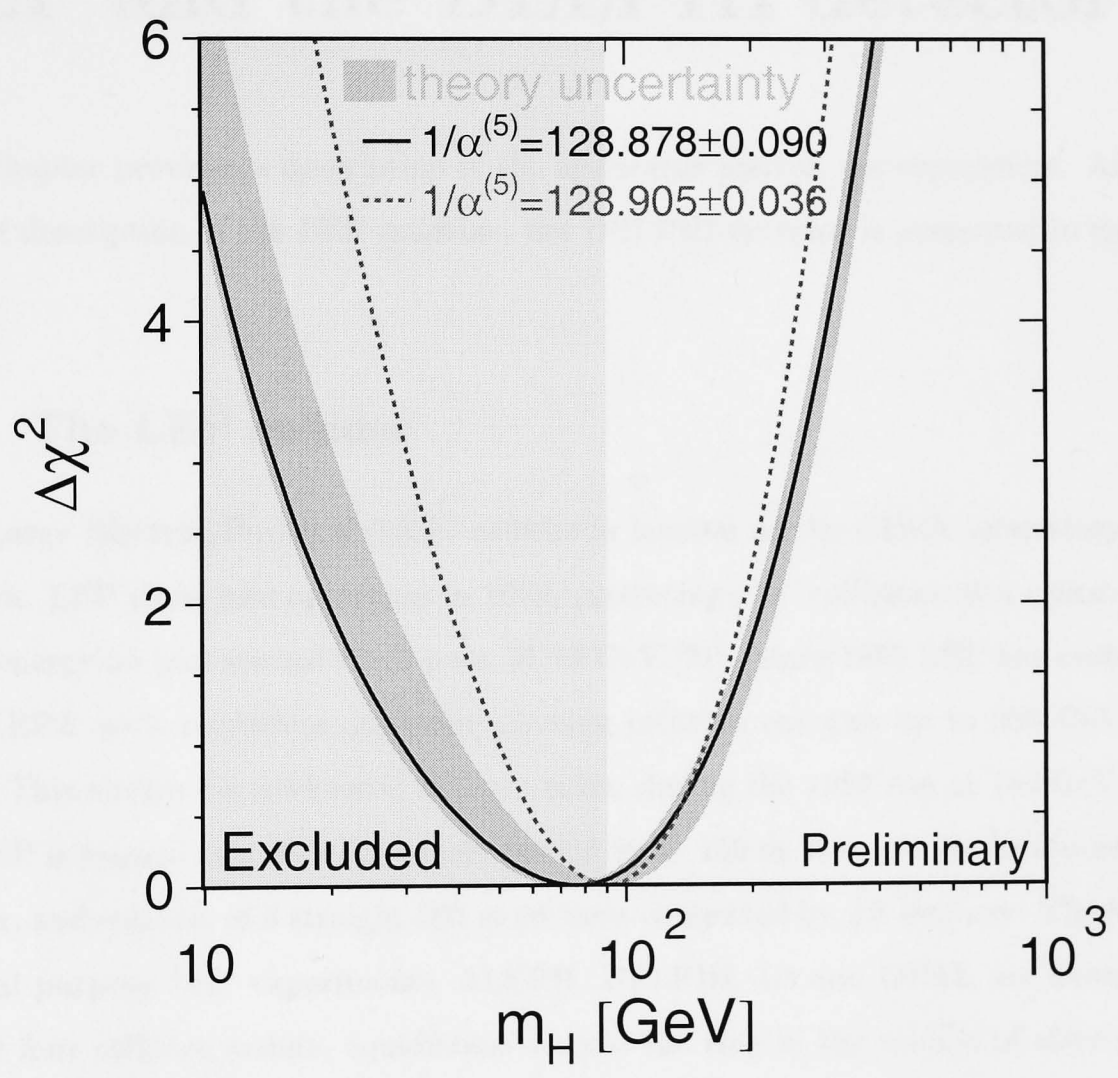
Figure 1.7: m_H dependence of $\Delta\chi^2 \equiv \chi^2 - \chi^2_{min}$ resulting from a global fit to experimental data (up to August 1998). The band represents an estimate of the theoretical error due to missing higher order corrections. The vertical band shows the 95% CL exclusion limit on m_H from direct searches.

Chapter 2

LEP and the DELPHI detector

This chapter provides a description of the apparatus used in the experiment. After a brief description of the LEP machine, the DELPHI detector is presented in more detail.

2.1 The LEP collider

The Large Electron-Positron (LEP) collider is located at the CERN laboratory in Geneva. LEP came into operation in 1989, producing e^+e^- collisions at a centre-of-mass energy on and around the Z-pole, 91.19 GeV [21]. Since 1995 LEP has evolved into LEP2, with successive upgrades allowing collision energies up to 200 GeV in 1999. This analysis is performed on data taken during the 1997 run at 183 GeV.

LEP is housed in a 26.7 km tunnel buried 50 to 150 m beneath the franco-swiss border, and consists of 8 straight 500 m sections connected by 2.8 km arcs. The four general purpose LEP experiments, ALEPH, DELPHI, L3 and OPAL are situated at the four collision points, equidistant around the ring in the middle of alternate straight sections.

In order to accelerate the electrons and positrons most efficiently to the required energy, they are produced, stored and accelerated in stages through CERN's existing network of injectors, accelerators and rings, as illustrated in figure 2.1. Electrons are produced through thermionic emission and accelerated to 200 MeV in the LEP Injector Linac (LIL). Some electrons are steered into a tungsten target, from which positrons produced via Bremsstrahlung and pair creation are separated using a magnetic field. The positrons and remaining primary electrons are accelerated to 600 MeV before injection into the Electron-Positron Accumulator (EPA).
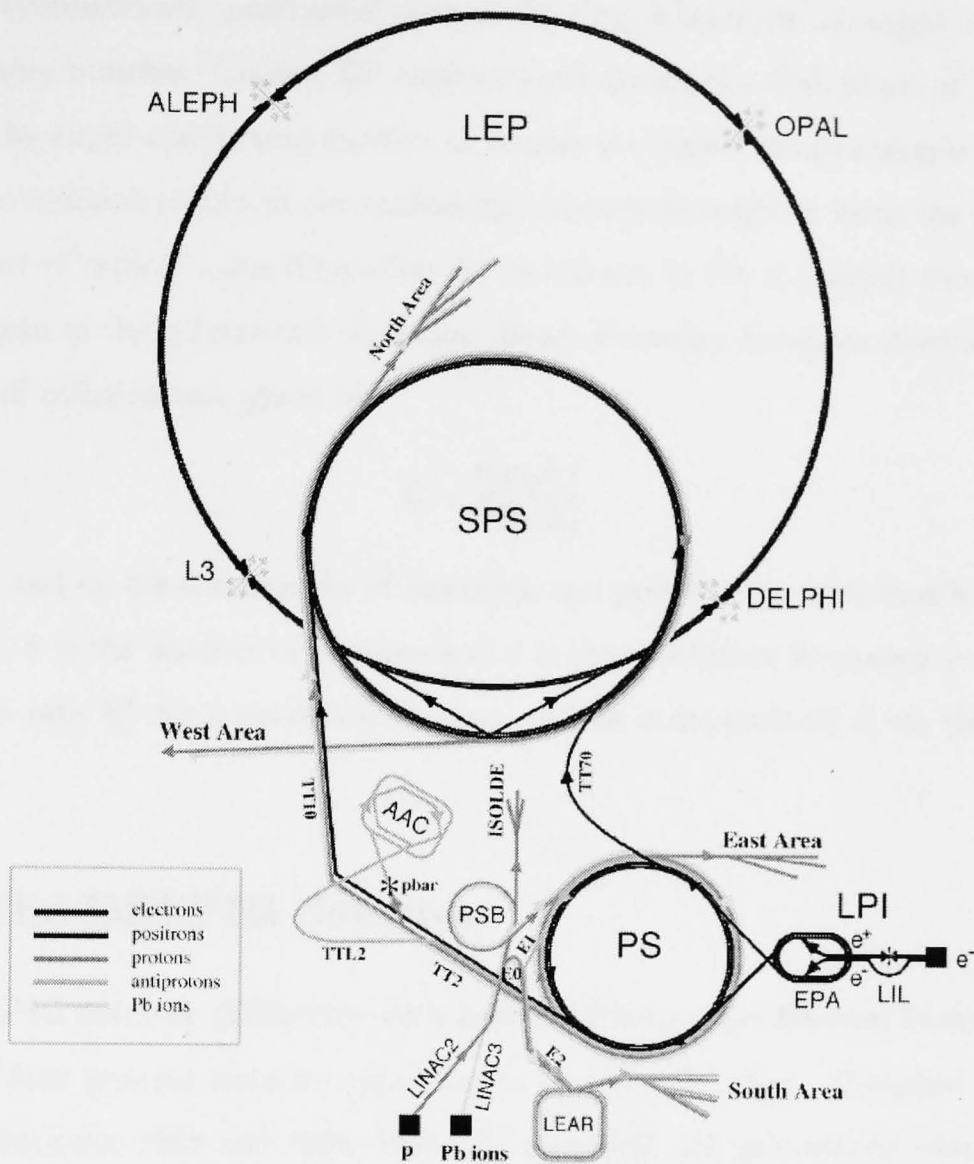
Figure 2.1: The network of injectors, accelerators, storage rings and colliders at CERN. Positron and electron paths are shown in black, protons, antiprotons and lead ions in grey.

After several LIL cycles, electrons and positrons stored in the EPA are accelerated through the PS (to 3.5 GeV) and SPS (to 22 GeV) until final injection into LEP[1]. Beam pipes are maintained under high vacuum to minimise collisions between the beam and gas molecules.

The electrons and positrons are guided around the curved sections by bending dipole magnets. Consequent synchrotron radiation losses necessitate constant re-acceleration of the particles in Radio-Frequency (RF) systems in the linear sections. Phase focusing of the RF system concentrates the particles into bunches; usually 4

[1]Electrons could not be accelerated from rest in LEP; power supplies do not yet exist that could provide stable power to solenoids over such a large dynamic range

bunches symmetrically positioned around the ring, sometimes arranged in "trains" of 2 or more bunches. Copper RF cavities used during the first phase of LEP were replaced by super-conducting cavities to enable the higher beam energies at LEP2.

At the collision points, superconducting quadrupole magnets focus the beam into a *beamspot* of typical r.m.s dimension $\Delta_x \simeq 100\ \mu$m in the x (radial) direction and $\Delta_y \simeq 10\ \mu$m in the y (vertical) direction. Beam focussing increases *luminosity*, $\mathcal{L}$; a measure of collision rate given by

$$\mathcal{L} = \frac{n_e n_p k f}{\pi \Delta_x \Delta_y} \tag{2.1}$$

where n_e and n_p are the number of electrons and positrons in each bunch ($\sim 4.10^{11}$ particles), k is the number of bunches and f is the revolution frequency (~ 11 kHz). The event rate $\frac{dN}{dt}$ for a process with cross-section σ depends on $\mathcal{L}$ via the relation $\frac{dN}{dt} = \sigma \mathcal{L}$.

2.2   The DELPHI detector

The DELPHI detector (**DE**tector with **L**epton, **P**hoton and **H**adron **I**dentification) is one of four general purpose experiments on the LEP ring. Designed and constructed between 1982 and 1989, DELPHI provides high granularity over much of the 4π solid angle, with an emphasis on particle identification, three-dimensional spatial information and precise vertex reconstruction. The detector consists of 19 sub-detectors and a superconducting solenoid surrounding the central tracking region. *Tracking detectors* make precise measurements of spatial position for charged tracks, whilst *calorimeters* are used to measure neutral and charged particle energy.

Inside the 1.2 Tesla solenoidal field, charged particles follow a helical path with axis parallel to the beampipe. The radius of curvature R depends on track charge q and transverse momentum p_t according to the formula:

$$R = \frac{p_t}{qB} \tag{2.2}$$

This reduces to $R \simeq 2.8 p_t$ metres for a track of 1 unit charge with momentum measured in GeV/c. Since curvature depends on p_t, momentum measurements are more accurate for tracks travelling transverse to the beam and the bulk of the tracking is concentrated in this region.

16

Figure 2.2 shows a section of the central or *barrel* region of DELPHI as well as one of DELPHI's two end-caps covering the *forward* region.

Forward Chamber A
Forward RICH
Forward Chamber B
Forward EM Calorimeter
Forward Hadron Calorimeter
Forward Hodoscope
Forward Muon Chambers
Surround Muon Chambers

Barrel Muon Chambers
Barrel Hadron Calorimeter
Scintillators
Superconducting Coil
High Density Projection Chamber
Outer Detector
Barrel RICH
Small Angle Tile Calorimeter
Quadrupole
Very Small Angle Tagger
Beam Pipe
Vertex Detector
Inner Detector
Time Projection Chamber

DELPHI

Figure 2.2: The DELPHI detector

The DELPHI detector has been described in detail elsewhere [29–31]. This section will briefly describe the detector components of relevance to a Higgs search in the H$\nu\bar{\nu}$ channel, following an introduction to the DELPHI coordinate system.

The DELPHI coordinate system

The standard DELPHI reference frame uses a horizontal x axis pointing towards the LEP centre, a vertical y axis and horizontal z aligned with the beam in the direction of electron travel. ϕ is the azimuthal angle in the xy plane and θ the polar angle with respect to the z axis. In cylindrical coordinates, radius r is measured perpendicular to the beam; the xy projection is also referred to as the $r\phi$ plane.

2.2.1 Tracking detectors

In the barrel region of DELPHI, charged particle trajectories are reconstructed from space-points provided by four tracking devices. These are the Microvertex Detector (VD), Inner Detector (ID), Time Projection Chamber (TPC) and Outer Detector

17

(OD). Tracking in the forward region consists of Forward Chambers A and B (FCA and FCB), with the Very Forward Tracker (VFT), installed in 1996. High resolution detectors are placed close to the beamspot to allow accurate reconstruction of primary and secondary vertices.

The Microvertex Detector

The upgraded DELPHI VD [32–34] consists of three layers of silicon microstrip detectors, 48 cm in length, at radii of 63, 90 and 109 mm. The detector measures both $r\phi$ and z coordinates. The VFT forms a crown of pixel and ministrip detectors capping both ends of the VD, and allows polar angle tracking coverage down to 11°.

With precision of 7.6 μm per layer in $r\phi$ and up to 9 μm in z, the VD can reconstruct secondary vertices from the decay of short-lived particles. This is important in the search for H→ b$\bar{\text{b}}$ decays, which produce B mesons with a mean decay length of ∼ 2.5 mm. Figure 2.3 shows a clear secondary vertex reconstructed using the VD.
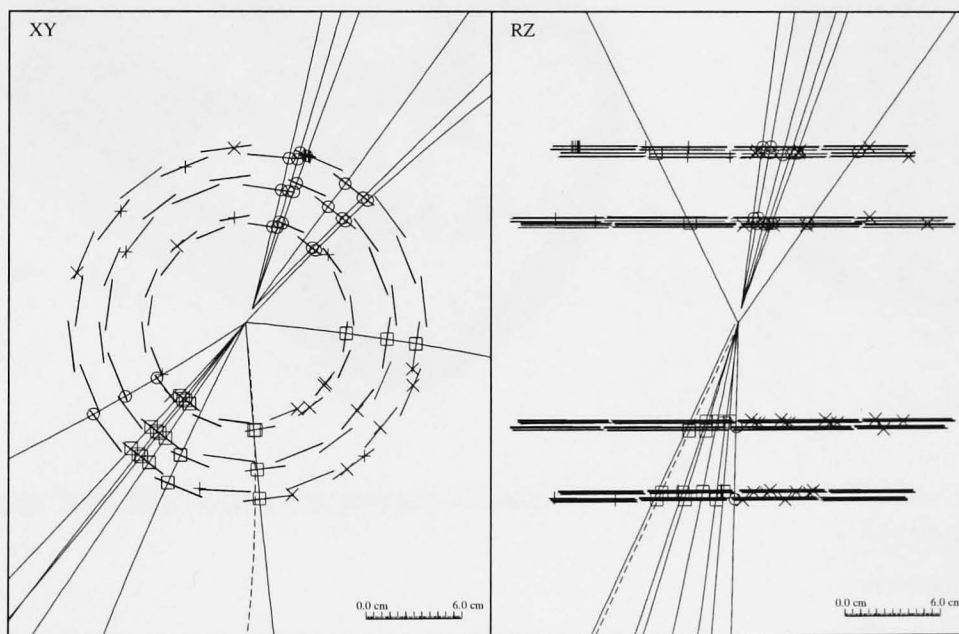
Figure 2.3: The xy and rz projection of a hadronic Z^0 decay observed in the DELPHI microvertex detector.

The Inner Detector

The ID comprises a jet chamber and a straw detector, situated in the region 11.8 < r < 28 cm, and covering polar angles of 15–165°. The jet chamber is a drift chamber divided into 24 azimuthal sectors, each with 24 drift wires strung parallel to

the beampipe and staggered in r. These give a track radial coordinate, with ϕ reconstructed from electron drift-time in the CO_2-isobutane gas mixture, and 40 μm single wire resolution in $r\phi$.

The Straw tubes consist of 5 cylindrical layers of streamer tubes surrounding the outside of the jet chamber. These give further $r\phi$ and z information, but are mostly used for triggering due to their fast ($< 3\ \mu$s) read-out time.

The Time Projection Chamber

Lying outside the ID, the TPC is the main tracking device in DELPHI. It is 2.6 m long, with an active volume between 29 and 122 cm in radius.
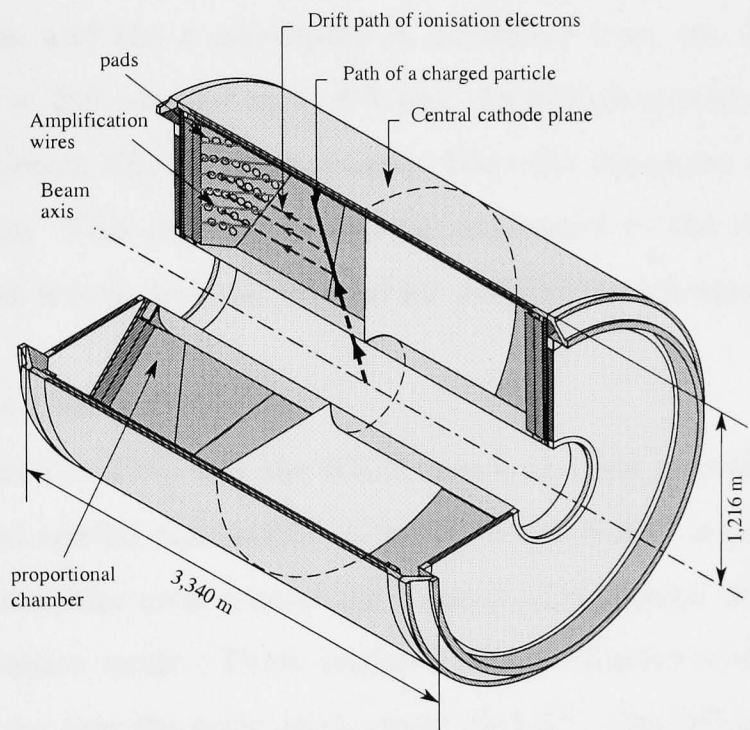
Figure 2.4: The Time Projection Chamber
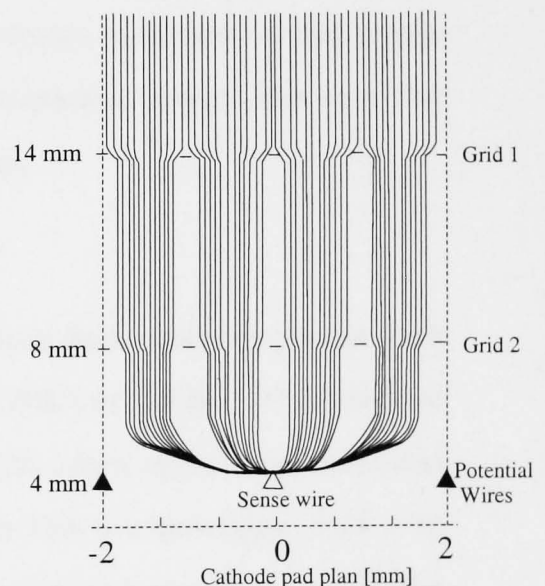
Figure 2.5: Wire geometry and field lines at the end-plates of the TPC.

The detector is divided into 6 azimuthal sectors, with a transverse cathode plane bisecting the centre as shown in figure 2.4. Charged tracks ionise an Argon-Methane gas mixture and the freed electrons (about 70 per cm) drift under a 187 Vcm^{-1} electric field to readout planes in the end plates. Here they are detected by 192 anode wires and 16 segmented concentric cathode pads. Due to the high magnetic field, electrons do not drift directly to the anode but spiral around field lines; an effect that rather conveniently limits transverse diffusion. The drift velocity is almost uniform

at 65 μm s^{-1}, but is constantly monitored using lasers. These produce ionisation clouds at known coordinates from which drift velocity can be calibrated.

The cathode end plate is shielded by a 3 layer grid of wires, as illustrated in figure 2.5. The outer layer contains wires with a small alternating ± 30 V potential. This acts as a gate to slow moving ions produced at the end plate, preventing their accumulation distorting the drift field. The middle layer is a cathode grid, limiting the electric field in the proportional chamber below. This consists of the closer layer of 192 sense wires at 1430 V separated by shield wires. Electrons avalanche at the anode, inducing a signal on the cathode pads below.

The r and ϕ positions of each point are obtained from the cathode pad information and the z coordinate is calculated from the drift time, with resolutions of $\sigma_{r\phi} = 250$ μm and $\sigma_z = 880$ μm. As well as spatial information it is also possible to obtain dE/dx measurements from the deposited charge collected on the anode wires. This quantity is directly associated to the ionization energy loss over the track length and can be used for particle identification.

The Outer Detector

After the TPC and the RICH comes the OD, providing final tracking points with good spatial resolution. Situated between 197 and 208 cm radius, it consists of 24 modules each containing 5 layers of staggered drift tubes operating in limited streamer mode. These measure $r\phi$ coordinates with 110 μm precision, and z to ± 4 cm over the polar angle range 43–137°. The OD improves momentum resolution by a factor of 4 for tracks over 30 GeV, and also provides trigger information through fast read out.

The Forward Chambers

The Forward Chambers A (FCA) and B (FCB) each consist of three modules with respectively 2 and 4 staggered planes of drift tubes operating in limited streamer mode. Together, they provide tracking between 11° and 36°. The precisions on track elements obtained are $\sigma_x, \sigma_y = 250$ μm, $\sigma_\theta = 8.5$ mrad and $\sigma_\phi = 24$ mrad for the FCA and $\sigma_x, \sigma_y = 150$ μm, $\sigma_\theta = 3.5$ mrad and $\sigma_\phi = 4/\sin\theta$ mrad for the FCB.

Table 2.1 summarises the specifications and performance of the DELPHI tracking detectors.

Detector	Position		Acceptance $\theta(°)$	Max. no. of points along track	Resolution per point (mm)
	r (cm)	$|z|$ (cm)			
VD	6.3/9.0/10.9	≤ 24	≥ 21	3 in $r\phi$	0.008 in $r\phi$
				2 in z	0.010 in z
ID jet	12–23	≤ 62	≥ 15	24	0.085 in $r\phi$
TPC	35–111	≤ 134	≥ 20	16 in $r\phi,z$	0.25 in $r\phi$
				192 in $r\phi$	0.9 in z
OD	197–206	≤ 232	≥ 42	5 in $r\phi$	0.11 in $r\phi$
				3 in z	35 in z
FCA	30–103	155–165	11–32	6	0.25
FCB	53–195	267–283	11–53	12	0.15

Table 2.1: Summary of the DELPHI tracking detectors.

2.2.2 Calorimetry

Tracking detectors aim to measure particle positions without appreciably altering their path. Calorimeters are used to measure particle energies by stopping them through multiple interactions with dense matter.

Electromagnetic calorimeters measure electron and photon energies. They provide a dense medium for interaction via Bremsstrahlung and pair production and measure the properties of the resultant showers of secondary electrons and photons.

Hadronic calorimeters exploit the nuclear interactions of hadrons to measure their energy, with energetic hadrons producing hadronic showers.

Electromagnetic calorimeters partially stop hadrons but totally stop electrons and photons, and so are placed inside hadronic calorimeters in the detector.

The High-Density Projection Chamber

The HPC consists of 144 modules, with 24 segments in ϕ and 6 along z. It is 508 cm long and has an inner radius of 208 cm and outer radius of 260 cm covering the angular region 41.5° to 138.5°. Each module is filled with 41 layers of lead separated by gas gaps (80–20% Argon–Methane). An electromagnetic particle showers in the

21

lead and ionizes the gas. The charge drifts to one end of the box, where it is collected by a proportional chamber with pad readout (like in the TPC). The shower arrival position gives $r\phi$ information and the drift time gives z. The resolutions for 45 GeV electrons in θ and ϕ are $\sigma_\theta = 0.6$ mrad and $\sigma_\phi = 3.1$ mrad, the two-shower separation is $2°$ and the error on the energy measurement is $\sigma_E/E = 0.043 \oplus 0.32/\sqrt{E}$ [31].

The Forward Electromagnetic Calorimeter

The FEMC is a lead glass calorimeter situated in each end-cap, beyond the FCB. Each consists of 4532 Čerenkov lead-glass blocks, and cover polar angles from $8°$ to $35°$ from the beam pipe. Čerenkov radiation emitted by electrons in the glass is collected by vacuum phototriodes at the end of each block. Energetic photons are detected via conversion to electron-positron pairs.

Photons over 2 GeV are reconstructed with an (x,y) precision of $\simeq (5,5)$ mm [31]. The energy resolution is $\sigma_E/E = 0.03 \oplus 0.12/\sqrt{E} \oplus 0.11/E$ [31].

The Small Angle Tile Calorimeter

The STIC is a sampling lead-scintillator calorimeter covering the angular region between 1.7 and $11°$ in θ, hence overlapping with the FEMC. Two silicon planes at the front of the detector can be used as an electron veto. The STIC provides a luminosity measurement, using the Bhabha scattering process $e^+e^- \longrightarrow e^+e^-$ at low angles, but can also be used to tag high energy, low angle electrons and photons.

The Hadron Calorimeter

The HAC is a sampling gas detector covering the whole region for which tracking information exists; from 11–$169°$. Situated in the return yoke of the DELPHI magnet, the HAC is made up of two end-cap units and a barrel section. Over 19000 streamer tubes are placed in 2 cm gaps between the 5 cm thick iron plates of the return yoke. Operating on a similar principal to the HPC, hadronic showers initiated in the lead are sampled by the streamer tubes to produce an energy measurement with precision $\sigma_E/E = 0.21 \oplus 1.12/\sqrt{E}$ [31].

The specifications and resolutions of the DELPHI calorimeters are summarized in table 2.2[2].

---

[2]Depth refers to radiation length X_0: the mean distance over which a high energy electron loses

Detector	Position		Acceptance $\theta(^\circ)$	Depth	Shower resolution (σ_{E}/E) (%)
	r (cm)	$|z|$ (cm)			
HPC	208–260	≤ 254	≥ 43	$18X_0$	$4.3 \oplus 32/\sqrt{E}$
FEMC	46–240	284–340	10–36.5	$20X_0$	$3.0 \oplus 12/\sqrt{E} \oplus 11/E$
HAC	65–479	< 489	≥ 10	6λ	$21 \oplus 112/\sqrt{E}$
STIC	6.4–41	218–249	1.7–10.6	$27X_0$	$1.5 \oplus 13.5/\sqrt{E}$

Table 2.2: Specifications and performances of the DELPHI calorimeters

2.2.3 Other detectors

The hermeticity taggers

As well as gaps between HPC modules, DELPHI electromagnetic calorimetry design led to cracks between the forward and barrel regions and also at 90°, thus making it difficult to record all the energy of an event. To overcome this, taggers are placed in the gaps between the barrel and end-cap regions at 40°, to veto events with otherwise undetected photons. Similar scintillators are placed in the ϕ gaps between HPC modules, and in the 7.5 cm hole at 90° which accommodates a stiffening ring for the cryostat.

The muon chambers

Penetrating muons are identified using the barrel (**MUB**), forward (**MUF**) and surround (**SMC**) muon chambers situated on the outside of DELPHI, with one further layer inside the iron of the HAC. The detectors are composed of several planes of proportional wire drift chambers, and together they cover the region 20–160° in θ. Tracks are extrapolated to hits in the muon detectors using a map of the field within the solenoid return yoke and allowing for multiple scattering in the HAC.

The RICH detectors

Unique amongst LEP experiments, DELPHI includes **Ring Imaging Čerenkov**

---

all but a factor $1/e$ of its energy. λ is defined similarly for hadrons

detectors in the forward and barrel regions. These use the detection of Čerenkov light to measure particle velocities, which can combine with a momentum measurement to provide particle identification. The FRICH sits between forward chambers A and B, and the barrel RICH fits snugly between the TPC and the OD.

2.3 The DELPHI Online System

The DELPHI online system has to manage several functions during running: analyse events on an elementary level and supply a fast trigger decision; read out all the detector components and write the data to storage media; run the power supplies, gas and cooling systems of the detector and control and log all the slowly varying detector parameters. The set-up of these systems is described in detail elsewhere [35–37] and will not be discussed further here.

2.4 The DELPHI offline analysis chain

Raw data from the detector is processed offline to reconstruct events into a form useful for physics analysis. This procedure is summarized by the flow diagram in figure 2.6, with the main stages described briefly below.

2.4.1 The DELPHI SIMulation program DELSIM

DELSIM produces samples of simulated events to be compared with real events from the experiment. Monte Carlo event generators such as PYTHIA [38] are used to generate physics events at the parton level, with quarks fed through fragmentation programs like JETSET [39] or HERWIG [40] to produce 'final state particles' stable enough to reach the detector. These particles are then propagated through DELSIM [41]: a simulated model of the DELPHI detector. This involves tracing each particle through small steps in time, allowing for the possibility of secondary interactions with detector material and the decay of short-lived particles, such as the τ. A full description of the detector geometry and material characteristics is maintained by the CARGO database. This is updated online by each subdetector to register changes in position, drift velocity, temperature, pressure etc.
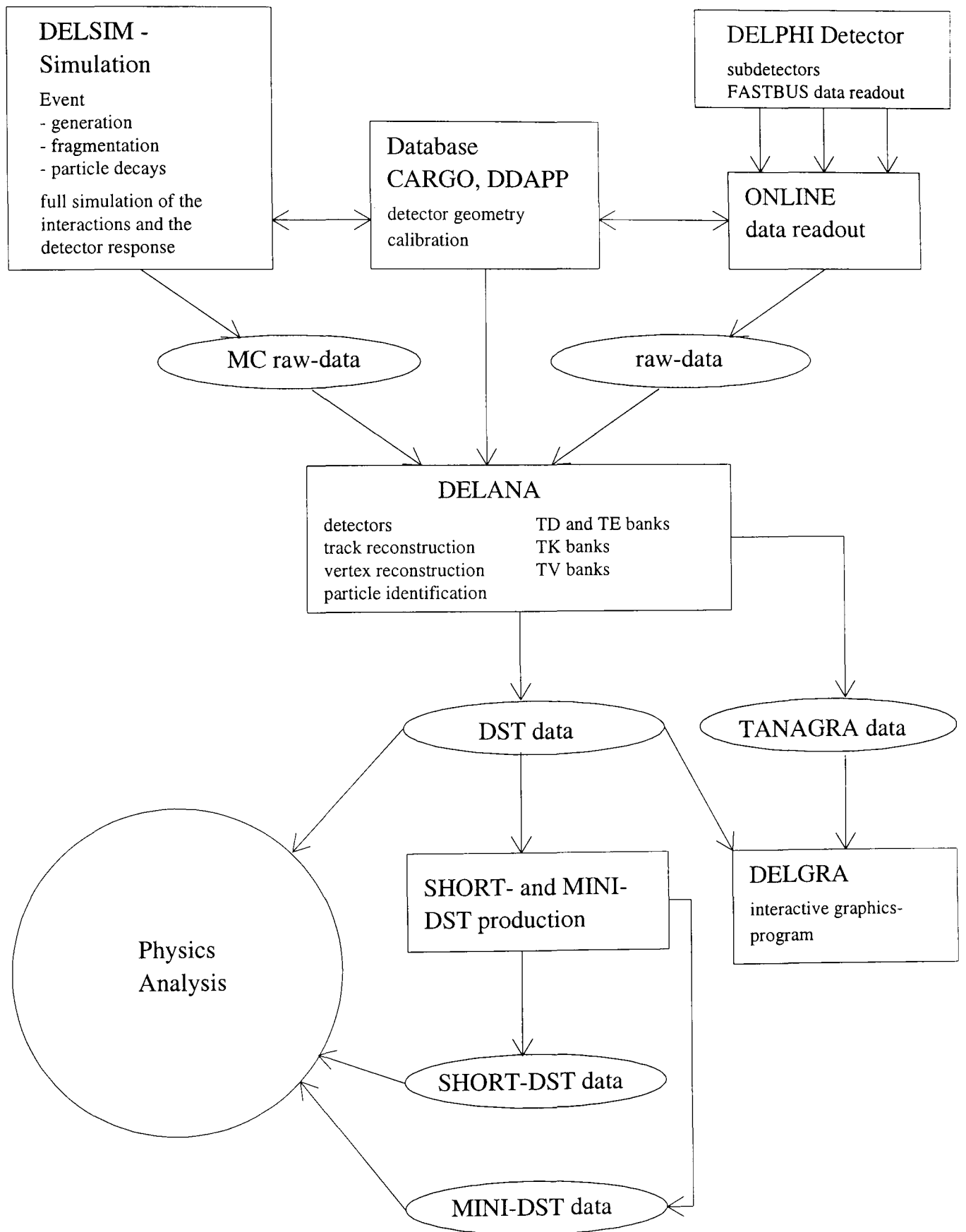
Figure 2.6: The DELPHI offline analysis chain.

2.4.2   The DELPHI ANAlysis package DELANA

DELANA [42] is the main reconstruction program, converting raw data in the form of tracking hits and calorimeter deposits into charged tracks and neutral clusters. Taking data from the detector and DELSIM alike along with up-to-date information from the CARGO database, DELANA reconstructs events in the following stages:

TD   Track Data objects, such as the space points of individual hit wires, are constructed separately inside each subdetector.

TE   TDs inside a subdetector are linked by pattern recognition programs into short strings, or Track Elements (TEs). These are stored as either the parameters of fitted track fragments from the tracking detectors, or a grouped cluster of hits in the calorimeters.

TK   TEs in the various subdetectors are extrapolated to produce fitted tracks, or TKs. This is a two-pass process, with extrapolated information from TKs produced during the first pass being used in each subdetector to resolve ambiguities and perhaps locate new TEs, which are then used in the second stage track fit.

TV   Track Vertices are found by extrapolating the fitted TKs. A TV consists of the coordinates and errors of the fitted vertex and the list of TKs pointing to it.

DELANA   produces Data Summary Tapes (DSTs), which contain all the information required for physics analysis. The DST ANAlysis program DSTANA is then run on the DST, providing some TE corrections not implemented at the DELANA level and refitting TKs and TVs accordingly. SHORT- and MINI-DST are also produced at this stage, providing efficient summaries of event information. The Track ANAlysis and GRAphics package TANAGRA provides information for event viewing in DELGRA the DELPHI GRAphics program. This is a utility for visually examining events, and is a useful tool; both for checking detector performance and providing a concise summary of an individual event.

Figure 2.7 shows a simulated $H\nu\bar{\nu}$ event for an 85 GeV/c^2 Higgs at $\sqrt{(s)} = $ 183 GeV, displayed using DELGRA. The HPC and FEMC subdetectors are also shown, along with two jets from the Higgs decay.
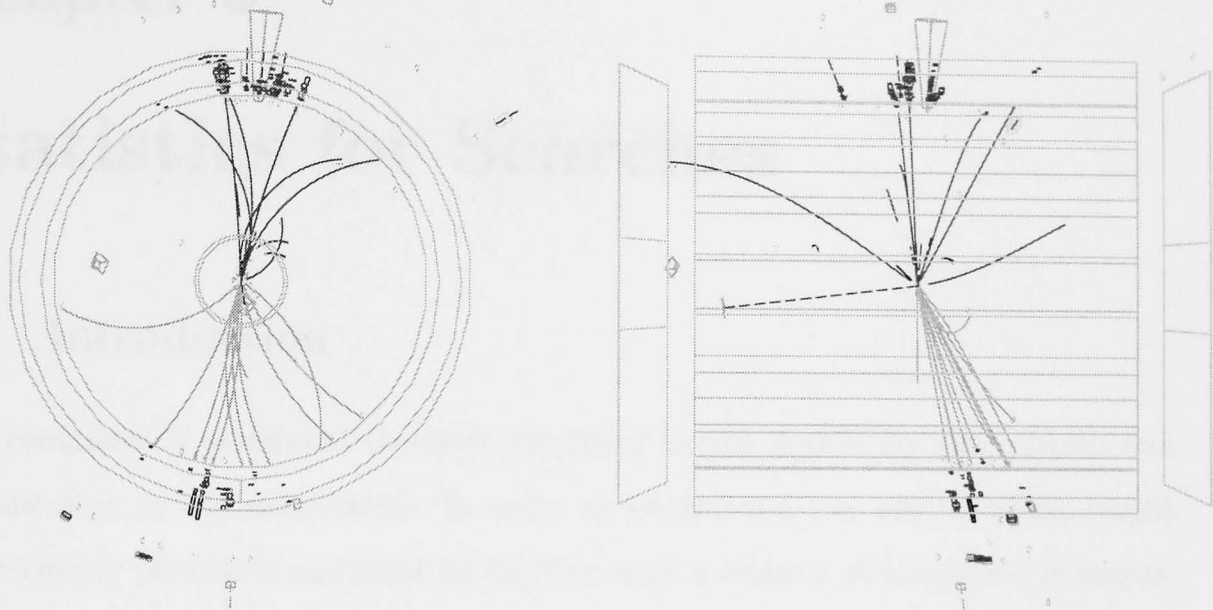
(a) xy projection   (b) yz projection

Figure 2.7: A simulated $H\nu\bar{\nu}$ event in the DELPHI detector, displayed by DELGRA. The HPC and FEMC subdetectors are shown along with two acollinear jets from the Higgs decay.

Chapter 3

Statistics for Searches

3.1 Introduction

The profusion of statistical methods employed in the search for new physics can be confusing to the uninitiated. In order to understand the way in which results are currently presented one must be familiar with a number of terms and concepts, mostly derived from the statistical field of *hypothesis testing*. This chapter provides a brief introduction to hypothesis testing, a general overview of its application to the LEP Higgs search, and a description of the particular techniques employed in this analysis.

3.2 Hypothesis Testing

This section follows the approaches described in [43–45], and begins with a simple example.

A new particle will usually manifest itself as an excess of events in a particular region of phase-space. After cuts, the expected number of background events in this region is b, with an extra s expected if the signal is present. The number of events n observed will be Poisson distributed, with probability $P(n|b) = e^{-b}b^n/n!$ for background alone, and $P(n|s+b) = e^{-(s+b)}(s+b)^n/n!$ in the presence of signal. The distributions of n for $b = 4.2$ and $s = 3.6$ are shown in figure 3.1.

The choice is between two hypotheses: background plus signal (abbreviated to "signal"), or background alone. One has to decide which to accept on the basis of an observation of n. Clearly, low values of n do not support the signal hypothesis. A *critical value* n_c can be chosen, such that $P(n \leq n_c|s+b) = CL_{s+b}$; i.e. one
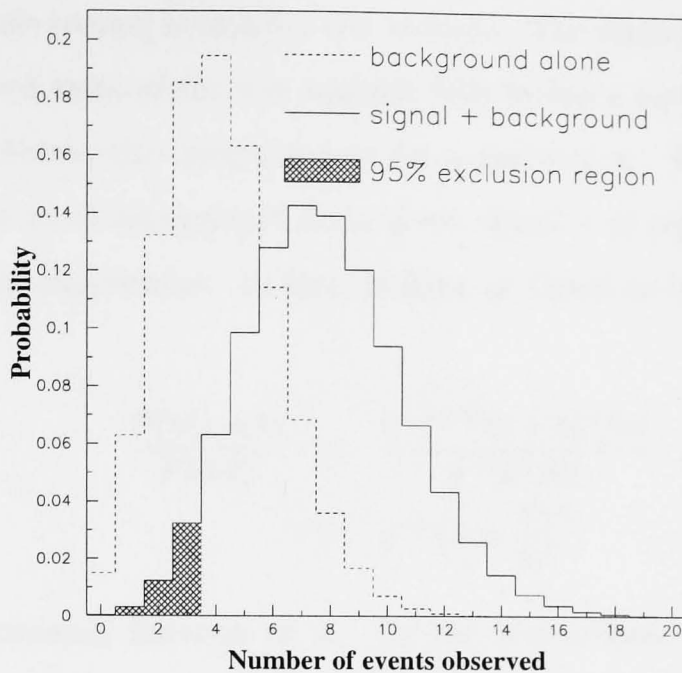
Figure 3.1: Poisson distributions for 4.2 background events (dashed) and with an extra 3.6 signal events (solid). The shaded area represents the 95% signal exclusion region; a measurement of $n \leq 3$ would allow us to exclude the signal hypothesis to the 95% confidence level.

would only expect to measure $n \leq n_c$ in a fraction CL_{s+b} of cases if the signal were present. If the observed value of n falls in this range, then the signal is rejected to the $(1 - CL_{s+b})$ confidence level (abbreviated CL). In the above example, for $n_c = 3$, $CL_{s+b} = P(n \leq 3|7.8) = 0.05$, so if 3 events or less are observed, the signal hypothesis can be rejected to the 95% CL.

In this simple example, an observation of $n > n_c$ leads to the rejection of background in favour of the signal. Given that only one of the possibilities correctly describes the data, there are two possible errors:

1. Rejecting the signal when it is present. This occurs with probability CL_{s+b}, often called the *significance* of the test, or the probability of *false exclusion*.

2. Rejecting the background when no signal is present. This would happen in a fraction $(1 - CL_b)$ of cases, where CL_b is the *power* of the test.

Clearly the aim is to make both CL_{s+b} and $(1 - CL_b)$ as small as possible [1].

---

[1] There is no universal common definition for these terms; the terminology adopted here is that used by the LEP Higgs Working Group. CL_{s+b} and CL_b above are often called α and $(1 - \beta)$, but

The variable n is a function of observed quantities, or a *statistic*. A statistic used in hypothesis testing is called a *test statistic*. The signal hypothesis is rejected when the observed value of the test statistic falls within a certain range, termed the *critical region*. Above, the critical region for n was $n \leq n_c$. This region was chosen as that with the most background for a given signal – or equivalently the highest power for a given significance. In fact, looking at signal to background ratio (s/b) in a bin of n:

$$\frac{P(n|s+b)}{P(n|b)} = \frac{e^{-(s+b)}(s+b)^n/n!}{e^{-b}b^n/n!} \tag{3.1}$$

$$= e^{-s}\left(1+\frac{s}{b}\right)^n \tag{3.2}$$

which is an increasing function of n. So the *best critical region* (BCR) is that with lowest s/b. This is a particular case of a general lemma due to Neyman and Pearson [45]. In general a value of CL_{s+b} (or test significance) is chosen, and the BCR is the region with lowest s/b covering a fraction CL_{s+b} of the signal. This region is "best" because it maximizes the test power CL_b for a given significance.

Since the statistic n is discrete, the values of CL_{s+b} are also discrete . For example, the critical region $n \leq 3$ above corresponds to $CL_{s+b} = 4.8\%$, while $n \leq 4$ gives $CL_{s+b} = 11.2\%$, so there is no BCR corresponding precisely to 5% significance. This can be accommodated by a modification of the definition of significance, such that the probability of false exclusion is **at most** CL_{s+b}. Thus the critical region $n \leq 3$ is chosen above. This and other complications are associated in particular with discrete statistics like n (in fact, the Neyman Pearson lemma holds exactly only for continuous statistics). We shall move swiftly on to continuous statistics, but the modified definition of significance given above will still prove useful.

3.2.1 Optimal Test Statistic

In the preceding example the test statistic was just n, the number of events found in a particular region of phase-space. Clearly this is not optimal; all information as to where the events lie inside and outside the cuts is lost. An event in a region of high s/b should constitute greater evidence for signal than one of low s/b. An ideal statistic would take into account s/b for **each** event – perhaps in a weighted sum.

can also be defined as $(1 - \alpha)$ or β, depending on the text.

30

The "cut and count" procedure described in the previous section can be seen as a weighted sum, with events passing the cuts awarded weight one and those failing given weight zero. The above analysis suggests using a new weight function $W(\mathbf{x})$, which is a function of s/b, to construct a statistic X:

$$
\begin{aligned}
X &= \sum_{j=1}^{N} W(\mathbf{x}_j) \\
&= \sum_{j=1}^{N} W\left(\frac{b(\mathbf{x}_j) + s(\mathbf{x}_j)}{b(\mathbf{x}_j)}\right) \\
&= \sum_{j=1}^{N} W\left(1 + \frac{s_j}{b_j}\right)
\end{aligned}
\tag{3.3}
$$

where j runs over all N events observed, $\mathbf{x}_j$ is the vector of phase-space variables for event j, $(s(\mathbf{x}_j) = s_j)$ and $(b(\mathbf{x}_j) = b_j)$ are the respective signal and background differential cross-sections at $\mathbf{x}_j$. $(s + b)/b$ appears rather than s/b directly because the signal is expected to add to background, not replace it.

Thus intuitive considerations have suggested the form of an improved test statistic. The precise form can be determined by considering the Neyman Pearson Lemma, which states that the best way to discriminate between two possibilities is by the likelihood ratio of the observation. Here the observation is a set of N events at phase-space locations $\mathbf{x}_i$; a *configuration*, C, of events. The likelihood of configuration C given background $b(\mathbf{x})$ is given by

$$
\mathcal{L}(C|b) = \frac{e^{-B} B^N}{N!} \prod_{j=1}^{N} \frac{b_i}{B}
\tag{3.4}
$$

where B is the total integrated background, so $b(\mathbf{x})/B$ is the normalized differential cross-section. The Likelihood Ratio (LR) for the experimental result C is then

$$
\begin{aligned}
Q(C) &= \frac{\mathcal{L}(C|s+b)}{\mathcal{L}(C|b)} \tag{3.5} \\
&= \frac{e^{-(S+B)}(S+B)^N/N! \prod_{j=1}^{N} \frac{s_j+b_j}{S+B}}{e^{-B} B^N/N! \prod_{j=1}^{N} \frac{b_j}{B}} \tag{3.6} \\
&= e^{-S} \prod_{j=1}^{N}\left(1 + \frac{s_j}{b_j}\right) \tag{3.7}
\end{aligned}
$$

where S is the integrated signal.

The Neyman Pearson Lemma proves that this is the optimal statistic: that which maximizes the expected confidence level for a given background and signal [2]. Q can be related to the intuitive idea of a weighted sum by taking logs:

$$\ln Q = \sum_{j=1}^{N} \ln\left(1 + \frac{s_j}{b_j}\right) - S \qquad (3.8)$$

which agrees with the expected form 3.3. For a given signal, S is just an additive constant and can be ignored.

Each experiment will yield a value of Q (or equivalently $\ln Q$), which can replace n as the test statistic. How much better than simple counting Q will perform depends on the distributions involved.

3.2.2   Illustrative Example

As a simple example, consider the case of a new particle manifested as a Gaussian peak on a flat background, as shown in figure 3.2. 4.2 events are predicted from background (B), with an extra 3.6 from signal (S). An experiment results in 4 events distributed as shown, giving a $\ln Q$ value of 1.68. The predicted distributions for $\ln Q$ with and without signal are shown in figure 3.3. The shaded area corresponds to 5% of the signal distribution, and since $\ln Q$ lies within this range the signal hypothesis can be rejected to the 95% confidence level.

Figure 3.3 also shows the same analysis performed using event counting as the test statistic. The overlap between the two distributions is greater, illustrating the advantage of taking into account differential information. The 5% critical region is again shaded, showing that for this experiment one could not reject the signal hypothesis using n as the statistic. Indeed, integrating the background distribution over the same range shows that one would only expect to exclude the signal in 40% of experiments, compared with 49% using the likelihood ratio; the Neyman Pearson Lemma shows that no other statistic could perform better. For simple counting to perform this well one would have to increase luminosity by 30%, but after that improvement the power of the likelihood ratio test advances to over 60%.

---

[2]An extension of the Neyman Pearson Lemma, found in [46].
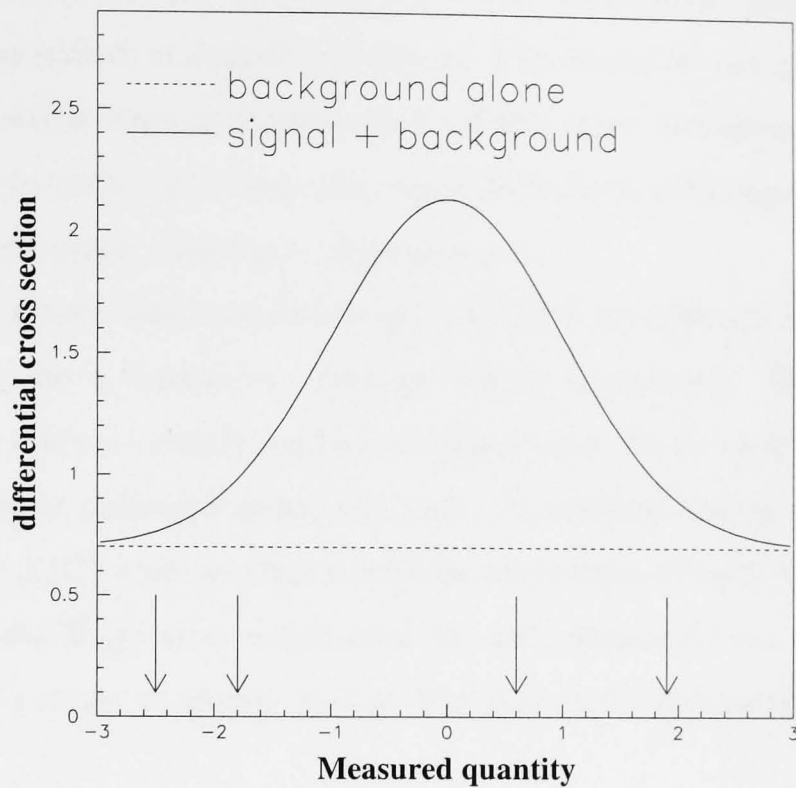
Figure 3.2: Event distribution for the example considered in the text, consisting of a Gaussian signal (solid) on a flat background (dashed). The position of four events generated from a random background experiment are indicated with arrows.
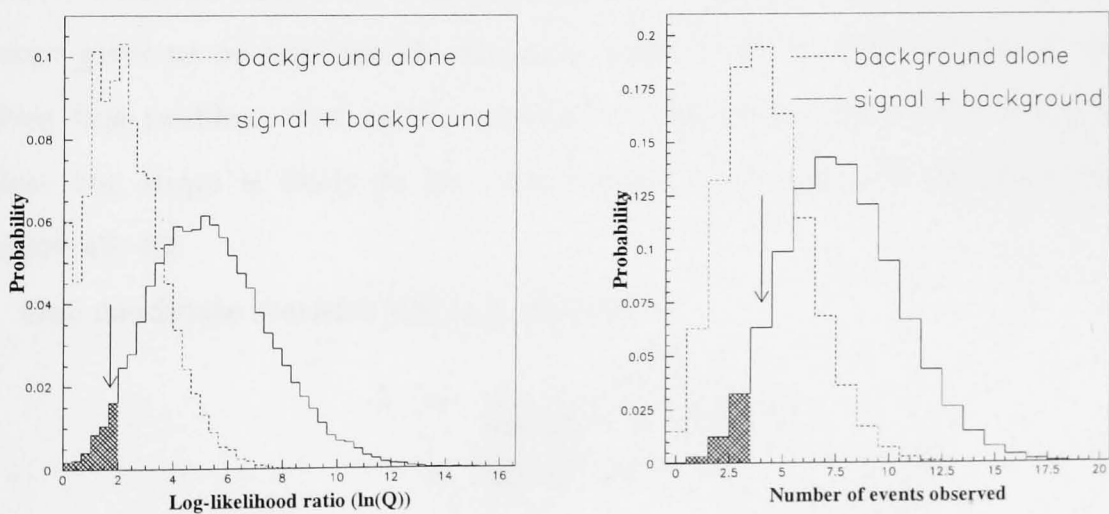
Figure 3.3: Test statistic distribution for the likelihood ratio (left) and simple event counting (right) for the example considered in the text. The experimental result is indicated by an arrow, and the corresponding 95% signal exclusion regions are shaded.

33

3.2.3 Composite Hypotheses in classical statistics

The discussion so far has concerned the choice between two hypotheses which are completely specified, or *simple* hypotheses. This would be the case, for example, if the Higgs particle were predicted with a definite mass. However, since m_H is a free parameter, the choice is between the simple hypothesis of background alone and the *composite* hypothesis covering a range of m_H [3].

We have shown that the Likelihood Ratio Q (or equivalently $\ln Q$) is the optimal test statistic for a comparison between simple hypotheses. However, the signal distribution $s(\mathbf{x}|m_H)$ clearly depends on Higgs mass. So for each different m_H there exists a different optimal statistic $Q(C|m_H)$. In classical theory, one adopts a single test statistic $X(C)$ which is a function of the observation C only. Choosing $Q(C|m_H)$ for a particular Higgs mass would make the test optimal for m_H alone, and close to optimal for a range of nearby masses, but there is no one statistic optimal for all m_H [4].

This is the impasse faced in classical theory; in tuning an analysis to look for one particular value of m_H, sensitivity to other values is lost. Modern searches have adopted techniques to overcome this problem but at the cost of redefining a few terms, as will be described in the following sections.

Another problem with the classical method is how to decide which statistic to choose. Different tests will be more powerful for different values of m_H and classical theory gives us no criterion for choosing between them. Use of Bayesian methods solves this problem, but at the expense of requiring *a priori* assumptions about where the Higgs is likely to be. For further information on Bayesian statistics, see [44, 47–49].

One candidate statistic [43] is λ, defined as

$$\lambda \;=\; \frac{\mathcal{L}(C|b)}{\max(\mathcal{L}(C|s(m_H)+b))} \tag{3.9}$$

$$\;=\; \min\left(1/Q(C|m_H)\right) \tag{3.10}$$

where the maximization is over all m_H considered. Since high values of m_H predict

---

[3] This case is covered in [43], §22.16 under the tests of a *simple* hypothesis.

[4] There are special cases where a single statistic is optimal for all members of a composite hypothesis. A test based on this statistic is called a Uniformly Most Powerful (UMP) test, as discussed in [44].

a very low cross-section and are thus indistinguishable from background, $\lambda \in (0, 1]$, with $\lambda \simeq 1$ for background-like experiments [5].

3.3 Hypothesis Testing Applied to a Physics Search

Classical hypothesis testing as described above is not applied directly to new physics searches. This is perfectly reasonable; the laws of statistics are not written in stone. Statistics was developed as a tool to aid in parameter estimation and decision making, and the worth of a technique depends entirely upon its utility to the case in question. However, confusion arises when terms defined within one context are redefined and then used in another. I have found no modern text collecting and explaining the different definitions and techniques employed in a modern physics search.

Presented here is a guide to some of the methods used in the search for the Standard Model Higgs boson at LEP [50], but many are common to standard practice.

3.3.1 Exclusion and Discovery

Thus far the choice between signal and background has been presented as "either/or". An observation in the critical region leads to a rejection of the signal hypothesis, typically with a significance of 5% (to the 95% CL). However, n outside the critical region does not lead to immediate announcement of a Higgs discovery. The background must be comprehensively rejected before discovery is announced. Long experience has led the PDG [21] to demand a 5σ [6] limit for discovery, equivalent to $(1 - CL_b) < 5.7 \times 10^{-7}$. That is to say, the probability of the observed result being due to a background fluctuation is less than one in a million.

For background $b = 4.2$ shown in figure 3.1, this corresponds to $n > 18$. This is indeed tremendously unlikely for background, but only occurs with probability 5×10^{-4} if one includes the 3.6 signal events. A measurement of n in this range is hardly compelling evidence for the existence of the predicted signal, so even if the

---

[5] Rather confusingly, λ is also known as "the Likelihood Ratio".

[6] Terminology derived from the Gaussian distribution, where the probability of a measurement more than 5σ from the mean is 5.7×10^{-7}

35

signal were present one would be unable to announce discovery. In practice what would happen would be this: for $n \leq 3$ signal would be excluded to 95% CL: for $3 < n \leq 9$ an experimenter would *not* exclude the signal, quote CL_{s+b} and CL_b and eagerly collect more data and for $n > 9$ they would check for underestimated sources of systematic error or turn expectantly to theorists for a revision of predicted cross sections.

How many more events would have to be collected before a discovery could be announced? Keeping the cuts the same, there would be a 50% chance of making a 5σ discovery after repeating the experiment 27 times (ie collecting 27 times the integrated luminosity). Improving these odds to 95% would require a factor 164 increase. However, intuition demands far less stringent proof, and most physicists would be slapping backs well before then (there is a 50% chance of excluding the background to 95% CL after just a factor 5 improvement).

Thus the choice in the first instance is not usually between background or signal, but between signal exclusion and non-exclusion. This is perfectly in line with classical theory, which deals with the probability of making a particular decision, not which decisions to make.

3.3.2 Confidence Levels

As noted in § 3.2.3, the presence of a Higgs of sufficiently high mass would be indistinguishable from background, due to the low Higgs cross-section. In the simple counting experiment described above all such m_H would be excluded when the background fluctuates down into its 5% tail, i.e. when $n = 0$. Thus one experiment in 20 would be expected to exclude *all* Higgs masses to 95% CL, or "exclude the universe". Clearly we would like to guard against this, but it is an inevitable pitfall of the blind application of frequentist techniques.

Again I stress that these techniques were developed for particular purposes and remained in favour due to their suitability for those and other applications. Here they are found unsuitable for our requirements and we are free to develop other methods[7].

The method adopted by LEP and the PDG [21] is a *Modified Frequentist* (MF)

---

[7] One suggested approach is the Bayesian method described in [44, 47–49].

approach. Here the significance of the test is redefined as

$$CL_s = \frac{CL_{s+b}}{CL_b} \qquad (3.11)$$

or the previous definition of significance, divided by the power.

For example, for $n_c = 3$ in the simple counting experiment described earlier; $P(n \leq 3|s + b) = CL_{s+b} = 0.05$, while $P(n \leq 3|b) = CL_b = 0.4$ so $CL_s = 0.12$. A measurement of $n \leq 3$ excludes the signal to the $1 - CL_s = 88\%$ CL by the revised definition, as opposed to the $1 - CL_{s+b} = 95\%$ CL under the previous definition. Under the modified definition, we require $n \leq 1$ for 95% CL exclusion [8]

It should be noted that this revised definition of CL is no longer a probability but a *ratio* of probabilities. However, with the MF method the false exclusion probability is still $CL_{s+b} = CL_s \cdot CL_b \leq CL_s$, so a stated CL of 95% implies a false exclusion rate of *at most* 5%. This satisfies the revised definition of CL given in § 3.2, and as such is called *conservative*.

Notice that the Poisson probability of observing zero events from a mean value μ is $e^{-\mu}$. The smallest critical region we can define is just $n_c = 0$, but for $\mu < -\ln(0.05) = 2.996$ this smallest critical region has a significance $CL_{s+b} = CL_s > 5\%$. This means that signals predicting less than 3 events can never be excluded to 95% CL by a simple counting experiment.

The same result holds for a weighted log-likelihood sum of events, which can be proven as follows. CL_{s+b} is the probability of a result in the critical region given signal plus background. Let CL_{n+b} be the same probability given n signal events. Then

$$\begin{aligned} CL_{s+b} &= P(0|s)CL_{0+b} + P(1|s)CL_{1+b} + P(2|s)CL_{2+b} + \cdots \\ &\geq P(0|s)CL_{0+b} \\ &= e^{-s}CL_b \end{aligned} \qquad (3.12)$$

since the probability of a result in the critical region in the absence of signal is just the probability with background alone. As a result,

$$\begin{aligned} CL_s &= \frac{CL_{s+b}}{CL_b} \\ &\geq e^{-s} \end{aligned} \qquad (3.13)$$

---

[8]Confusion between *confidence level*, CL, and what is often known as the *signal confidence*, CL_s, is an unfortunate consequence of the terminlogy adopted by the LEP Higgs working group.

So a mean signal $s < 2.996$ events can never be excluded to the 95% CL. Since event weights are always positive the minimum value of $\ln Q$ (most background-like experiment) for given m_H again corresponds to zero events seen [9].

For signal indistinguishable from the background (heavy Higgs), $CL_{s+b} = CL_b \Rightarrow CL_s = 1$, corresponding to zero CL. Therefore such alternatives can never be excluded by the MF method, satisfying the demand that we should not be able to "exclude the universe".

Of course a result incompatible with signal *or* background should be investigated to ensure the background is well understood. Usually reasons would be found to make the result more compatible with expectations before publishing. However we do expect unlucky fluctuations every now and then and should not discount the role of chance in any particular result [10].

3.3.3 Composite Hypothesis Testing: an alternative approach

The classical method described in § 3.2 requires a *single* test statistic to be chosen for an experiment and used to perform all significance tests required. The current LEP approach allows us to construct a different statistic for each possible signal – ideally $Q(C|m_H)$ – and perform exclusion tests independently on each. This corresponds to breaking the composite hypothesis down into a set of simple hypotheses and testing each independently against the background.

This method is perfectly valid for exclusion; if the Higgs does exist with mass m_H, then the false exclusion rates calculated using $Q(C|m_H)$ hold whether or not a different test is used for other Higgs masses. The procedure is equivalent to defining different sets of cuts for different ranges of the signal, but carries with it the same complications.

The problem lies with discovery, as can be illustrated with another simple *Gedankenexperiment*. Consider the search for an excess in one of a number of bins in a plot. This scenario could occur in the search for a narrow resonance over a broad mass range, where each bin is broader than the resonance width. Looking at a single

---

[9]This is not the case if signal interferes destructively with background in some region ($s < 0$), reducing the cross-section.

[10]In fact a downward fluctuation of background – observing fewer events than expected – tends to lead to better limits on m_H, so perhaps not so unlucky after all!

bin, we would expect a 1% upward fluctuation of background in, by definition, 1 out of 100 experiments. However, looking at 100 independent bins at least 1 such fluctuation would be expected with $1 - 0.99^{100} = 63\%$ probability. This fact is well known to physicists, who tend not to get excited about a 3σ excess in one bin of a plot.

This feature has been termed the "look elsewhere" effect [51], and shows that the significance of a discovery has to include the fact that we look elsewhere. Above, the discovery significance was set at 1%. The probability of a more significant 5σ discovery in 100 bins is $1 - (1 - 5.7 \times 10^{-7})^{100} \sim 100 \times 5.7 \times 10^{-7} \sim 4\sigma$. As a rough guide, discovery significance is diluted by a factor of the search range divided by the signal resolution.

As stated previously, a 5σ discovery is unlikely to come from a single high energy run at LEP even after combination of experiments [11]. However, the same problem is encountered when we attempt to assess the significance of a smaller deviation from background. The technique to be used to handle discovery is still under discussion [51], but it is likely that the significance of a deviation from background shall be measured by a single statistic, such as the minimum likelihood ratio λ introduced in § 3.2.3.

3.4   Method employed in this analysis

The discussion above illustrates the possible advantages of using a modified likelihood ratio method in a particle physics search. The application in practice is more complicated, principally because the signal and background distributions are never known exactly. They can however be estimated, and this estimate used to construct Q. The better these estimates are, the closer to optimal Q will be.

In this thesis a simple analysis with cuts set by eye is compared to an automated cut optimising procedure and a likelihood ratio analysis. Bias due to finite Monte Carlo samples is observed and investigated for each technique.

---

[11] Given existing limits and predicted integrated luminosities and beam energies.

3.4.1 Bias due to finite Monte Carlo samples

Background and signal cross-section estimates come from a finite number of Monte Carlo events distributed in phase space. In principle, it would be possible to define cuts using little isolated acceptance regions around every signal event, making them small enough that no background events are included. The signal efficiency would then be 100%, with 0 expected background. These estimates are clearly biased, as could be verified by applying the same cuts to an independent set of Monte Carlo events.

The bias above is obvious, but the same precaution should be applied to a less sophisticated analysis technique. In a simple "cut and count" analysis, statistical fluctuations can lead to clusters of background events, which can be simply removed by a slight shift in a cut. This is a problem with background events in particular, because signal events have much higher granularity in the search region. Any bias thus introduced can easily be removed by using an independent set of Monte Carlo events to estimate efficiencies.

Given a Monte Carlo event sample, the simplest method would be to use half the events to define the analysis (training sample), saving the other half to independently measure the result (test sample) [12]. It is in the cases when splitting the sample might have a significant effect on the result that the split must be performed: a fluctuation due to limited Monte Carlo statistics can be exploited to produce a biased result, as shall be seen in chapter 5. The more optimal an analysis, the more carefully the experimenter has to guard against bias.

---

[12] A 50/50 split is suggested by Laplaces' Principle of Insufficient Reason.

Chapter 4

Data selection

4.1 Introduction

This chapter provides a brief description of the real data and simulated Monte Carlo samples used in the analysis. Real data (or 'data') acquisition is described in § 4.2 and simulation for signal and background processes in § 4.3. The track and event selection applied to these samples are described in § 4.4 and § 4.5.

4.2 Real data sample

Analysis was performed on data collected during the 183 GeV run of the LEP accelerator, during the latter half of 1997. The integrated luminosity collected during this time was determined using the STIC calorimeter, identifying low angle Bhabha scattering events $e^+e^- \longrightarrow e^+e^-$. This process has a high cross-section well determined by QED theory at LEP centre of mass energies, and the simple signature of back-to-back, highly energetic electrons. The integrated luminosity determined in this way was 53.95 ± 0.08 pb^{-1}.

The signature for Higgs events in the neutrino channel is missing energy, and a dominant background process is Z^0 *radiative return* with jets and one or more hard photons, described in § 4.3. Therefore strict demands had to be placed on calorimetry performance; to ensure both good jet energy reconstruction and full hermeticity to capture radiated photons. Only events with all calorimeters operating above 90% of maximum performance were considered, with the same demand placed on the TPC as the pivotal tracking detector.

The integrated luminosity surviving these cuts was 51.59 ± 0.08 pb^{-1}.

4.3 Monte Carlo sample

4.3.1 Background processes

A number of different known Standard Model processes contribute to the total cross-section visible at LEP2. This section covers the generation of background channels, along with a brief description of their properties.

Two-photon physics

This process accounts for a significant fraction of the event rate at LEP2. As shown in 4.1, it can be seen as an interaction between two photons radiated by the initial state particles and is thus connected to the electron radiator function, which governs Brehmstrallung and initial state radiation. Since the cross-section for both of these processes falls rapidly as a function of photon transverse momentum, two-photon events tend to be (a) low energy, (b) low multiplicity and (c) boosted forward or backward along the beam. As such they are easy to cut against, however the high event rate means they still have to be treated as a significant background at this stage. The photons require a charged current loop to interact, which can be provided by either quarks or leptons, but only the former can pass the hadronic selection described below.

Also due to the high rate, statistics are relatively low for events generated from the bare matrix element. This leads to a large uncertainty in the two-photon contribution to total background. Applying cuts at generator level to preselect events likely to pass a hadronic selection (and look anything like the Higgs signal) provides a *biased* sample with far higher statistics. As long as equivalent cuts are applied to data, one is free to use a biased sample in the analysis.

In fact, cuts are always applied at generator level to avoid infinite poles in the matrix element. These poles are clearly not physical, but arise from the failure of low-order perturbation theory to fully describe the physical process involved. However, they tend to be associated with very low energy (*infra-red* or *soft*) interactions: corresponding in this case to events with soft, collinear photons with low transverse momentum. Such events are removed by the first few cuts described below and do not contribute to the Higgs background.
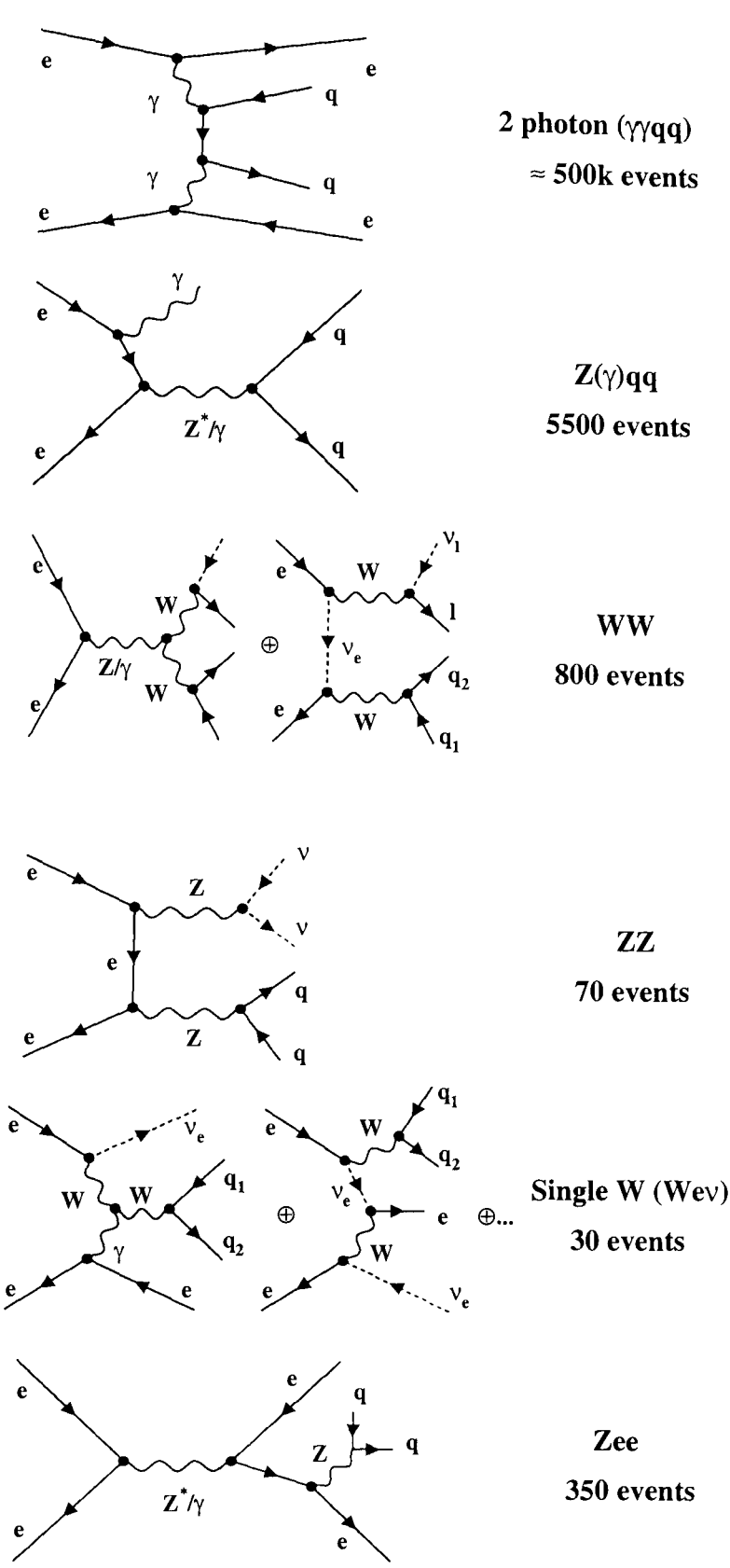
Figure 4.1: Standard model background processes, along with mnemonic names and approximate event rates

Biased two-photon events were generated with cuts of:

- $E_T > 4$ GeV

- $E_{fwd}/E_{vis} < 0.7$

where E_T is event transverse energy[1], E_{fwd} the total energy deposited within 30° of the beam pipe and E_{vis} is the total visible energy in the event.

Simplified theoretical concepts state that a total cross-section for two-photon interactions can be described by a sum of three components: a non-perturbative term describing a soft hadronic part by a Vector-meson Dominance Model (VDM); a perturbative term describing a point-like coupling of the photons to a quark-antiquark pair by the Quark Parton Model (QPM), and a term for the hard scattering of the partonic constituents of the photon; the so-called resolved photon contribution (QCD). These three contributions are modelled separately, with care taken to avoid double-counting through overlap between the models. The contributions from each process are shown separately in table 4.1.

Hadronic Z^0 events

LEP2 runs at energies well above the Z pole, so classic s-channel Z production no longer dominates as it did at LEP1. However, it is still an important process, contributing via the diagram shown in figure 4.1.

The principal diagram is still s-channel production of a now off-shell Z or photon, which then decays in the usual manner. Hadronic decay modes contribute to the background in this search; b quark decays in particular. These events should have far too much energy to be mistaken for the Higgs, but if the resultant jets are mismeasured then they can resemble a heavy Higgs event.

The other major contribution is from *radiative return* to the Z pole. This is where the initial state electrons radiate one or more hard photons before producing an on-shell Z boson, as shown in figure 4.1. Cutting against hard photons reduces this background but, as for two-photon events, the radiative photons are highly peaked in the forward direction. If all photons are lost down the beampipe then these events can resemble the Higgs. Cutting on the polar angle of missing momentum reduces

---

[1] E_T is the sum over all particles of $E_i sin\theta_i$, where E_i and θ_i are particle energy and polar angle.

the contamination – if all missing energy is due to lost photons, then the missing momentum vector should point down the beam. However, mismeasured jets can again contribute to a signal-like contamination from this channel.

Studies with a number of event generators [52,53] have shown that the differential cross section in the region of the radiative return peak is sensitive to differences in the treatment of initial state radiation (ISR). This fact will be important later in accounting for discrepancies between observed and predicted event rates around the Z^0 pole.

WW physics

One major motivation for LEP2 was an accurate measurement of W boson mass and width from the controlled production of W pairs. The highest order Feynman diagrams contributing to this process are shown in figure 4.1. WW events are classified according to the W decay modes: *hadronic* where both W's decay to quarks, *leptonic* when both decay leptonically and *semi-leptonic* with one leptonic and one hadronic decay.

The semi-leptonic decay topology consists of two jets and an independent, high energy lepton. This can contribute background to the $H\nu\bar{\nu}$ search when the lepton is lost down the beampipe or mismeasured. If the lepton is a τ then it can lose a large fraction of energy to neutrinos during decay and again resemble the signal – particularly if the resulting visible decay products are close to a jet.

This background is further suppressed by the low probability of beauty production (certainly not two b quarks), but secondary vertices from charm quark and τ decay can contribute an occasional b-tag.

ZZ production

183 GeV lies on the threshold of on-shell ZZ production. One diagram for this process is shown in figure 4.1. Due to phase-space limitations, one Z tends to be produced close to on-shell, while the other is pushed well off-shell. The cross-section at 183 GeV is as yet small (1.25 pb, corresponding to 68 events per 50 pb^{-1}), but the process becomes more important at higher energies.

The main background contribution arises when one Z decays to neutrinos and the other to b quarks, with approximately $2 \times 0.2 \times 0.7 \times 0.15 \times 68 \sim 3$ events ex-

pected. These events are indistinguishable from signal and thus form an irreducible background for Higgs close to the Z mass. In this analysis, efficiency for a 90 GeV/c^2 Higgs lies around 30%, so we expect a background contribution of about one event. This is twice the actual contribution observed, but that is due to the fact that one Z tends to be well off-shell, and if this boson decays hadronically it does not resemble a 90 GeV/c^2 Higgs.

Single W production

There are a number of processes contributing to single W production at LEP2, as illustrated by figure 4.1. The highest cross-section is for a W associated with one of the initial state electrons (as can be seen from the figure) and a corresponding neutrino, so the channel is also known as Weν. For this process to contribute to Higgs background one has to somehow lose the electron, but since it tends to be forward and disappears down the beampipe in approximately 85% of cases that is not uncommon. B-tagging again reduces this background, but there remains some charm contamination.

4.3.2 Summary of background processes

Table 4.1 gives a summary of the background channels described above, where N_{stat} is the "number of statistics" in each channel, or the ratio of events generated to events expected from the $\mathcal{L} = 51.59$ pb^{-1} collected, given channel cross-section σ:

$$N_{stat} = \frac{N_{gen}}{\sigma\mathcal{L}} \tag{4.1}$$

4.3.3 Signal simulation

Signal events were simulated using the HZHA generator [22], interfaced with JETSET [39] for hadronization. A summary of generated event samples is given in table 4.2.

4.4 Track selection

Good agreement between real data and fully simulated Monte Carlo events demands three conditions: (a) the physics processes contributing to data are well understood.

Physics channel	Generator	Cross section (pb)	N_{stat}
$\gamma\gamma$ (VDM)	BDKRC	550.0	14.3
$\gamma\gamma$ (QCD)	TWOGAM	374.0	3.1
$\gamma\gamma$ (QPM)	BDKRC	122.7	6.5
$Z(\gamma)qq$	PYTHIA	106.7	186.5
WW	PYTHIA	15.44	53.8
ZZ	PYTHIA	1.34	88.7
Weν	PYTHIA	0.60	277.4
Zee	PYTHIA	6.81	13.7

Table 4.1: Simulated data samples for the background processes described in text, and shown in figure 4.1

Higgs Mass GeV/c^2	Cross section (pb)	Events generated
50	0.240	1200
60	0.210	2100
65	0.187	2100
70	0.163	4500
75	0.138	4500
80	0.110	4200
85	0.079	3000
90	0.042	3000
95	0.007	2400

Table 4.2: Simulated Higgs samples generated using the HZHA generator

(b) the hadronization of quarks into final state particles is correctly described by JETSET, and (c) final state particles interactions within the detector are correctly modelled in DELSIM [41].

Spurious tracks from cosmic rays or the interaction of beam particles with stray gas molecules or the beampipe wall could contaminate our sample. This contamination is reduced by considering only particles coming from a region close to the interaction point [2]. Cuts were made on track *impact parameter* of:

- $|r_{\mathrm{imp}}| < 4\ \mathrm{cm}$

- $|z_{\mathrm{imp}}| < 10\ \mathrm{cm}$

where r_{imp} is defined as the distance of closest approach of the track to the primary vertex in the $r\phi$ plane, and z_{imp} the z coordinate of that point, as illustrated in figure 4.2.
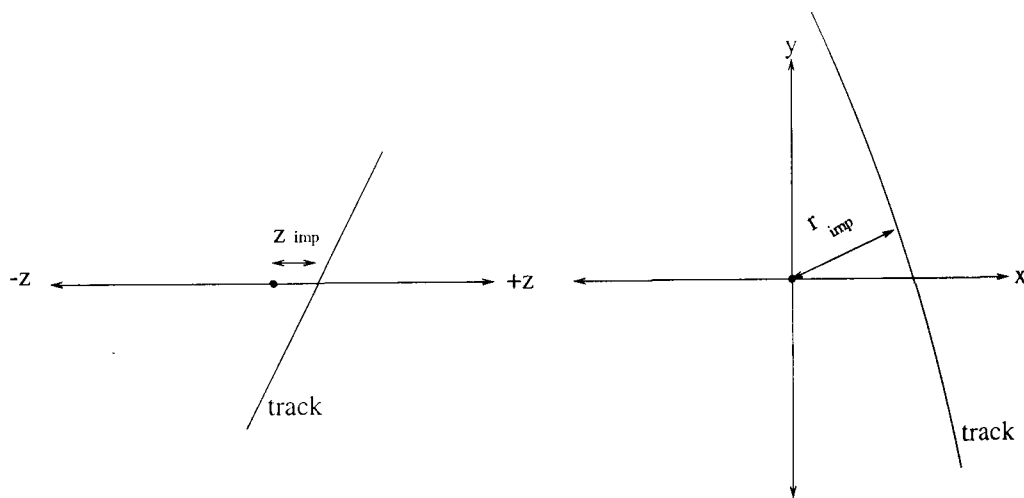

Figure 4.2: Definition of z and r impact parameters

Low energy tracks from soft hadronization and multiple scattering inside the detector are notoriously difficult to model, but contribute little to the global event variables used in this analysis, so were rejected with the following cuts:

- $p_{chrg} > 100\ \mathrm{MeV}/c$

- $E_{\mathrm{neu}} > 200\ \mathrm{MeV}$

where p_{chrg} is the charged track momentum and E_{neu} is the energy of a neutral cluster.

---

[2] An estimate of beam-gas and beam-wall contamination was made by running the selection on data events with the z_{imp} cut changed to 20–40 cm. Contamination was found to be < 0.1 pb.

Poorly reconstructed tracks can often have unphysical momenta with a large associated error. This can occur if an attempt is made to reconstruct a track from a short length of TE through which a straight (infinite momentum) track can be fitted. This is a problem for less than 1 in 600 tracks, but since the average charged multiplicity of a hadronic event is 30, about 5% of all events include a high momentum track contributing a huge uncertainty to many event properties.

An attempt was made to recover these tracks by taking first the momentum of the associated TPC track element, if available, or otherwise the associated calorimetric energy, following the approach of [54]. Otherwise the event was rejected.

4.5 Hadronic selection

A loose hadronic selection is applied to focus discussion on background channels relevant to the Higgs search. The Higgs topology under investigation contains two energetic hadronic jets from b quark decay, as described in § 1.4. Low energy, low multiplicity events not relevant to this analysis were removed by the following cuts:

- $N_{chrg} > 7$

- $E_{chrg}/E_{CM} > 16\%$

- $|\cos\theta_{thrust}| < 0.98$

where N_{chrg} is the number of charged particles in the event and E_{chrg}/E_{CM} is the ratio of the total energy carried by charged particles in the event to centre of mass energy (183 GeV). The low multiplicity, low energy events removed by these cuts dominate the event rate at LEP2 (mostly Bhabha and two-photon scattering, described previously). The thrust axis is defined by the direction of the unit vector $\mathbf{n}$ which maximizes thrust T, defined as

$$T = \max_{|\mathbf{n}|=1} \frac{\sum_i |\mathbf{n} \cdot \mathbf{p}_i|}{\sum_i |\mathbf{p}_i|} \qquad (4.2)$$

where $\mathbf{p}_i$ is the momentum of particle i. For back-to-back jets $T \sim 1$ and the thrust axis follows a jet direction. θ_{thrust} is the polar angle of the thrust axis, so the third cut above removes events with 2 very forward jets, likely to be two-photon background. Higgs signal survives this selection with over 80% efficiency.

Figure 4.3 is a plot of visible energy after these cuts, with the dominant $Z\gamma$ background channel highlighted. The low energy peak corresponds to radiative events, where the initial state photon(s) are lost in the beam.

Dividing the visible energy distribution into 3 regions, defined as

1. $E_{vis} < 65$ GeV

2. $65 < E_{vis} < 130$ GeV

3. $E_{vis} > 130$ GeV

we see a clear data excess in the second bin, which is dominated by radiative Z events. This 7.4% discrepancy corresponds to a significant 4σ fluctuation.
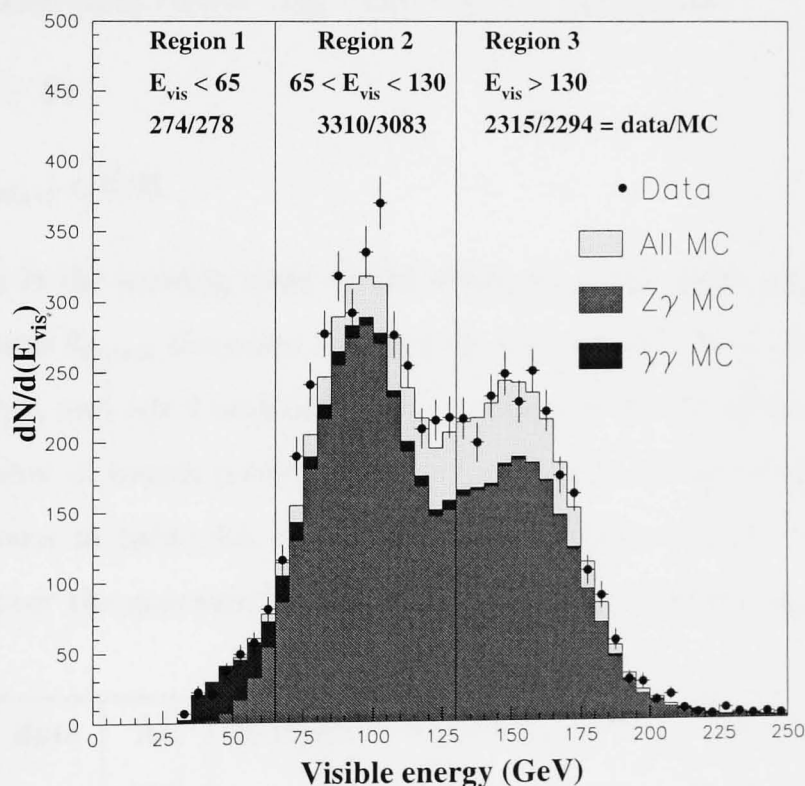

Figure 4.3: Visible energy distribution, after hadronic selection. The dominant $Z\gamma$ background channel is highlighted, along with the residual 2 photon events.

Other analyses on the DELPHI 183 GeV data sample observed the same excess [52, 55], which has been attributed to a mismodelling of collinear initial state radiation in radiative Z events. Several Monte Carlo generators have been compared to the 183 GeV data [52, 53] with results confirming the discrepancy identified in

50

figure 4.3. A new version of PYTHIA (6.1) which is to include improved handling of ISR is currently under development [56].

In order to deal with the problem, $Z\gamma$ radiative return events were identified in the simulation (by demanding total generated ISR energy lost in the beam $E_{ISR} >$ 20 GeV) and re-weighted in order to match the observed visible energy distribution in region 2. This resulted in an overall 10% increase in the cross-section in this region, and an 18% increase in the radiative return cross-section. The contribution of this rescaling to the systematic uncertainty in the background is discussed in § 6.5.

4.6   Tighter preselection

To reduce the data sample, a further selection was made by cutting to remove easily identified background events. The following cuts were made:

1. $M_{miss} > 50$

2. $|\cos\theta_{miss}| < 0.95$

where M_{miss} is the missing mass in the event, θ_{miss} the polar angle of the missing momentum and θ_{thrust} the polar angle of the thrust axis. Cut 1 isolates events with missing energy, and cut 2 removes events with particles lost down the beam.

The number of events passing these cuts for each background channel and real data are shown in table 4.3, along with the efficiency for an 85 GeV/c^2 Higgs. Efficiencies over the generated range of Higgs mass are plotted in figure 4.4.

cut	data	All MC	Z(γ)qq	$\gamma\gamma$	WW	Weν	ZZ	Zee	85 GeV/c^2 Higgs
hadronic	5921	5910	4887	143	722	18.0	49.7	90.2	83.8
cut 1	2896	2845	2414	120	217.4	15.6	17.6	59.5	83.2
cut 2	1180	1161	860.5	52.2	206.3	14.2	13.3	12.6	80.0

Table 4.3: Data and Monte Carlo events remaining after each cut (described in text). The final column shows efficiency for an 85 GeV/c^2 Higgs.
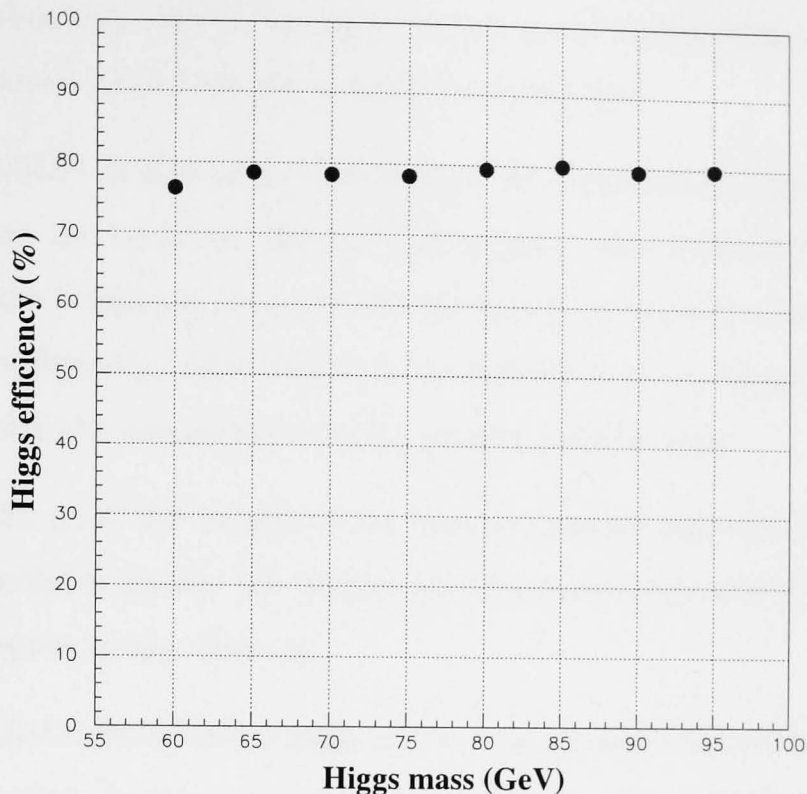
Figure 4.4: Signal efficiencies after preselection

4.7 Discriminating event variables

Event variables were defined to discriminate between Higgs signal and background Monte Carlo. A brief description of the variables used is given below.

- EVIS, the total visible energy in the event

- θ_{miss} is the missing momentum vector polar angle, and XCTH $= |cos(\theta_{miss})|$. Radiative return events with photons missing in the beampipe should have XCTH close to 1.

- Events containing b-quarks are tagged using the standard DELPHI package AABTAG [57]. This computes the probability that all tracks from the event come from a single, primary vertex by considering track impact parameters and evidence for secondary vertices. The probability returned is highly peaked around 0 and 1, so in order to spread out the distribution the variable plotted is BTAG= $\log(-\log(P_{\mathrm{BTAG}}))$. Events containing b quarks have a high BTAG value.

52

- The event was forced into two jets, clustering particles with the DURHAM algorithm [58]. ACOL was then defined as the acollinearity of the jets. or the supplement of the 3-d space angle between them.

- LOGACOP: acoplanarity is defined as the supplement of the jet angle projected onto the $r\phi$ plane. Events with missing momentum due to particles lost down the beampipe, such as radiative return events with a low p_t photon, have low acoplanarity. LOGACOP is the logarithm of the acoplanarity (log again being used to spread out a highly peaked distribution).

- HARDC gives the energy of the hardest charged particle in the event. This discriminates against the background from semi-leptonic WW events with a hard lepton in the detector.

- TKISOL2 is the isolation angle of the most isolated charged track above 2 GeV in the event. Isolation was measured with respect to all other selected charged tracks. TKISOL6 is the most isolated track above 6 GeV. Both of these variables cut against semi-leptonic WW events, where the lepton produced is a τ. This can result in an isolated, relatively low energy track not identified by HARDC.

- ECAL is the maximum calorimeter energy in the event. This identifies hard photons inside the detector from radiative return events, even if they lie inside a jet and have suffered association with a charged track.

- CJET is the closest jet to the beampipe, measured in degrees. Jet reconstruction is more difficult in the forward region, and some of the more stubborn background stems from poorly measured forward jets.

- PISOL gives the angle between the missing momentum and the closest neutral or triggered tagger. This identifies radiative return events with a single photon, either partially reconstructed or lost in cracks between the DELPHI calorimeters.

- PTISOL gives the same angle measured in the $r\phi$ plane. This is particularly useful for identifying radiative return events with 2 photons: one lost in the beampipe, and the other mismeasured or tagged in a crack.

- PZ is the visible longitudinal momentum in the event.

- PTLOG is the logarithm of the event transverse momentum.

- The calorimetric energy between two cones of half-angle 5 and 30° was calculated for every particle above 2 GeV in the event. ECONE was then defined as the minimum cone energy; a low value identifying an isolated track or neutral cluster.

Plots for some of the analysis variables after full preselection are shown in figures 4.5 and 4.6. Real data is represented by solid markers, and shaded histograms show the Monte Carlo background.
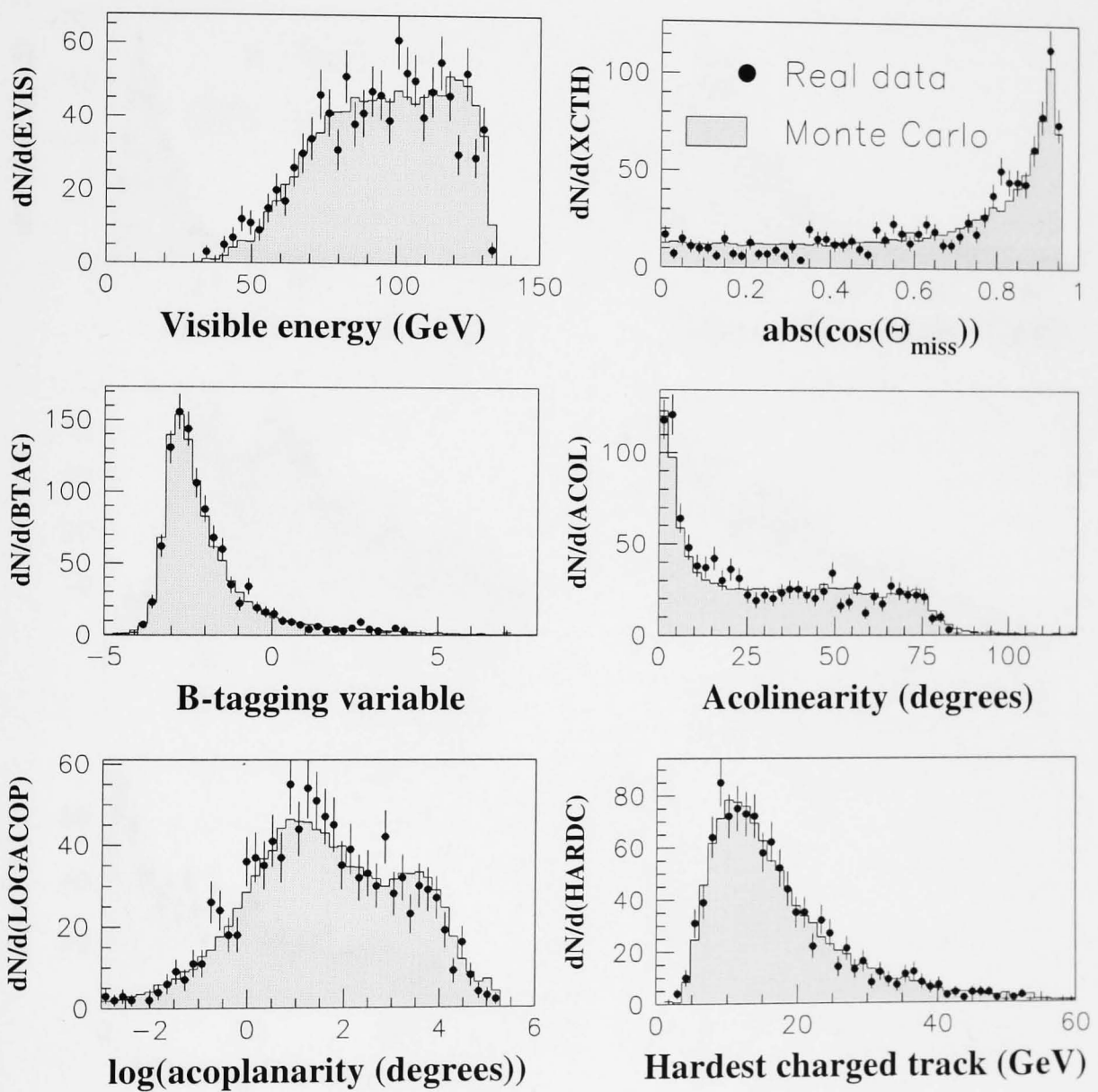
Figure 4.5: Analysis variable distributions after preselection. Points are data, shaded histogram is Monte Carlo background.
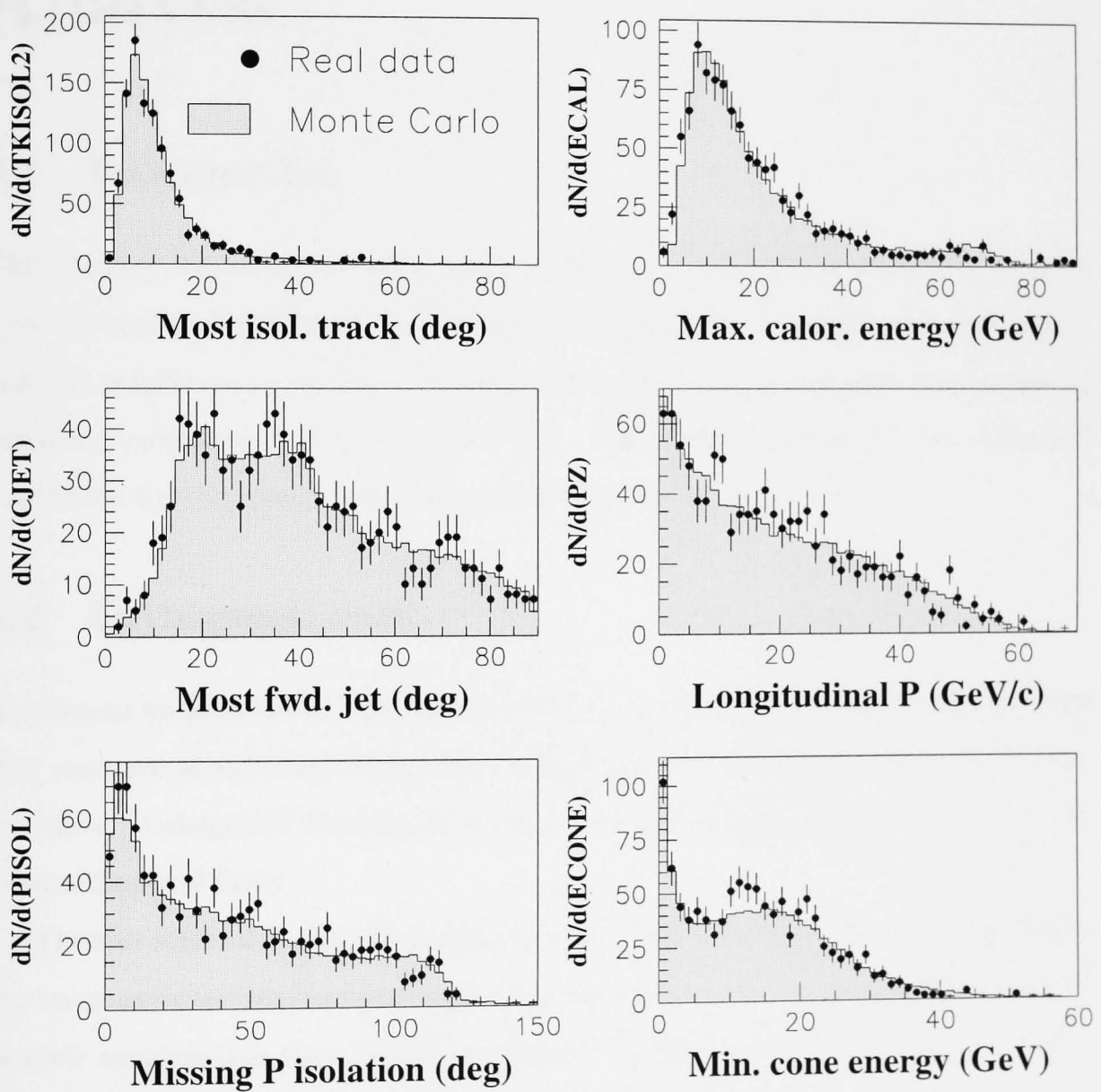
Figure 4.6: Analysis variable distributions after preselection. Points are data, shaded histogram is Monte Carlo background.

Chapter 5

Analysis

5.1 Introduction

This chapter describes the application of analysis techniques described in chapter 3 to the real and simulated data samples of chapter 4. A simple "cut and count" analysis is followed in section § 5.2, with the extension to continuous discriminating variables investigated in § 5.3 and § 5.4. A comparison between real data and simulation for the chosen analysis method is given in § 5.5.

5.2 Orthogonal cuts

A common method used in physics searches is to construct discriminating variables that separate signal from background and apply cuts directly to these. Such cuts are called "orthogonal" because, in a biplot of two discriminating variables, the cuts form orthogonal lines.

The test statistic is just the number of events passing these cuts. Better statistics can be constructed (as has been argued in chapter 3) but to justify the effort involved in their construction they should be able to do significantly better than a simple, standard approach to the case at hand. A simple "cut and count" search is presented here; first with the cuts placed by eye, then enhanced using different optimisation procedures. These can then form the basis of comparison for more sophisticated techniques.

5.2.1 Manual cut determination

Cuts were imposed sequentially on the data sample, using the discriminating variables described in the previous chapter. Cut values were determined by eye on a training sample and efficiencies measured from the test sample, as advocated in § 3.4.1. The result was a background of 1.3 ± 0.2 events, with an 85 GeV/c^2 mass Higgs efficiency of $20 \pm 1\%$ and 1 event remaining in data. It would certainly be possible to improve this result by varying the cut values but this is an inefficient and tedious procedure to perform by hand. Two automated methods of orthogonal cut optimisation are described in § 5.2.2.
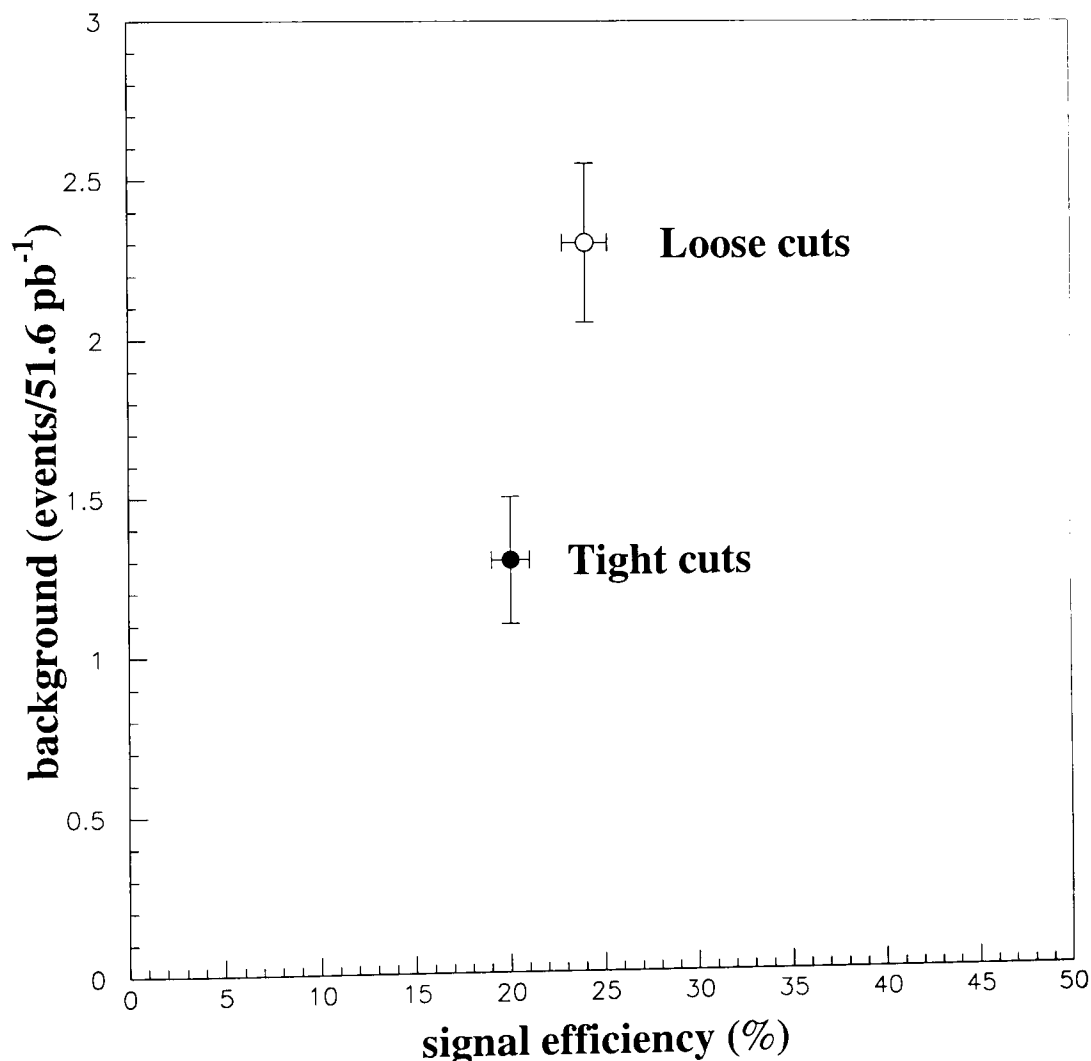

Figure 5.1: The expected performance of an analysis can be summarised as a point in the background-signal plane. The result from setting cuts "by eye" is shown as a solid dot. Slightly loosening the cuts results in the point marked by an open circle.

One question that arises immediately is why stop cutting at precisely the point chosen? Why not tighten the cuts, or relax them to let in more signal at the expense of increasing background? This is the question faced not just by an individual experimenter in trying to "optimise" their analysis, but by a collaboration in attempting to choose between competing analyses. The result of a sequential selection can be summarised by plotting expected background against signal efficiency, as shown in figure 5.1. This plot shows two possible cut selections, with corresponding differences in signal efficiency and background. The question now takes the form, "how should one rate different points on the signal-background plane?"

Any proposed solution should obey certain intuitive demands: an analysis offering increased signal efficiency for a given background rate gives an improvement, as does one with less background for a given signal. If a *score function* is awarded to each point on the s-b plane, with better analyses having a higher (or lower) score, then the contours of this function (projected onto the s-b plane) should therefore have positive gradient. These contours are plotted for the candidate functions s/b and $s/\sqrt{b}$ in figure 5.2, projected onto a shaded contour map above the plotted functions. We can see that scoring using these functions would allow us to tighten our cuts to the point of reducing the signal to zero, which is clearly not optimal. This weakness is demonstrated by the fact that the contours meet at the origin, as seen in figure 5.2. So a candidate score function should have contours of positive gradient, which intercept on the positive s-axis.

The PDG exclusion formula for confidence level CL in the presence of background b and with n_{obs} events observed in data is [21]

$$1 - CL = \frac{P(n \leq n_{obs}|b + s_{\mathrm{CL}}(n_{obs}))}{P(n \leq n_{obs}|b)} \qquad (5.1)$$

where $P(n|b)$ is the Poisson probability of seeing n events from a mean value b, and $s_{\mathrm{CL}}(n_{obs})$ is the number of signal events satisfying this equality. Any hypothesis predicting $s > s_{\mathrm{CL}}$ is rejected to the $CL\%$ confidence level. With signal efficiency ϵ, a signal predicting more than

$$N_{95} = \frac{s_{95}}{\epsilon} \qquad (5.2)$$

events in total is excluded to 95% CL.

A possible score function is $\overline{N_{95}}$ defined as

$$\overline{N_{95}} = \sum_{n_{obs}} N_{95}(n_{obs})P(n_{obs}|b) \qquad (5.3)$$

$\overline{N_{95}}$ is the *expected* exclusion limit given background b and signal efficiency ϵ. The best analysis is that which minimises the expected exclusion limit. Contours of this function are shown in figure 5.3, and follow the required form [1].
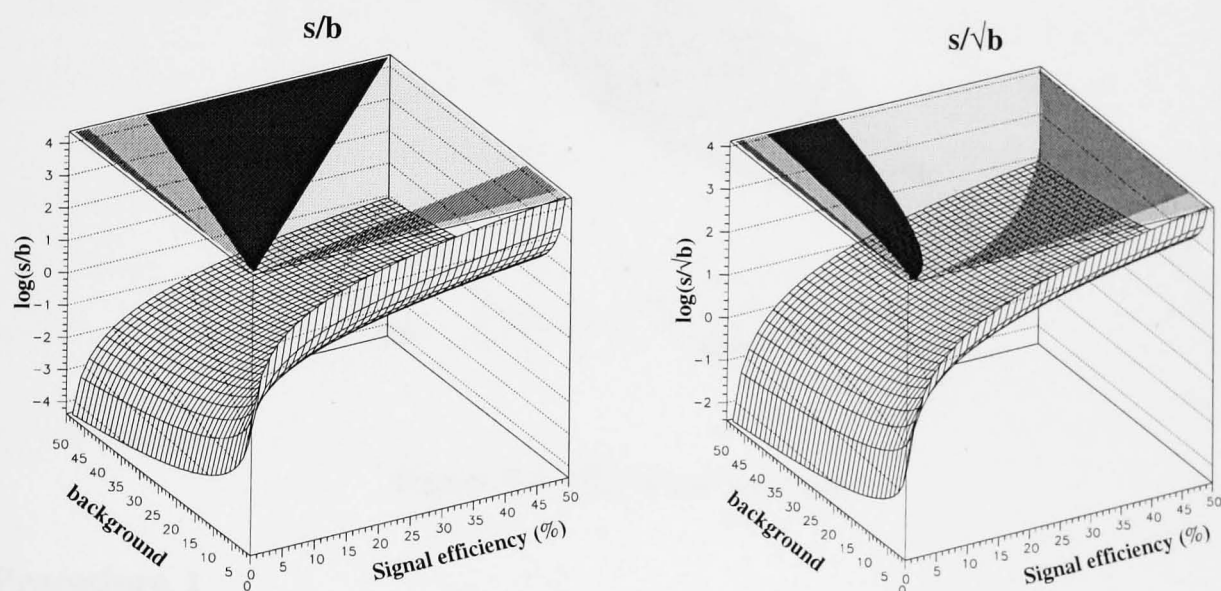

Figure 5.2: Candidate score functions s/b and $s/\sqrt{b}$. Function contours are projected onto the shaded regions above.

This discussion serves to illustrate a general point: having chosen a quantitive measure optimality one can rate different analyses, but any measure of optimality contains a level of arbitrariness.

5.2.2 Automated cut optimisation

Having set the cuts above, it might be possible to increase signal efficiency for given background by slightly tightening and loosening various cuts. However, the large number of variables required to discriminate background from signal makes this a cumbersome task. Instead, a program was written to loop over small steps in each cut value, calculating s and b for each cut combination. Two procedures for orthogonal cut optimisation were investigated, as described below.

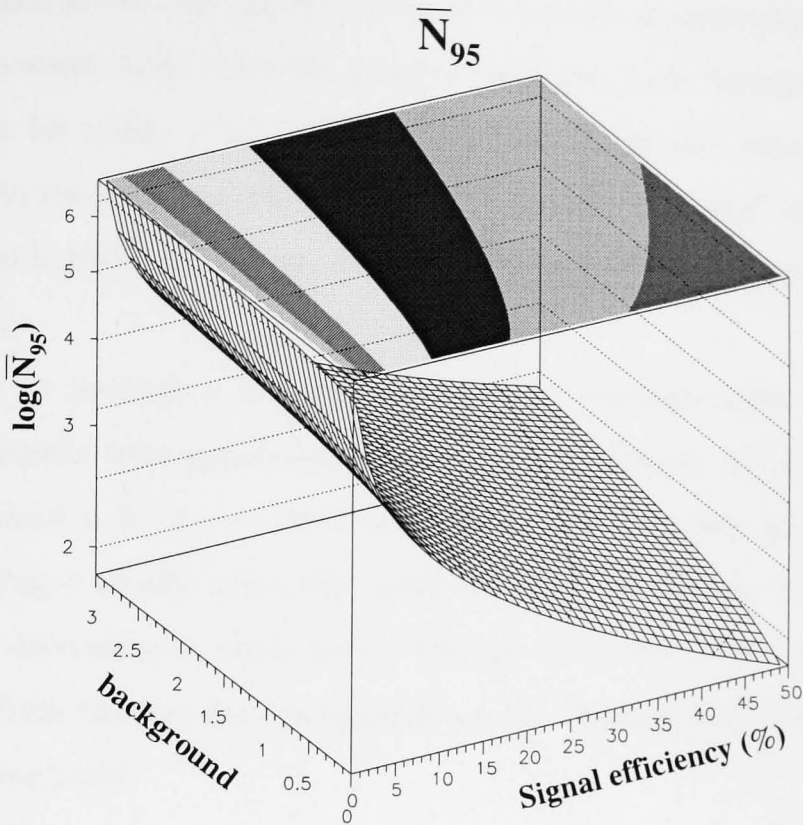[1] Optimising here means *minimising* $\overline{N_{95}}$, not maximising.

Figure 5.3: $\overline{N_{95}}$ score function

Procedure 1

The first method was to loop over a set of 3 cut values for each variable, resulting in a distribution of points on the s-b plane. From the previous discussion the optimal points are bound to be those allowing least background for a given signal, so the maximum signal in each of 100 background bins was stored and plotted as the solid line on figure 5.4. This curve gives a concise summary of a search analysis and is known as a *performance curve*.

Procedure 2

The above optimisation used 3 cut values for each of the 15 variables demanding the evaluation of 3^{15} different cut combinations. An attempt to increase the granularity of the search with 4 cut values would require a prohibitive $(4/3)^{15} = 75$ factor increase in computing time, without significantly improving the coverage of different configurations in cut space.

Measures can be taken to reduce the actual number of combinations considered, but the rapid increase in computation time is a feature of the rather unsophisticated

approach taken above. An improvement can be made by optimising each cut in turn according to some score function, looping back over each variable until no further advance can be made. This approach provides far greater coverage in cut space and results in the improved performance curve marked by solid circles in figure 5.4. The program is also much faster, running in 20 seconds as opposed to 3 minutes for procedure 1.

In order to produce a performance curve to compare with other methods, a number of points were generated by using this algorithm to minimise $b - \lambda s$ for several values of λ. $b - \lambda s = c$ describes a line on the s-b plane, gradient λ, intercept c. Minimising c ideally gives the point on the performance curve with tangent gradient λ: decreasing λ yields points further down the curve. The *optimal* point was chosen from these as the one minimising $\overline{N_{95}}$ (marked with a box) and is known as the *working point*.

5.2.3 Bias through optimisation

Both procedures were trained on half the available Monte Carlo sample (training sample), with event rates estimated from the remainder (test sample). Performance curves for the two samples in figure 5.4 illustrate a clear bias, underlining the importance of a split-sample analysis for optimised techniques – high event granularity in phase space becomes sparse when considered in 15 dimensions. The bias will depend on the method and distributions involved, but a shift of over 3 times the estimated background uncertainty can be seen in figure 5.4.

5.3 A relative likelihood method

Computation of the relative likelihood requires knowledge of the signal and background distributions over 15 dimensional phase space. Were each variable independent, these could be found by taking the projected distributions $\mathcal{L}_i(x_i)$ independently for each variable x_i and constructing the full likelihood

$$\mathcal{L}(\mathbf{x}) = \prod_{i=1}^{nvar} \mathcal{L}_i(x_i) \tag{5.1}$$

Unfortunately, some of the variables used in this analysis are far from independent. The biplot of longitudinal momentum against visible energy for the $Z\gamma$ background
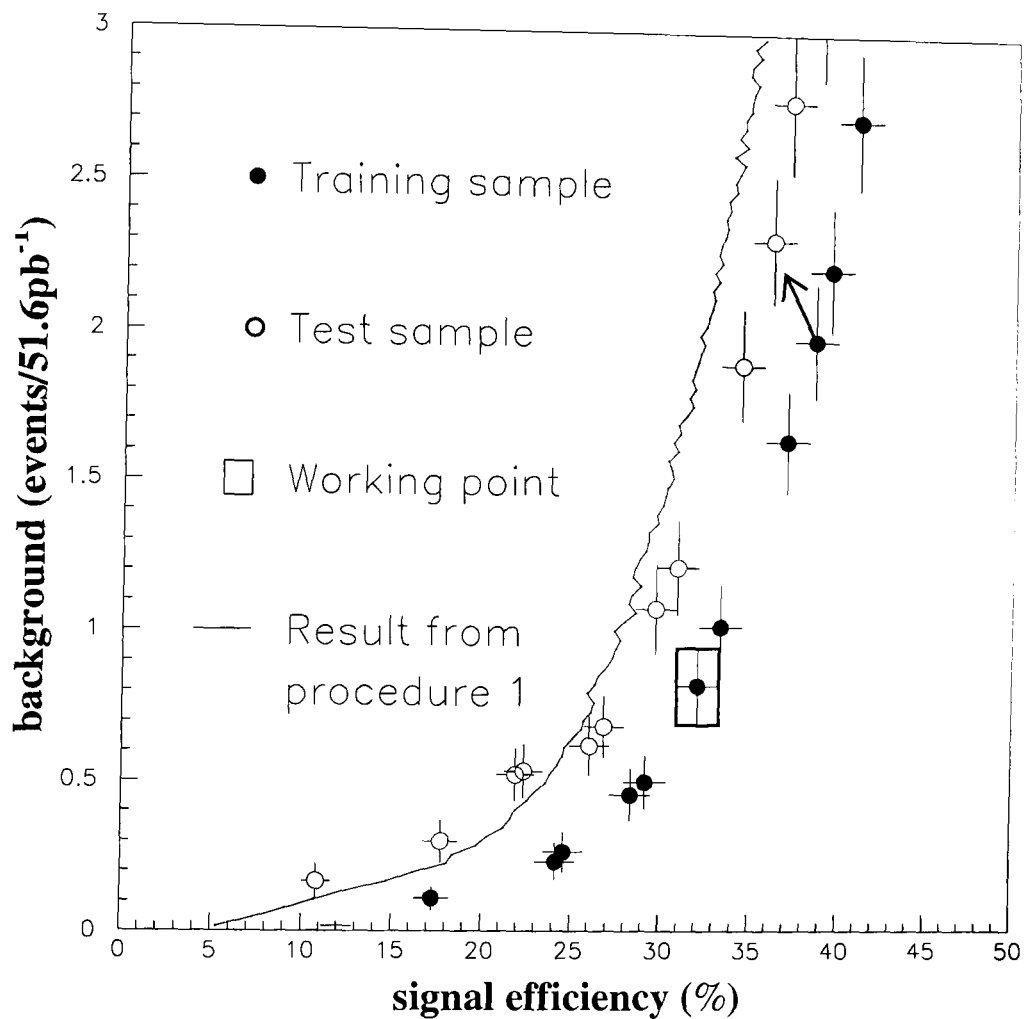
Figure 5.4: Performance curve for procedures 1 and 2. The result from procedure
1 is given as a solid line. For procedure 2, solid markers denote the
training sample and open circles the test sample. Association between
points on the two curves is illustrated by the arrow. The working point
chosen by minimising $\overline{N_{95}}$ is marked by a box.

channel shown in figure 5.5 reveals a complicated functional dependence. The concentration at high visible energy corresponds to events where all energy is recovered, while the diagonal bands at low energy are from radiative events with photons lost in the beampipe.
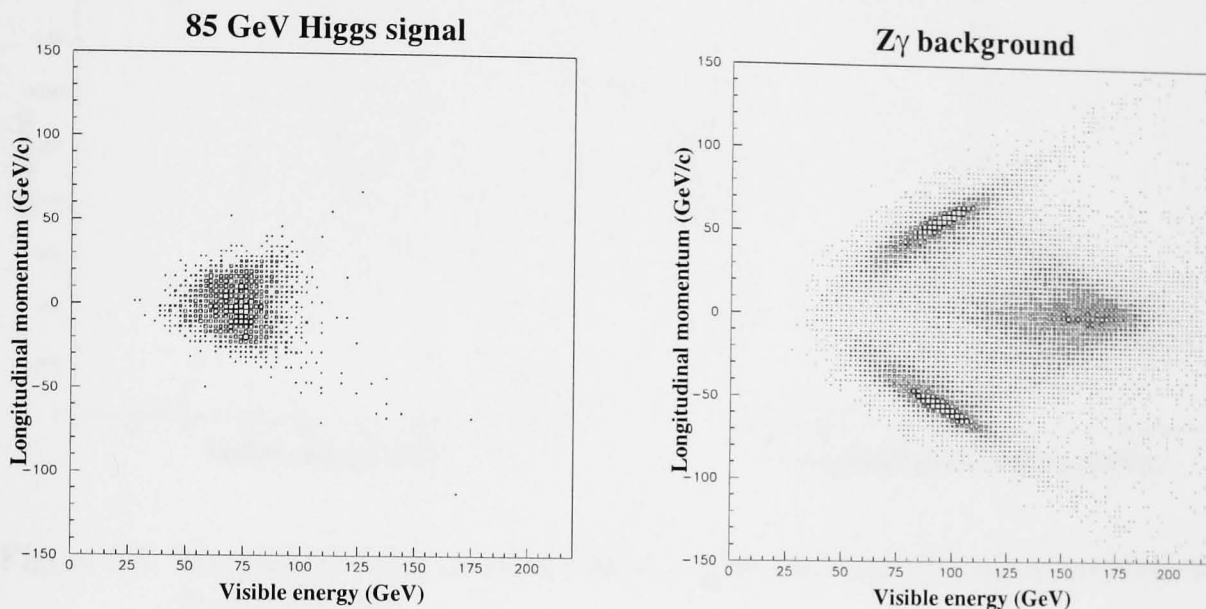

Figure 5.5: Biplot of longitudinal momentum against visible energy for an 85 GeV/c^2 Higgs signal and Zγ background

Figure 5.6 shows the marginal distributions for each variable for the Zγ background which, when independence is assumed, lead to the estimated biplot distribution of figure 5.7. This is not only wrong but disastrous, since background cross-section is now concentrated in the high signal region and the discriminating power of the two variables is completely lost.

For this reason the blind assumption of independence suggested above is unlikely to lead to satisfactory results, but this can be tested by applying it to the analysis above. Signal and background distributions were binned in each of the 15 variables, smooth functions fitted using the HBOOK routine HQUAD [59] and likelihood distributions for signal and background constructed using equation 5.4 above. Figure 5.8 shows signal and background histograms and fitted functions for the BTAG discriminating variable described above.

The likelihood ratio was estimated from the training sample using all 15 variables and equation 5.4 (i.e. ignoring correlations), and its distribution for signal and background test samples plotted in figure 5.9. Cutting on this variable should in
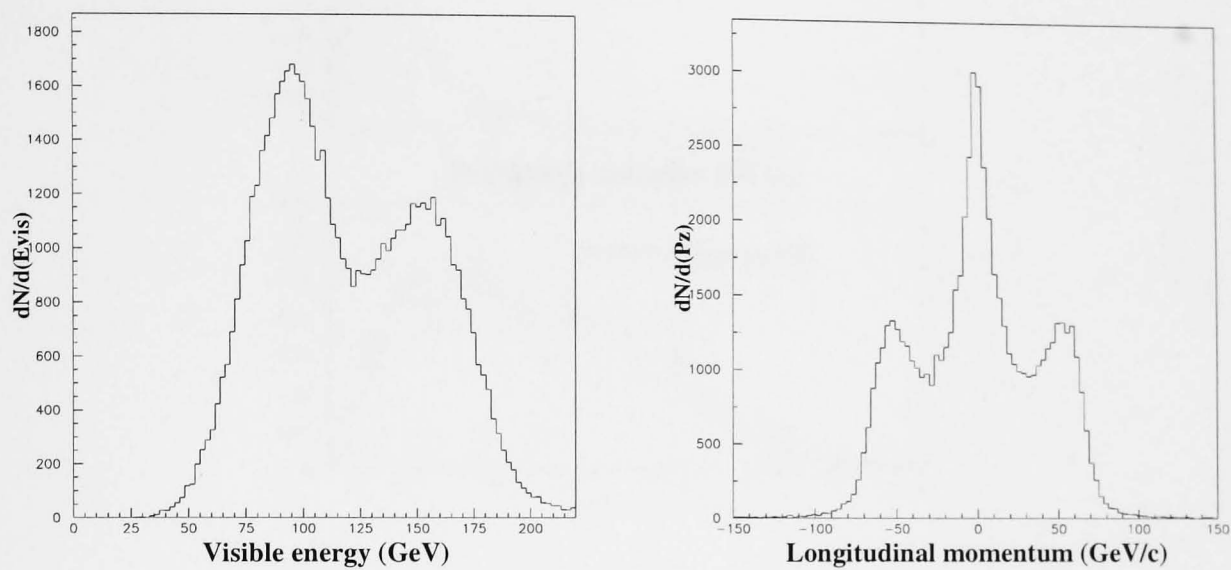
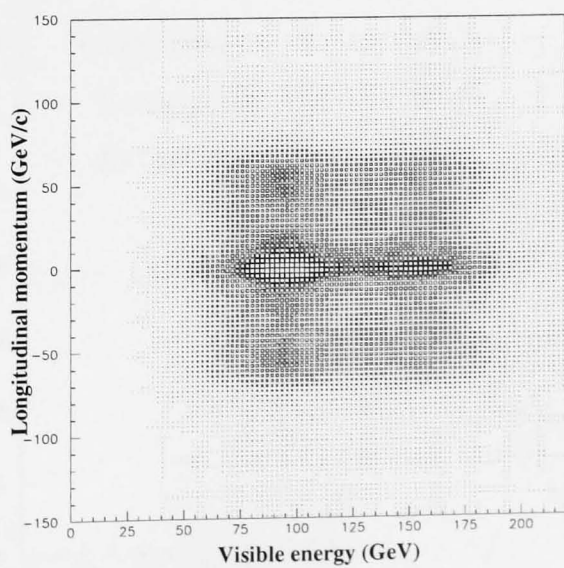Figure 5.6: Marginal distributions of visible energy and longitudinal momentum for $Z\gamma$ background

Figure 5.7: Biplot distribution obtained assuming P_Z and E_{vis} independence
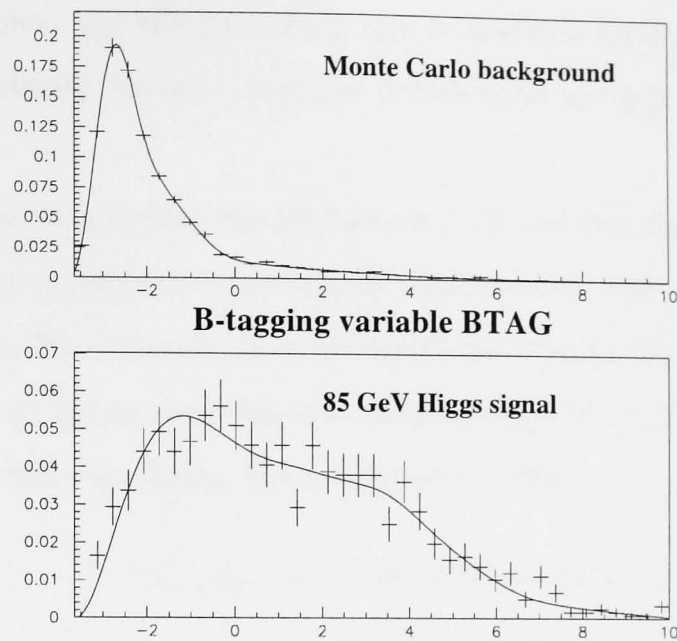
65

Figure 5.8: Signal and background histograms and fitted functions for the BTAG variable described in §5.7. Both histograms are normalised to unity.

principle yield an optimal performance curve, but figure 5.10(a) shows that it actually performs little better than the orthogonal cut analysis described in the previous section.
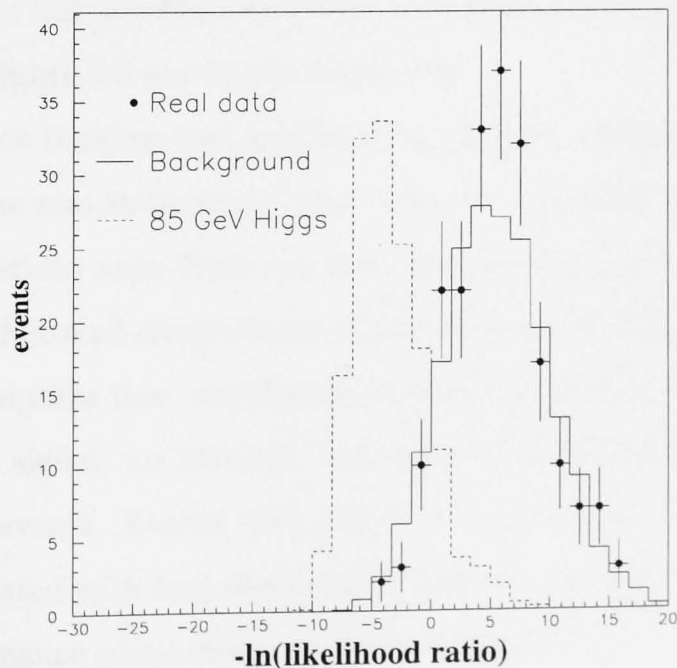

Figure 5.9: Distribution of $-\ln Q$ for real data (points), Monte Carlo background (solid histogram) and 85 GeV/c^2 Higgs signal (dashed histogram). Signal has been scaled by 50 for comparison.

Some improvement can be made by performing two dimensional fits on highly dependent variables, but the gain from this is minimal for a considerable increase in analysis complexity because variable dependence spreads over more than two dimensions.

It is important to note that the problem is with variable *dependence*, not correlation. Independent variables are necessarily uncorrelated, but uncorrelated variables can be dependent. For example, let x be distributed evenly $(f(x) = f(-x) \Rightarrow \overline{x} = 0)$ and consider $y = x^2$ (or equivalently any even function of x). Clearly y is completely dependent on x, but calculating the covariance we find

$$
\begin{aligned}
cov(x,y) &= \; < (x - \overline{x})(y - \overline{y}) > \\
&= \; < xy > -\overline{x} \cdot \overline{y} \\
&= \; \int f(x) \cdot x^3 dx \\
&= \; 0
\end{aligned}
\tag{5.5}
$$

since the integrand is an odd function of x, and so x and y are *uncorrelated*.

The joint likelihood function for independent variables can be factorised $\mathcal{L}(x,y) = \mathcal{L}_x(x)\mathcal{L}_y(y)$, with the implication that knowledge of x gives no information about y (and vice versa). Graphically, this means that cutting a biplot like figure 5.7 vertically through the x axis produces the same section no matter where the cut is made; the variables in figure 5.5 are clearly dependent.

The *correlation* between two variables can always be removed by a rotation, but no matter how the axes in figure 5.5 are rotated the variables will remain dependent. Further complications arise from the fact that correlations for signal, background and different background channels are all likely to be different.

On the assumption that variable dependence is more a problem for the background than for signal, an attempt was made to reduce this effect by removing background-like events. Events with $-\ln Q > 3$ were rejected (see figure 5.9) and the analysis repeated with $\ln Q$ recalculated from the remaining events, yielding the improved performance curve shown in figure 5.10(b).
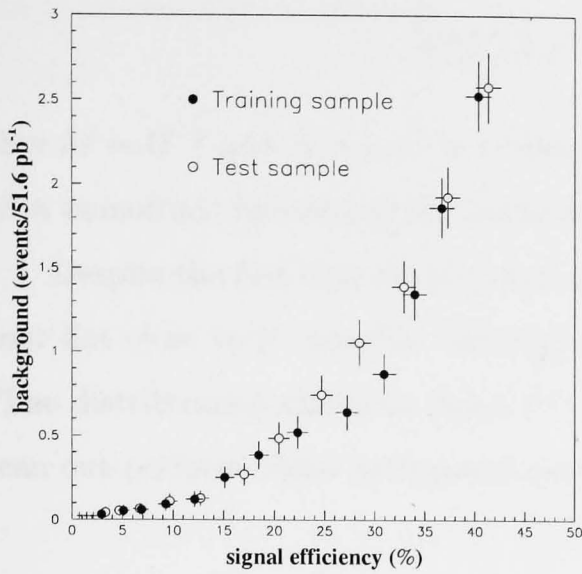
(a) Likelihood estimated using all events
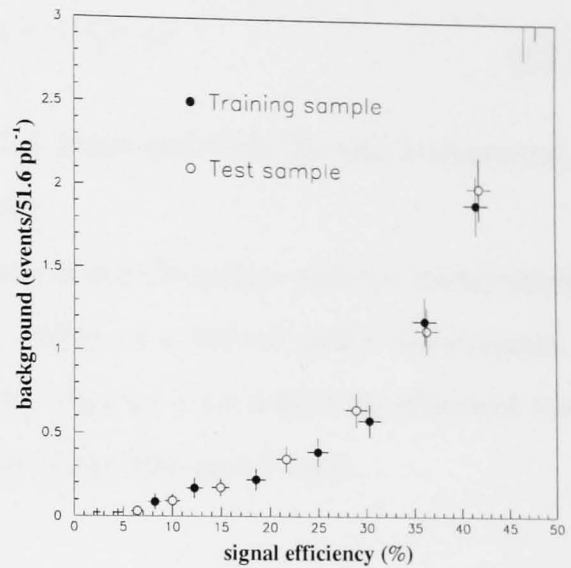
(b) Likelihood recalculated after removing background-like events

Figure 5.10: Performance curves for the likelihood variable. Solid points show the training sample, open circles the test sample.

5.4 Non-orthogonal cuts: a second order discriminating function

Motivated by the success of a similar approach described in [55], a second order function S of the variables x_i was constructed, with

$$
\begin{aligned}
S &= \sum_{i=1}^{nvar} \sum_{j=1}^{nvar} (x_i - a_i) m_{ij} (x_j - a_j) \\
&= (X - A)^T M (X - A)
\end{aligned}
\tag{5.6}
$$

where X denotes the column vector of values x_i, X^T its transpose, A a vector of constants a_i, and M the ($nvar \times nvar$) symmetric matrix with elements m_{ij}. If M is positive definite then contours of S are elliptical: cutting on S cuts a multidimensional elliptical hole in observable space.

Were the signal distribution a multidimensional Gaussian and the background flat in the signal region, then S could be made to correspond to the likelihood ratio and would thus be ideal. This correspondence is achieved by making M the inverse of the covariance matrix C and A the vector μ of mean values, as appear in the

Gaussian probability distribution

$$P(X) \propto e^{-\frac{1}{2}(X-\mu)^T C^{-1}(X-\mu)}$$

(5.7)

For $M = C^{-1}$ and $A = \mu$, P is a function of S alone and thus, for flat background, S a monotonic function of the likelihood ratio.

Despite the fact that the signal distribution is not Gaussian, and the background not flat close to it, one can investigate the utility of a second order discriminant. The distributions shown in figure 5.5 give an obvious case where an elliptical cut can out-perform either orthogonal cuts or the naive likelihood ratio.
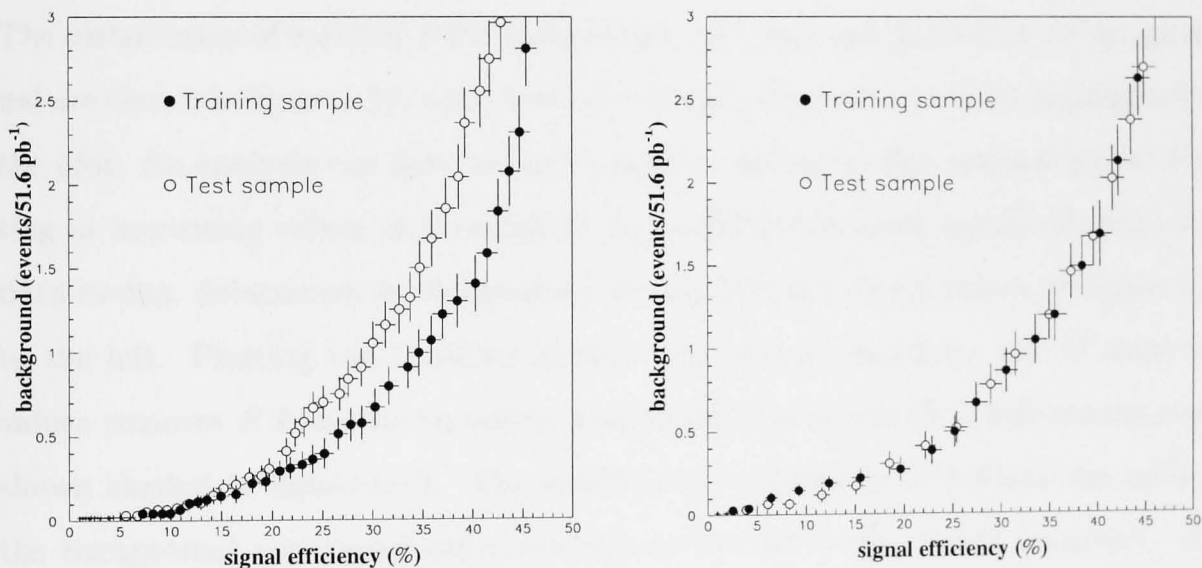
(a) Optimising on the 80 GeV/c^2 Higgs sample

(b) Optimising on the 85 GeV/c^2 Higgs sample

Figure 5.11: Performance curves for the second order discriminants (a) S_{80} and (b) S_{85}, optimised for 80 and 85 GeV/c^2 Higgs, respectively.

A first approximation for M and A can be made by identifying them with C^{-1} and μ above. These parameters can then be iteratively optimised as in § 5.2.2. The optimisation was performed by minimising the background at 40% signal efficiency for an 85 GeV/c^2 Higgs, resulting in the performance curve shown in figure 5.11(b). This curve is almost identical to the result from the relative likelihood method shown in figure 5.10(b). Again there is little bias observed between test and training samples, with the advantage that S is far simpler to calculate than $\ln Q$. As well as out-performing the orthogonal cut analyses of § 5.2, S also provides a continuous

variable to be used in constructing a likelihood ratio test-statistic. For this reason the second order function S is used in the following chapter for the evaluation of limits.

It should be noted that the lack of bias is a lucky coincidence due to the relative homogeneity of test and training samples, not an advantage of the method. The performance curves from optimising using the 80 GeV/c^2 Higgs sample are plotted in figure 5.11(a), and show a significant bias between test and training samples. Clearly, the split-sample approach is still necessary with this technique.

5.5 Comparison with data

The distribution of variable S for background, real data and an 85 GeV/c^2 Higgs signal are shown in figure 5.12, with dominant Zγqq background channel highlighted on the plot. An analysis can then be performed by cutting on this variable alone. Cutting at increasing values of S results in increased background, signal efficiency and data events, determined by integrating the appropriate distributions of figure 5.12 to the left. Plotting the resultant background against signal for one of these cut values removes S from the equation, and yields a point on the performance curve shown shaded in figure 5.13. The width of the shaded band reflects the error in the background and signal estimates due to limited Monte Carlo statistics. The corresponding number of data events passing the same cut on S is also plotted as a function of signal efficiency, and is in good agreement with the expected background.

In the following chapter the S variable will be used to set limits on the Higgs mass. To distinguish between optimisation at different mass points, S_{m_H} shall refer to S optimised at Higgs mass m_H. The plots in figure 5.12 are for S_{85}.
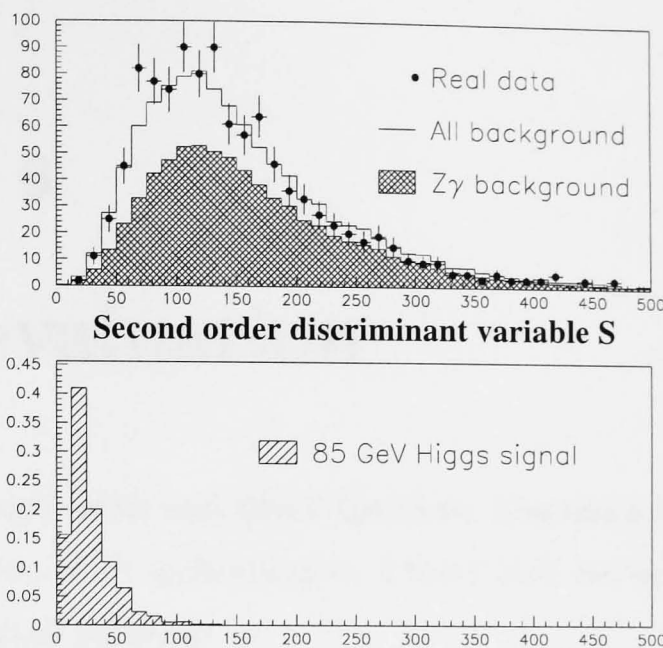
Figure 5.12: Distribution of the second order discriminant S_{85} for Monte Carlo background (solid histogram) and real data (points). The dominant contribution from the $Z\gamma$ background channel is shown as the shaded histogram. The distribution for an 85 GeV/c^2 Higgs signal is given beneath, normalised to unity.
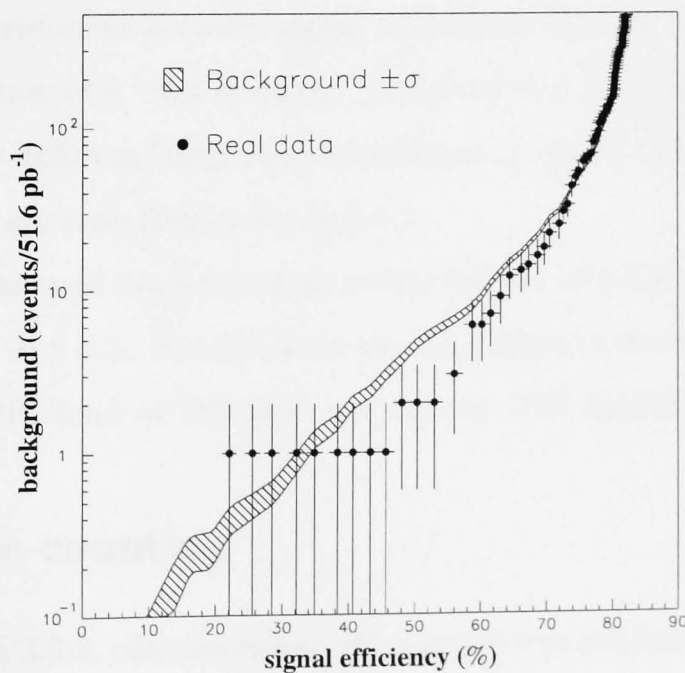

Figure 5.13: Full performance curve for the second order discriminant S_{85}, produced by integrating the distributions of figure 5.12 from the left. The band gives expected Monte Carlo background ($\pm\sigma$), and the points show real data.

71

Chapter 6

Limit evaluation

Neils Bohr supposedly said that if Quantum Mechanics didn't make you dizzy then you don't understand it. I think that the same can be said about statistical inference.

Robert Cousins [47]

6.1 Introduction

The analysis described in the previous chapter is here translated into a Higgs mass limit. A simple counting approach is adopted first, with the single test statistic S_{85} used to discriminate between signal and background in § 6.2.1. Following the expanded definition of a "test statistic" described in § 3.3.3, different test statistics are then used for different Higgs mass hypotheses in § 6.2.2. The advantages of using weighted events are then illustrated in § 6.3.

A brief summary of candidate data events follows in § 6.4, followed by a systematic error study in § 6.5. Results from the $H\nu\bar{\nu}$ channel are then compared to the combined DELPHI limit at 183 GeV and current LEP limits in § 6.6.

6.2 Simple counting

As discussed in § 3.3.3, one can either use a single test statistic to describe the data or one can test each value of Higgs mass independently. Both approaches will be investigated here.

6.2.1 Single test statistic

Limits can either be set using Poisson event counting or the likelihood ratio statistic defined in § 3.2.1. In either case, one wishes to maximize the sensitivity of the search for discovering or excluding the Higgs boson. However, as discussed in § 3.2.3, no single test statistic can have maximum sensitivity for all Higgs masses. One is forced to choose a mass range on which to focus the search.

Experiments preceding the 183 GeV data analysed here set a 95% CL mass limit of 77.5 GeV/c^2 for the Standard Model Higgs [60]. With an upper bound set by the kinematic limit of 92 GeV/c^2, we might choose to focus the search on an 85 GeV/c^2 Higgs. The total number of events predicted in this channel is only 3.7, reduced to under 1.5 after selection; and since a signal predicting under 3 events can never be excluded to 95% CL it will not be possible to exclude this Higgs in a stand alone analysis. One might instead attempt to maximise the probability of discovery, but as was shown in § 3.3.1 a discovery could not be trusted in a channel with such a low event rate.

The situation is analogous to splitting the H$\nu\bar{\nu}$ search into narrow bins of the discriminant variable S. An attempt to find the Higgs in any single bin would be futile; it is only in their combination that a search makes sense. Similarly, it is only in combination with other search channels that the H$\nu\bar{\nu}$ search becomes valid.

The above holds true if the Higgs can only have the properties predicted by the Standard Model. It might be that the cross-section prediction is low, so that the event rate is actually much higher. However with this input into previous searches, the existing limit would itself be higher still. In justifying a stand alone analysis we are forced to search for a particle that looks less and less like the Standard Model Higgs. We are saved by the fact that in the Standard Model the Higgs cross-section falls rapidly after the kinematic limit, so that even if predictions were out by an order of magnitude an 85 GeV/c^2 Higgs might not have been discovered previously.

The results of a stand alone analysis can be summarised by plotting the cross-section exclusion limit as a function of m_H. The test statistic chosen was S_{85}, the second order discriminant optimised for an 85 GeV/c^2 Higgs, with the cut chosen to minimize $\overline{N_{95}}$, as advocated in § 5.2.1. The result was a background of 1.95 ± 0.19 events, with 1 event in data and signal efficiencies as shown in figure 6.1.
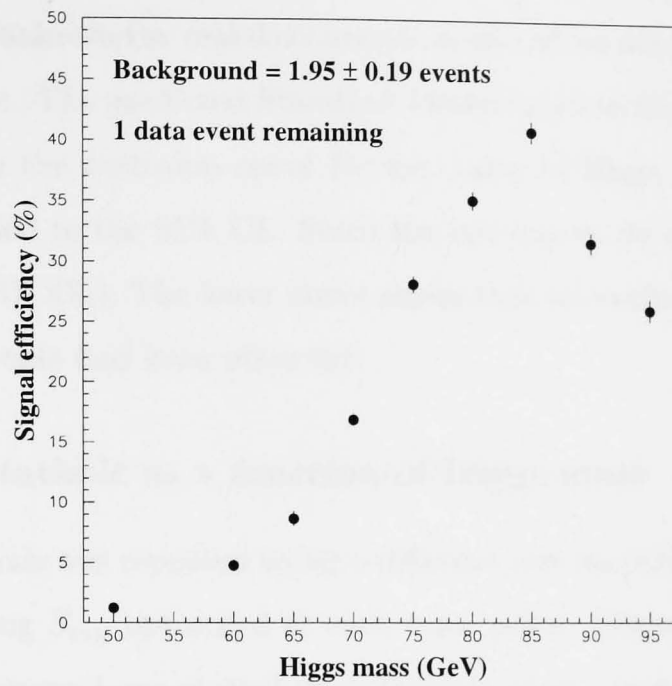
Figure 6.1: Signal efficiency as a function of Higgs mass for the cut on S_{85} described in § 6.2.1.
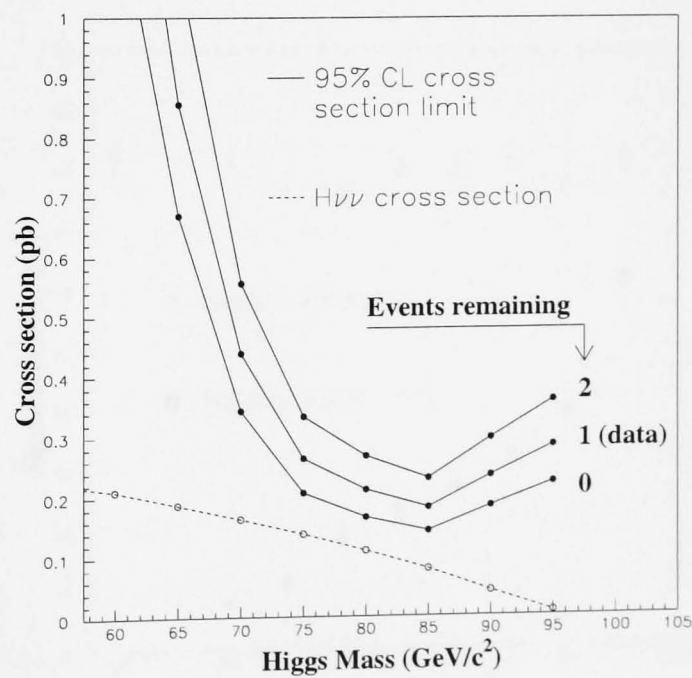

Figure 6.2: 95% CL cross-section exclusion limits for 0, 1 and 2 events observed (solid lines) and Higgs cross-section (dashed line) as a function of Higgs mass. 1 event remains in data, as indicated.

Figure 6.2 shows the cross-section exclusion limit set by Poisson counting. The three solid curves show the exclusion limit for 0, 1 and 2 events remaining in data. Since 1 event remains in the real data sample collected we are primarily interested in the middle curve. The predicted Standard Model cross-section is also plotted; were this to lie above the exclusion curve for any value of Higgs mass, then that mass would be excluded to the 95% CL. Since the two curves do not cross, no exclusion is possible (to 95% CL). The lower curve shows that an exclusion limit could not be set even if no events had been observed.

6.2.2   Test statistic as a function of Higgs mass

The above analysis was repeated using a different test statistic for each Higgs mass; the statistic being S_{m_H} optimised at each mass point. Higgs efficiency and Standard Model background are plotted as a function of m_H in figure 6.3. Efficiency is relatively constant at 40% while the background falls for lower Higgs mass as the dominant WW and $Z\gamma$ channel contributions become less problematic. The flat efficiency is an artifact of the optimisation procedure, which minimised background at 40% signal efficiency.
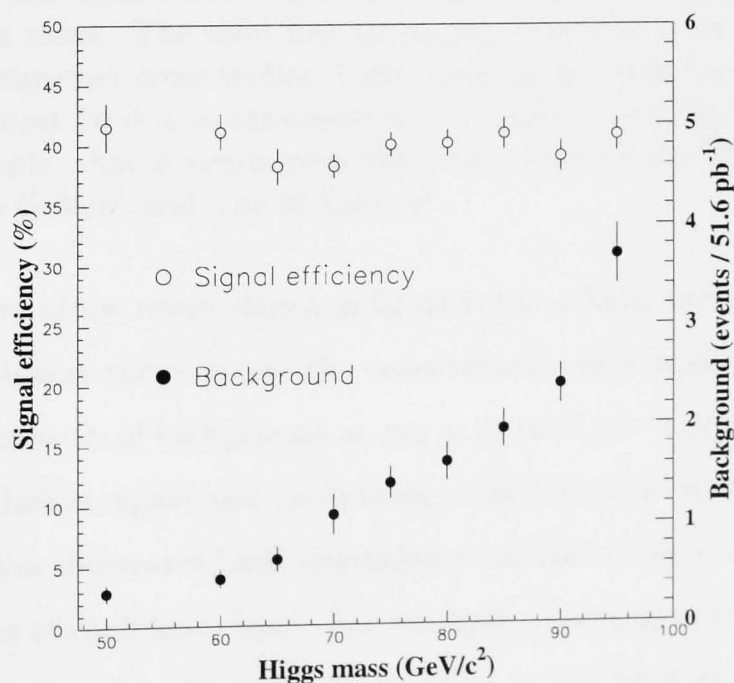

Figure 6.3: Signal efficiency and background as a function of Higgs mass for the cuts described in § 6.2.2.

The resultant cross-section limit is plotted in figure 6.4, showing the Higgs cross-section (shaded area), expected limit and observed limit as a function of Higgs mass. Also shown are the limits that would be set for 0 to 4 events observed in data, from which we can see that, for cuts optimised on the 70 GeV/c^2 Higgs sample, no events pass in data, 1 event at 75 GeV/c^2, 2 at 80 GeV/c^2 etc.
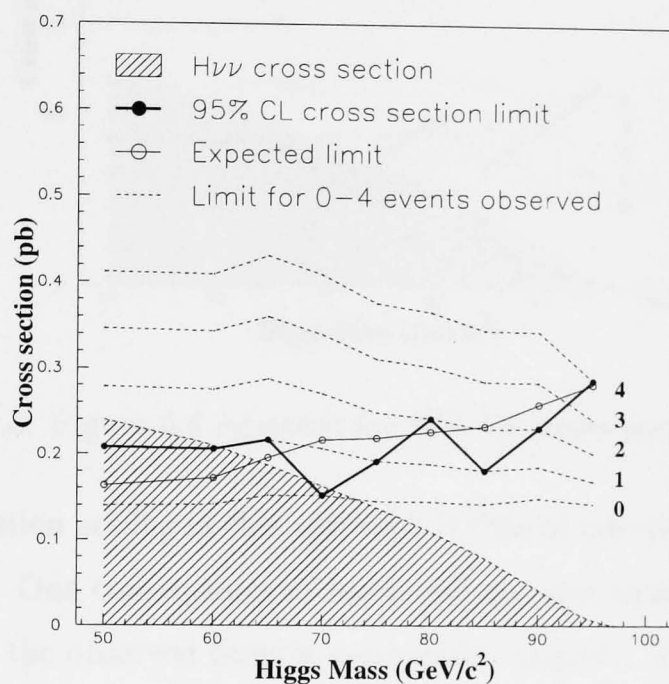

Figure 6.4: 95% CL cross-section exclusion limit, optimising separately on each Higgs mass. The solid line shows the observed limit and the thin line the expected cross-section limit, with signal cross-section shaded. The limits set for 0–4 events observed are shown as dashed lines revealing, for example, that 2 events pass the cuts optimised for 80 GeV/c^2, 1 event at 85 GeV/c^2 and 4 at 95 GeV/c^2.

Interpretations of the result shown in figure 6.4 as a limit are complicated by the fact that the exclusion curve crosses the cross-section curve more than once, due to a downward fluctuation of background at $m_H = 70$ GeV/c^2. It is simplest to opt for a continuous exclusion region and exclude $m_H < 60.5$ GeV/c^2 to the 95% CL.

The fluctuation illustrates limit dependence on the number of events observed and on the choice of confidence level. For example, choosing to exclude to 90% CL leads to the exclusion plot of figure 6.5, resulting in the limit $m_H < 74$ GeV/c^2 to the 90% CL. The choice of the experimenter to summarise their result with a single 95% CL limit forces other interpreters of the data to accept the same limit when they might have been happier with a lower level of confidence.
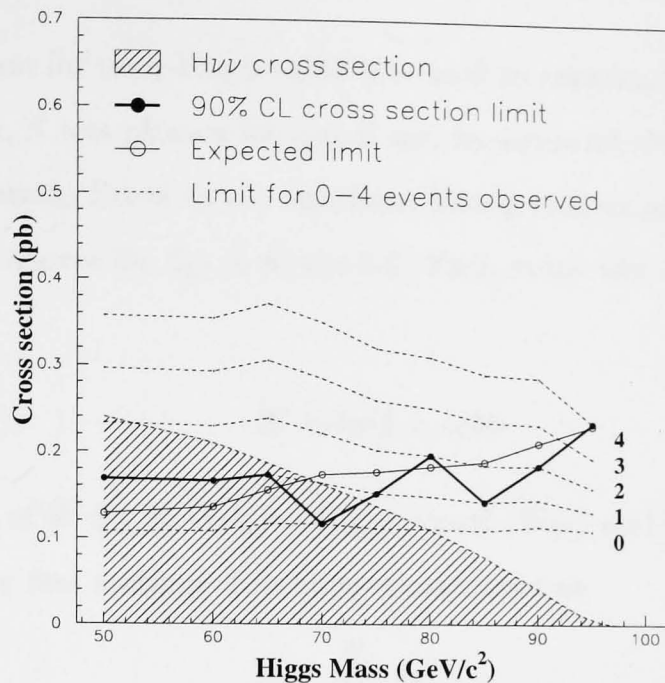
Figure 6.5: Figure 6.4 repeated for 90% CL cross-section exclusion.

Another question arising in this approach is that of interpolation between different mass points. One consequence of hard cuts are that candidates disappear at a certain mass, so the observed limit is necessarily "jagged". Rather than the linear interpolation used to set a 74 GeV/c^2 90% CL limit above, all that can be said is that the candidate disappears suddenly somewhere between 70 and 75 GeV/c^2 and the limit lies within this range. Better precision can be achieved by generating more Higgs mass points, or interpolating S distributions between adjacent masses.

6.2.3 Problems with using simple event counting to set limits

The main problems with this approach to setting limits can be summarised as follows:

- The final result depends on the fine details of where candidates lie with respect to the cuts

- One 95% CL exclusion point is an insufficient summary of the data

- Even in the absence of a signal, the limit can lie anywhere in a broad mass range, depending on the data

The first two problems at least can be solved with a likelihood ratio method.

6.3 Limit setting using weighted events

The S distribution for each Higgs mass was used to construct a likelihood ratio for each event. First, S was plotted for signal and background close to the signal region and smooth functions fitted to the resultant histograms using the HBOOK routine HQUAD [59], as shown for S_{85} in figure 6.6. Each event was then awarded a weight W, where

$$W = \ln(1 + s/b) \qquad (6.1)$$

The distribution of W for 85 GeV/c^2 Higgs signal (W_{85}) and background are shown in figure 6.7. The test statistic T is then constructed as

$$T = \sum_{i=1}^{N} W(\mathbf{x}_i) \qquad (6.2)$$

where N is the total number of events and $W(\mathbf{x}_i)$ is the weight of event i.
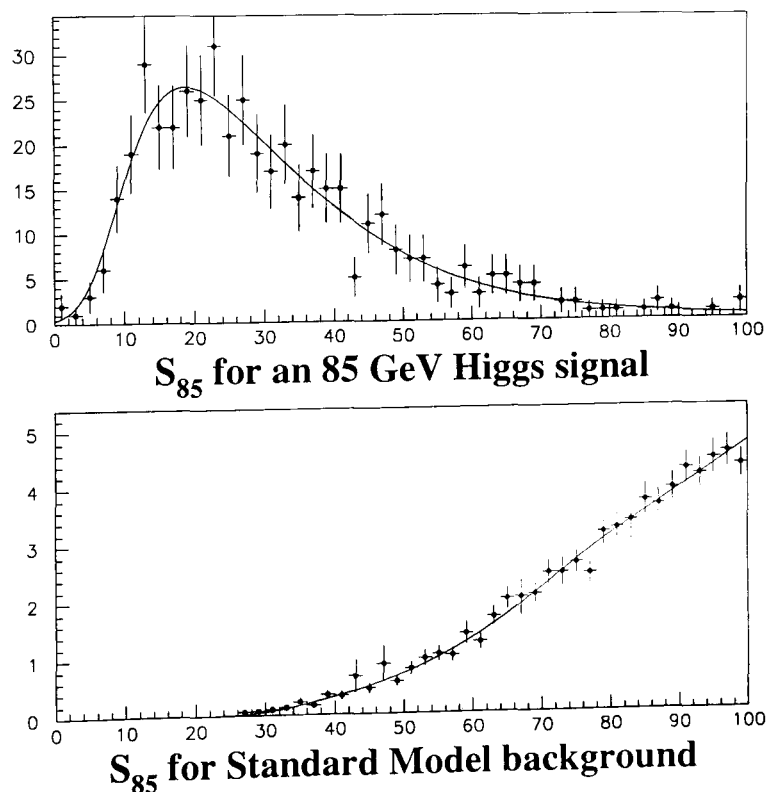

Figure 6.6: Distribution of S_{85} for 85 GeV/c^2 Higgs signal and Standard Model background, with smooth fitted functions.

Signal and background events were then generated according to the distributions of figure 6.7 to produce the expected distribution of T in the presence of signal and

for background alone. High weight events are most important for discriminating between signal and background, so a cut was applied on $W_{85} > 0.012$. The result was a background of 30.3 events, with 25 events remaining in data and 2.93 expected signal events (72% efficiency).

A split-sample approach was again adopted, with functions fitted to S for the training sample and corresponding W distributions generated from the test sample.

1 million simulated experiments were then generated according to the distributions of figure 6.7. The expected distributions for T in the presence of 85 GeV/c^2 signal (T_{85}) and for background alone are plotted in figure 6.8.
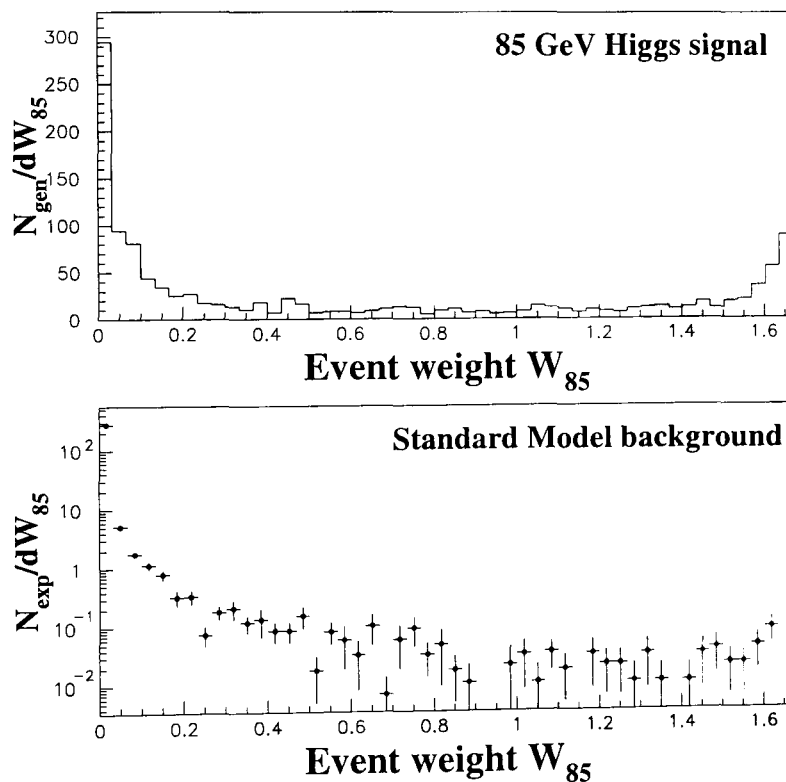

Figure 6.7: Event weight W_{85} distribution for background and 85 GeV/c^2 Higgs signal events.

The value of T_{85} calculated from real data is indicated by an arrow on figure 6.8. Confidence levels are then constructed in 3 stages:

1. The probability of a more background-like experiment from background alone. CL_b, is found by integrating the background distribution to the left, as indicated by the hatched area – here, $CL_b = 42\%$. The expected value of CL_b is obviously 50% and its distribution is flat.

2. The probability of a more background-like experiment in the presence of signal, CL_{s+b}, is found by integrating the signal distribution to the left, as indicated by the cross-hatched area. Here $CL_{s+b} = 9.7\%$.

3. The *significance* of the result is then $CL_s = CL_{s+b}/CL_b$: if $CL_s < 5\%$ then the signal is rejected to the 95% CL. Here $CL_s = 23.1\%$.
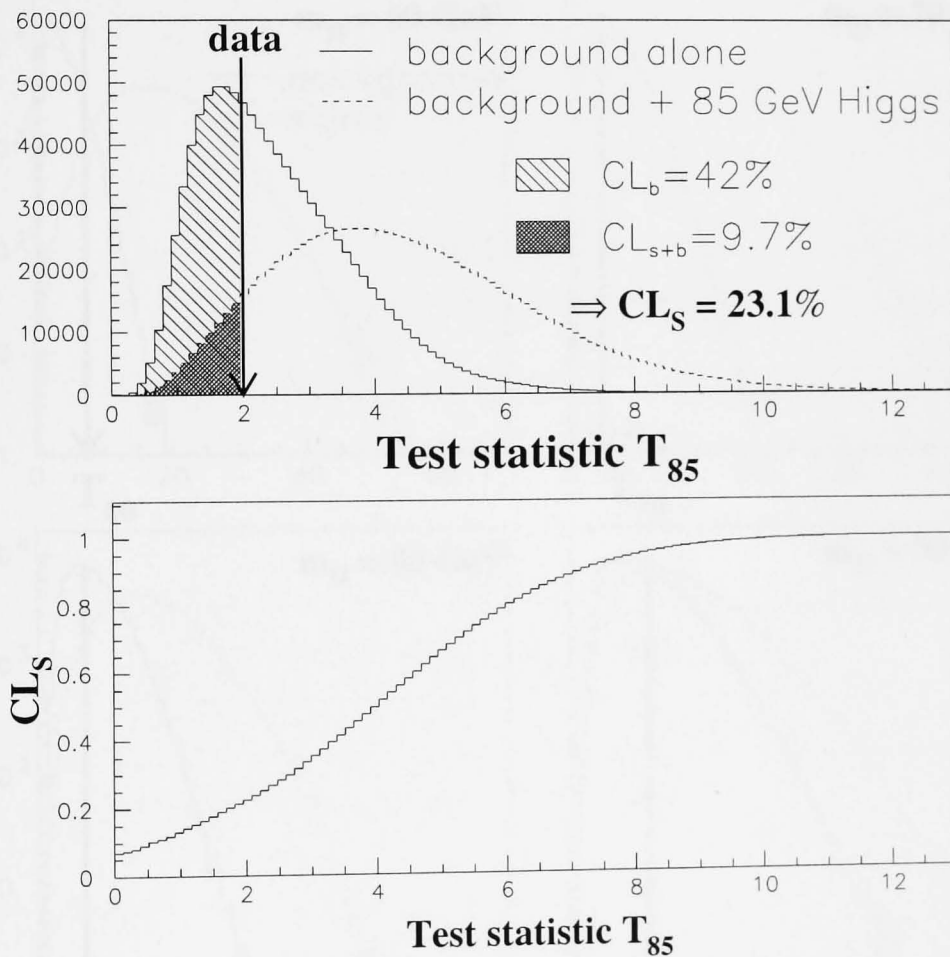

Figure 6.8: The upper plot shows the distribution of test statistic T_{85} for background and 85 GeV/c^2 Higgs signal, with the real data result indicated by an arrow. The lower plot shows the derived value of CL_s as a function of T_{85}.

Overlap between the two alternatives is relatively large because of the low signal cross-section. It is therefore unlikely that we would be able to distinguish between 85 GeV/c^2 Higgs signal and background from this experiment alone.

The distribution of T for 1 million simulated experiments optimised at a number of Higgs mass values are shown in figure 6.9, with the actual data result again indicated by an arrow.
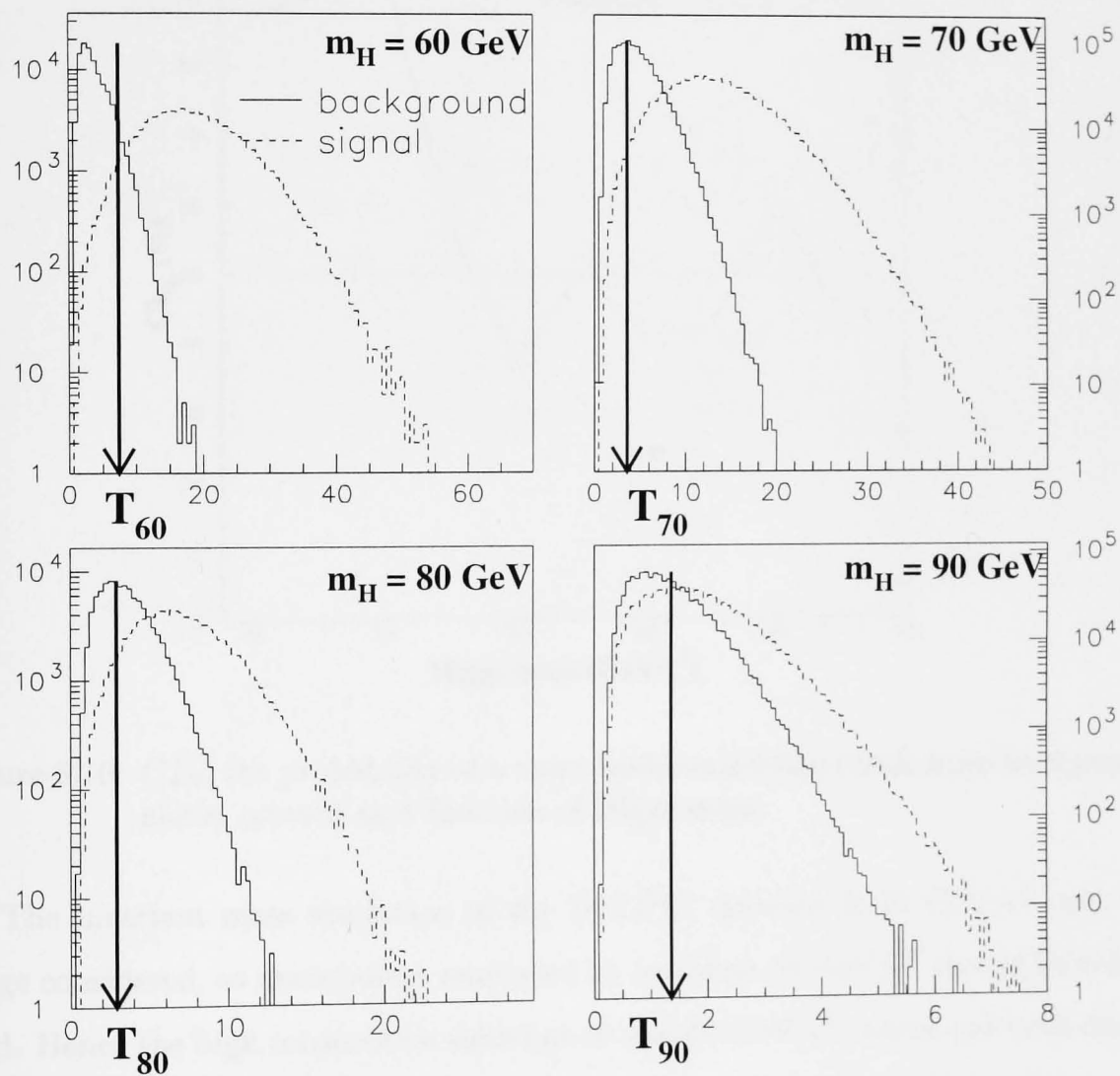
80

Figure 6.9: Expected T distributions from background (solid) and signal (dashed histogram) for $m_H = 60$, 70, 80 and 90 GeV/c^2. An arrow indicates the result from real data.

To check compatibility with background, CL_b was plotted as a function of Higgs mass in figure 6.10. The points are widely distributed; were each point independent then their distribution would be flat, but they are not independent since they all consider the same data sample.
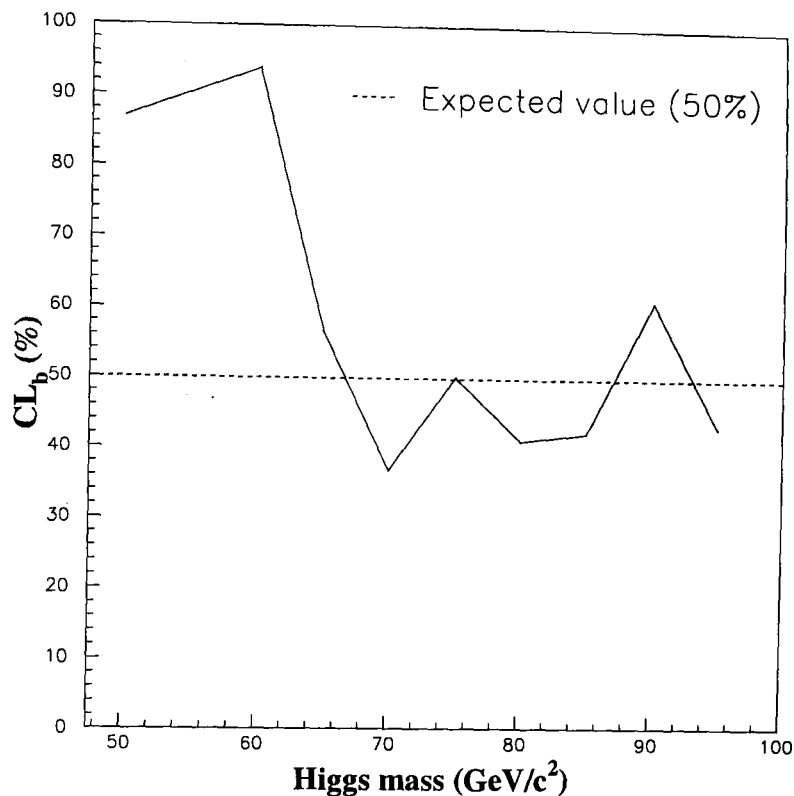

Figure 6.10: CL_b, the probability of a more background-like result from background alone, plotted as a function of Higgs mass.

The invariant mass resolution of the DELPHI detector is 10 GeV/c^2 over the range considered, so mass points separated by less than 10 GeV/c^2 should be correlated. Hence the high consecutive values at 50 and 60 GeV/c^2, which are both due in a large part to one signal like event in data, shown in figure 6.12. This event is also the single remaining candidate for these two mass points in the counting method of § 6.2.2.

Analysis results are summarised in figure 6.11, where observed (solid line) and expected (thin line) CL_s are plotted as a function of Higgs mass. The light shaded area shows the 90% range for CL_s as predicted from background alone. This should be read vertically; for example at $m_H = 70$ GeV/c^2, one expects 90% of observed CL_s to lie in the range 2.3–30. Reading the band horizontally shows the dependence

of the final limit on the observed event topology; the 95% CL limit could (and very nearly does) vary by as much as 20 GeV/c^2.

The dark shaded band represents $\pm 1\sigma$ contours for the systematic uncertainty, as detailed in § 6.5.
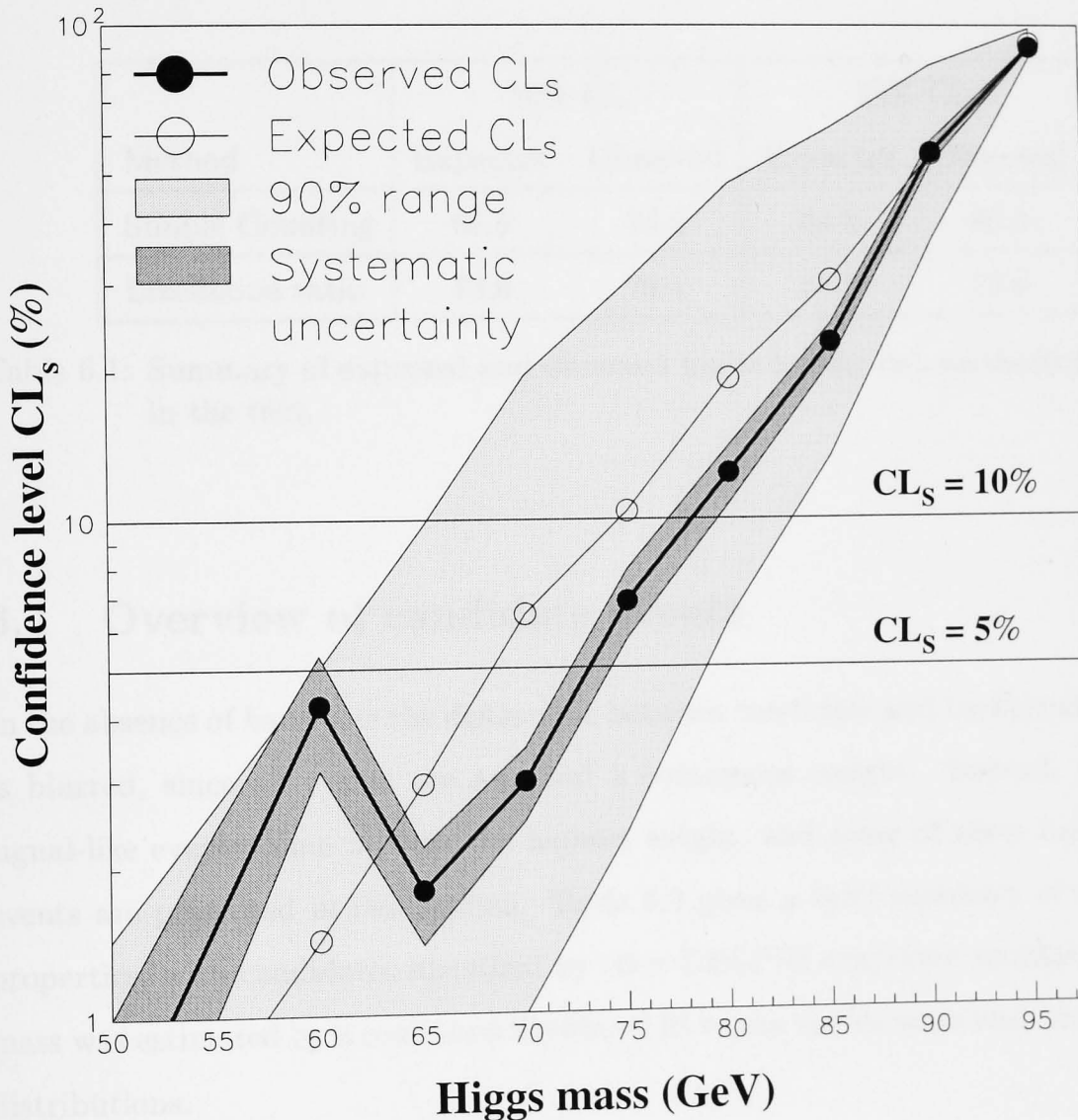
Figure 6.11: Summary of expected (thin line) and observed (solid line) limits for the likelihood ratio method. The light shaded band represents a 90% CL range for the observed limit, as explained in the text. The dark shaded band shows $\pm 1\sigma$ contours for the systematic error in the observed confidence level, explained in § 6.5.

The low mass candidate shown in figure 6.12 threatens to spoil the 95% CL limit for the likelihood ratio method. It is most compatible with a Higgs mass in the range 50–60 GeV/c^2, so that intermediate mass points around 60 GeV would probably show CL_s rising briefly above 5%.

Comparing figure 6.11 to the corresponding figures 6.4 and 6.5 for exclusion by event counting, the advantages of the likelihood ratio approach are obvious. The expected 90% and 95% CL limits on m_H from simple counting are 68.5 GeV/c^2 and 64.0 GeV/c^2 respectively, while the likelihood ratio gives 74.6 GeV/c^2 and 68.5 GeV/c^2. Expected and observed results for the two methods are summarised in table 6.1.

Method	90% CL		95% CL	
	Expected	Observed	Expected	Observed
Simple Counting	68.5	74.0	64.0	60.5
Likelihood ratio	74.6	78.1	68.5	73.0

Table 6.1: Summary of expected and observed limits for the two methods described in the text.

6.4 Overview of candidate events

In the absence of hard cuts the distinction between candidate and background events is blurred, since all events are awarded a continuous weight. Instead, the most signal-like events come in with the highest weight, and some of these high weight events are presented in this section. Table 6.2 gives a brief summary of the event properties, with candidates identified by their DELPHI run/event numbers. Fitted mass was estimated by a combined likelihood fit to the visible mass and acollinearity distributions.
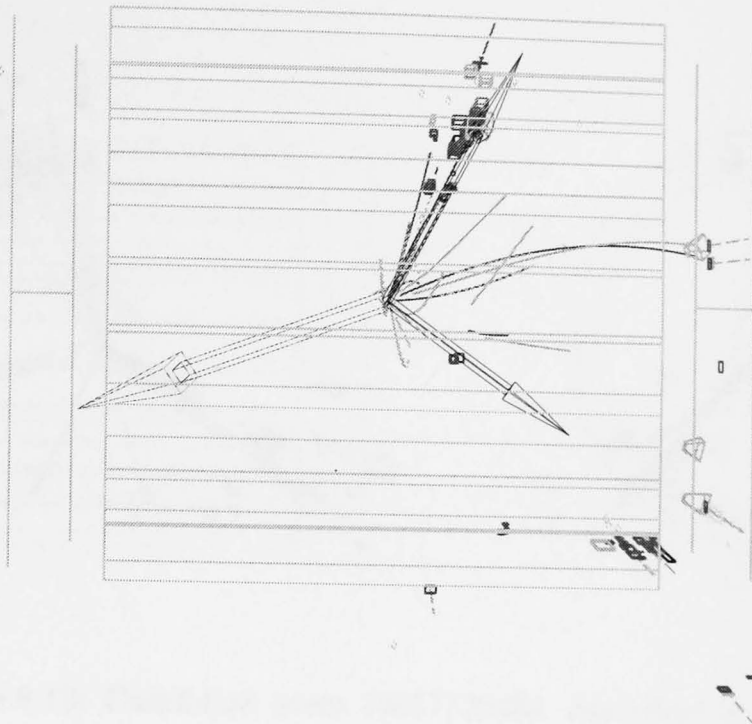
Figure 6.12: Candidate event 79694/11307, described in table 6.2. The HPC sub-detector is shown in the barrel, flanked on either side by the FEMC calorimeters.

Candidate 79694/11307: fitted mass $= 58 \pm 8 \, \text{GeV}/c^2$

The first candidate is responsible for the jump in CL_s at 60 GeV/c^2 observed in figure 6.11. Scanning the event, it appears to be a radiative return event with one jet (pointing downwards on the plot) angled towards the weak 40° region. Energy lost from this jet pulls the missing momentum off beam axis and thus makes the event a candidate, with kinematic factors overcoming a weak BTAG value.

Candidate 79817/20484: fitted mass $= 89 \pm 12 \, \text{GeV}/c^2$

Again, a poorly measured jet around the 40° region contributes to the missing energy in this event, which is also likely to be a radiative Z^0.

Candidate 80251/10557: fitted mass $= 84 \pm 12 \, \text{GeV}/c^2$

A weak jet in the forward region gives this event the kinematic properties of a Higgs candidate. The BTAG value is not particularly significant.
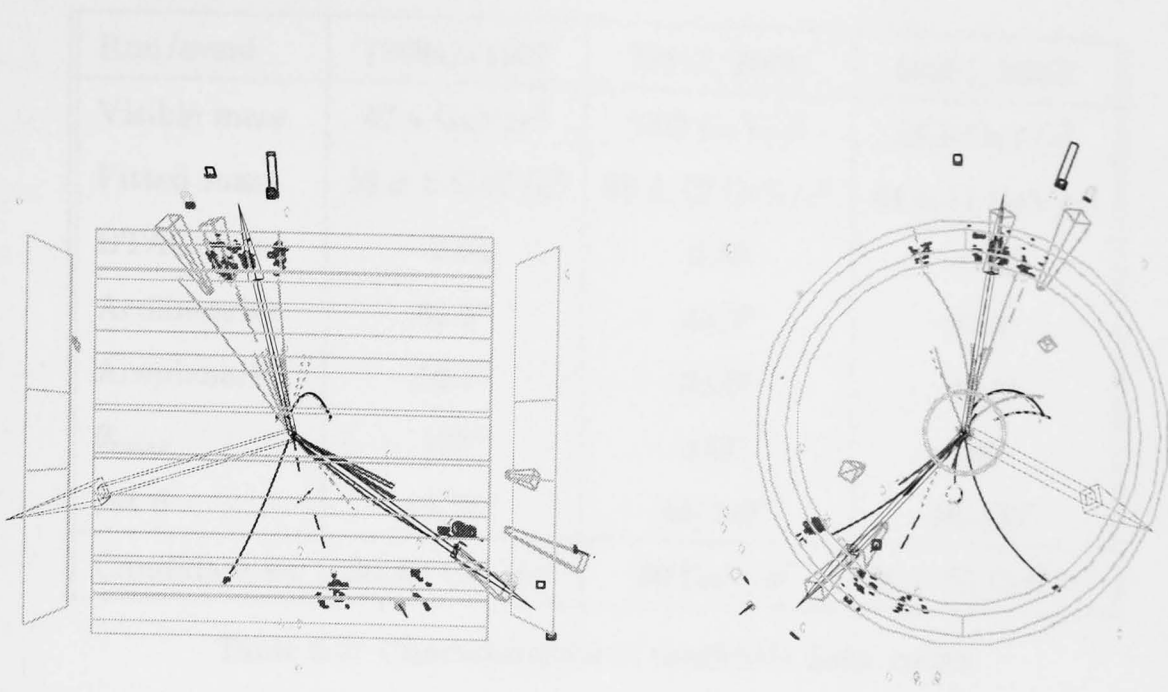
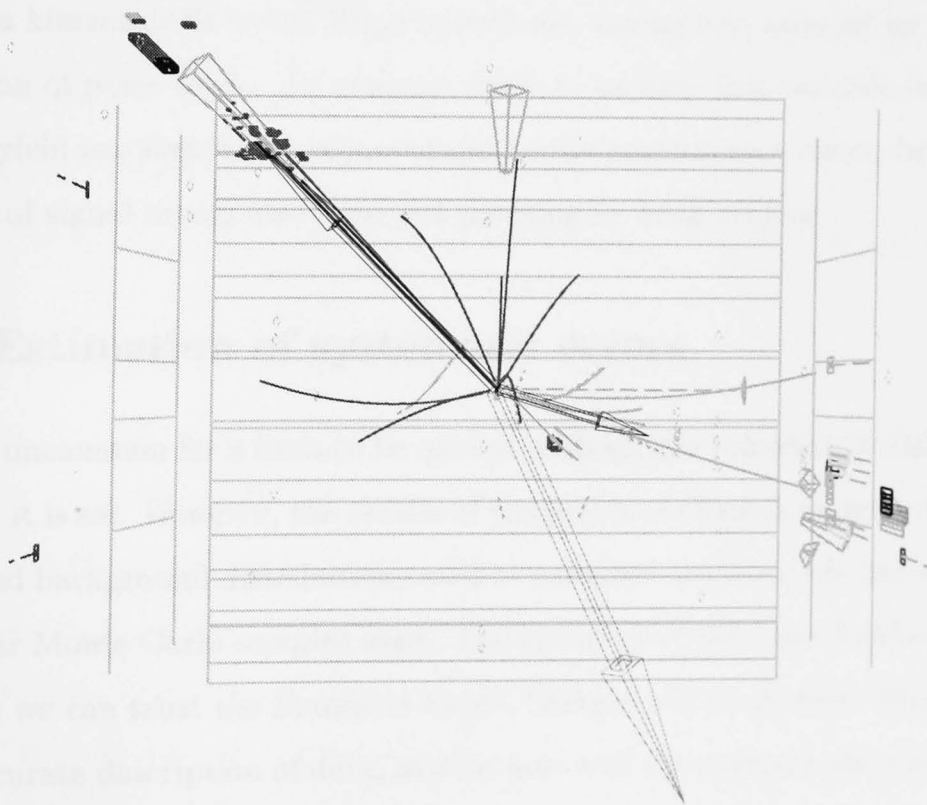Figure 6.13: Candidate event 79817/20484, described in table 6.2.

Figure 6.14: Candidate event 80251/10557, described in table 6.2.

Run/event	79694/11307	79817/20484	80251/10557
Visible mass	47.4 GeV/c^2	72.8 GeV/c^2	68.0 GeV/c^2
Fitted mass	58 ± 8 GeV/c^2	89 ± 12 GeV/c^2	84 ± 11 GeV/c^2
BTAG value	-2.04	0.80	-0.02
Acolinearity	81.3°	43.3°	37.4°
Acoplanarity	56.1°	33.2°	48.8°
θ_{miss}	125°	143°	96°
Jet θ	43, 73°	44, 103°	18, 133°
Candidate for	50, 60 GeV/c^2	80 GeV/c^2	80 − 95 GeV/c^2

Table 6.2: Characteristics of candidate data events.

Summary of candidates

Despite sharing the kinematic properties of the Higgs signal, all candidate events have jets pointing towards weak regions of the DELPHI detector. This suggests that the analysis might be improved by including a new discriminating variable, such as a kinematic fit to the Higgs hypothesis, taking into account jet resolution as a function of polar angle. An attempt made to include this variable in the analysis did not yield any significant improvement to the performance curve, because a large fraction of signal events also have jets pointing to weak regions.

6.5 Estimation of systematic errors

It is not uncommon for a limit to be quoted without any reference to the uncertainty in where it is set. However, the results of the previous chapter make it clear that the signal and background distributions used to calculate the limit are dependent on the particular Monte Carlo samples used. The accuracy of the limit further depends on how well we can trust the Standard Model background predictions from simulation as an accurate description of data, and on how well the detector simulation matches the real detector performance. The term "systematic error" is used rather freely in particle physics, but in general any quantity of influence for which we do not know the exact value is a source of systematic error.

Three possible sources of systematic uncertainty are investigated here: those arising from finite Monte Carlo statistics; from the errors in reconstruction of event variables, and overall background normalisation. The 75 GeV/c^2 Higgs sample is used to illustrate the analysis, being the closest mass point to the 90 and 95% CL limits.

Uncertainty from finite Monte Carlo samples

Even if the simulated background were 100% accurate, the fact that it is only sampled with a finite number of events leads to an uncertainty which is statistical in nature, dependent on the number of generated events. The split-sample approach allows an estimate of this error by reversing the roles of test and training samples: for the 75 GeV sample this caused a relative 2% shift of CL_s from its central value.

Investigations into changing the number of bins and smoothing the weight histograms shown in figure 6.7 saw the derived confidence level change by no more than 3%. Varying the signal and background efficiencies by their errors within each bin saw CL_s change by a further 2%. CL_b and CL_{s+b} varied by over 10% each, but these changes were correlated so that an upward fluctuation of CL_b was matched by a change in CL_{s+b} and $CL_s = CL_{s+b}/CL_b$ remained stable.

Uncertainty from variable reconstruction

The plots of figure 4.5 show that data and simulated background agree well at the preselection level, after the rescaling of radiative return events. Analysis variables were also plotted for data and simulation from high statistics samples collected at the Z^0 pole in 1997, using the same data acquisition and detector simulation as the high energy samples. Figure 6.15 compares data and Monte Carlo for four important event variables, showing good agreement.

Jet momenta components were each smeared by ± 0.8 GeV/c in the Z^0 peak sample, leading to the improved data-Monte Carlo agreement for event P_x and P_z shown in figure 6.16. The same smearing was applied to jets in the high energy sample and event variables recalculated, with a resultant shift in CL_s of under 1%.
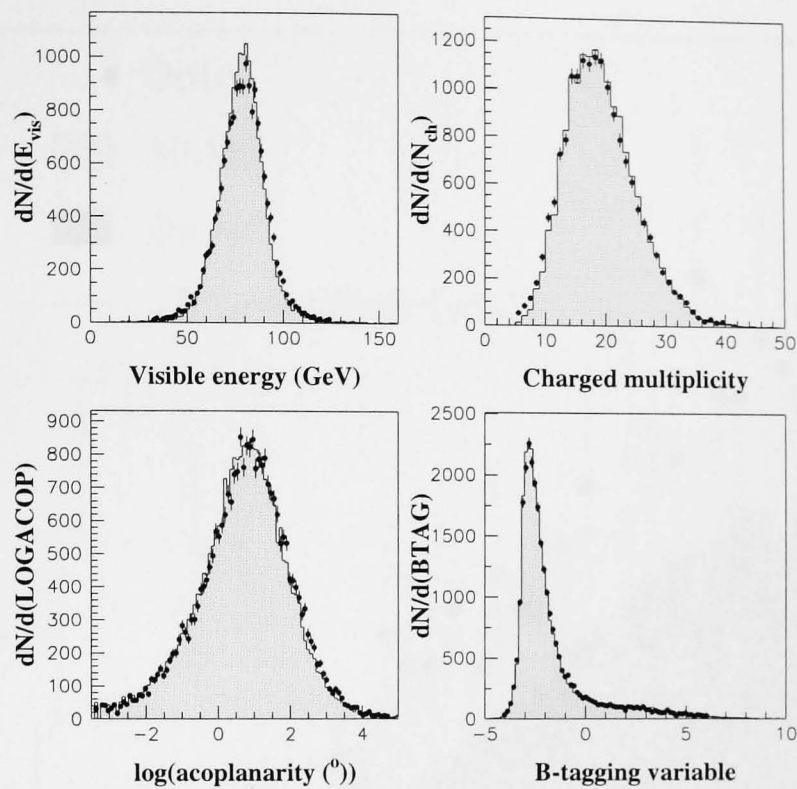
Figure 6.15: Distribution of visible energy, charged multiplicity, acoplanarity and the B-tagging variable from a high statistics Z^0 peak sample. Real data points are compared to shaded Z^0 simulation.
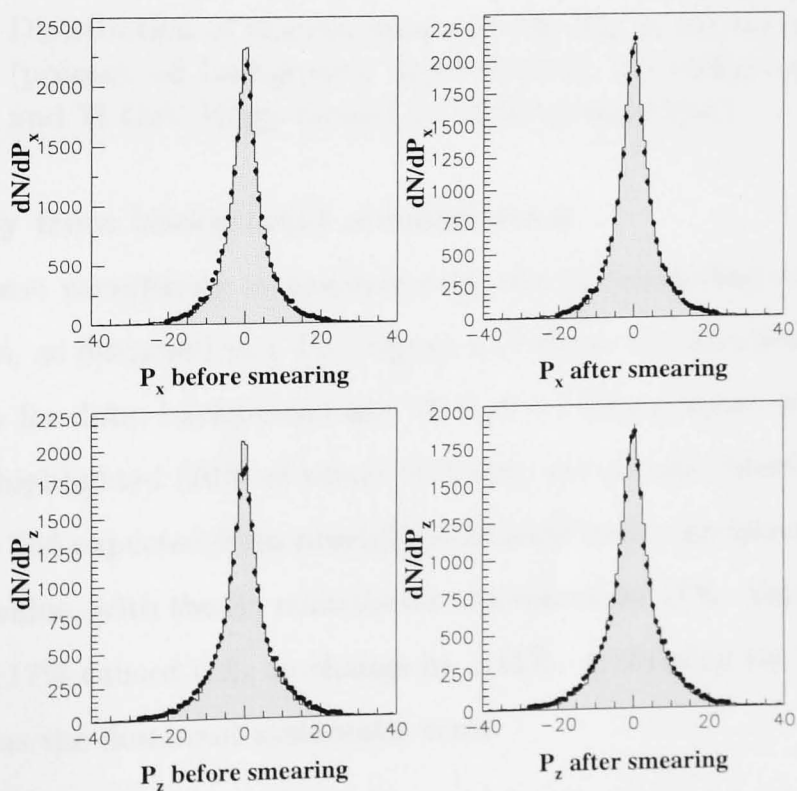

Figure 6.16: P_x and P_z in the Z^0 sample before and after momentum smearing.
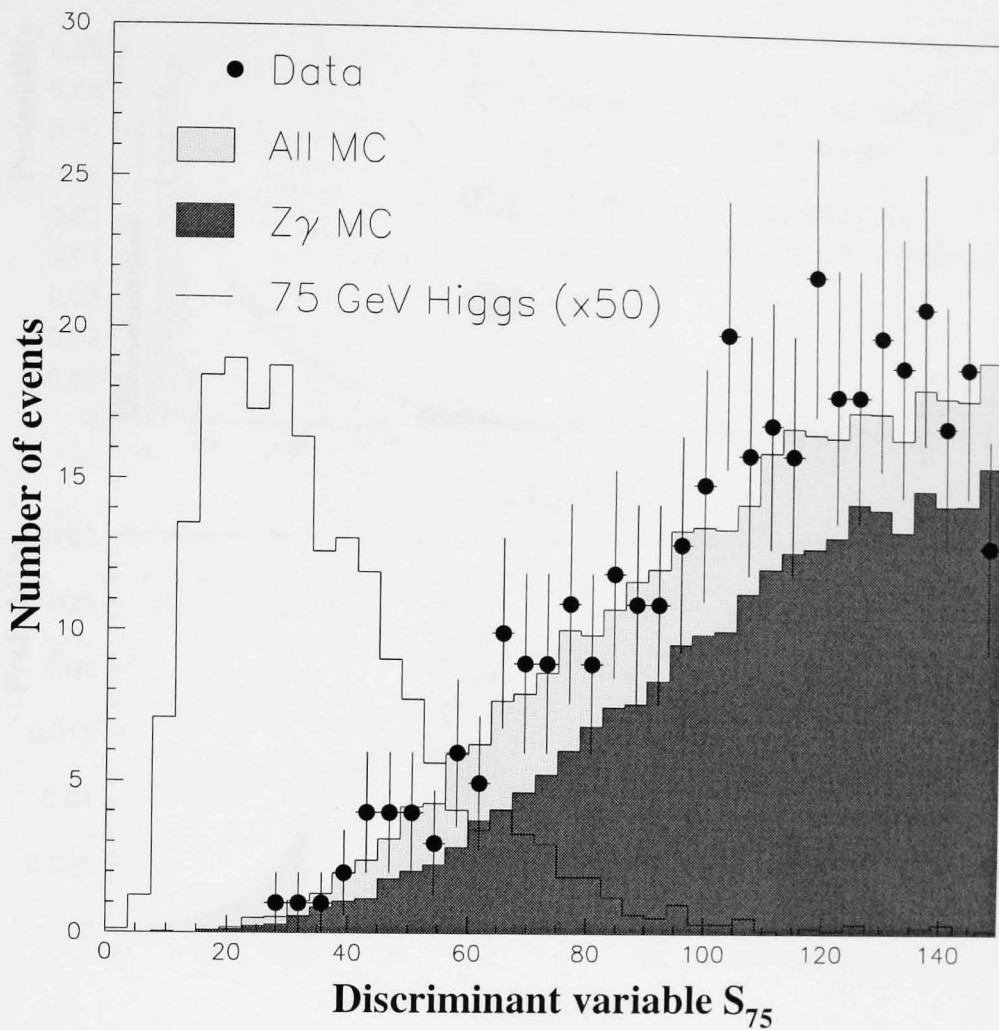
Figure 6.17: Distribution of discriminant variable S_{75} in the signal region for data (points), all background (light shaded), $Z\gamma$ background (dark shaded) and 75 GeV Higgs (scaled by 50 for comparison).

Uncertainty from background normalisation

The systematic uncertainty is dominated by the mis-modelling of ISR in radiative return events, as discussed in § 4.5. Figure 6.17 shows the distribution of S_{75} in the signal region for data, background and 75 GeV/c^2 Higgs signal, with the dominant $Z\gamma$ channel highlighted (70% of total). 377 data events are observed in this region, compared to 356 expected from reweighted Monte Carlo – an increase of 12% on the unweighted value, with the $Z\gamma$ contribution increased by 17%. Varying the $Z\gamma$ background by ±17% caused CL_s to change by ±15%, confirming the $Z\gamma$ normalisation uncertainty as the dominant systematic error.

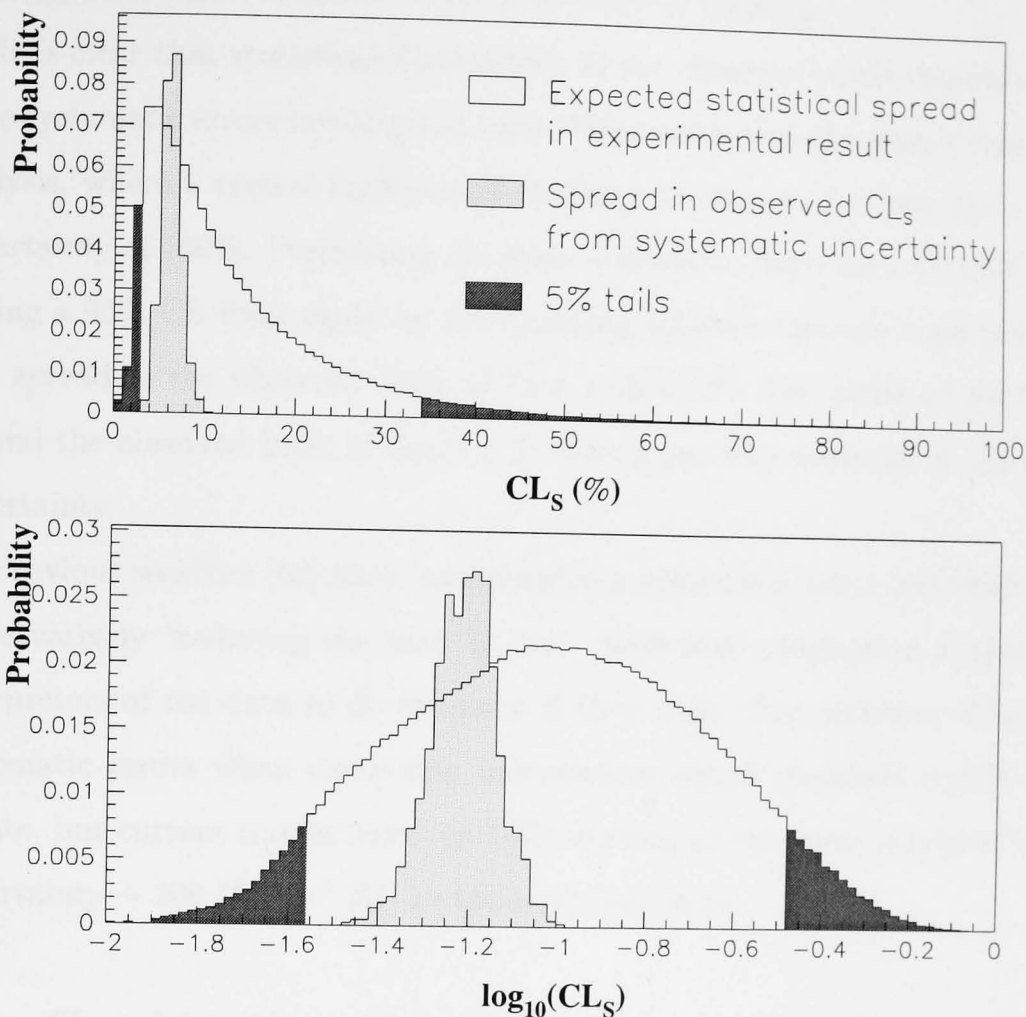Figure 6.18: Statistical and systematic uncertainties in CL_s for a 75 GeV Higgs.

6.5.1 Comparison of systematic and statistical uncertainties

The combined effect of estimated systematic uncertainties on CL_s for a 75 GeV/c^2 Higgs is illustrated in figure 6.18. The open histogram shows the expected spread in CL_s from statistical fluctuation alone. The light shaded histogram shows the variation of the observed value (from $CL_s = 6.6\%$) after taking into account all investigated systematic effects. Dark shaded areas show 5% tails of the CL_s distribution: 10% of random background experiments would expect an observed value of CL_s somewhere in this range.

The skew visible in the upper plot is responsible for a gradual migration of the expected limit from the median value as CL_s decreases, until it eventually lies outside the 90% band shown in figure 6.11. This feature has indeed been observed in combined LEP results [61], and shows the expected value of CL_s to be a poor basis

for comparison with data at low CL_s. The lower plot shows the same distribution for $\log_{10} CL_s$, which is the more natural choice of variable [1].

It is clear that statistical fluctuations in the observed result dominate even the large systematic errors investigated here. The same is true of a simple event counting analysis, where a typical background of about 1.0 expected events has a statistical uncertainty of 100%. Performing the same systematic study for a 70 GeV Higgs and setting a 95% CL limit again by interpolating between the two mass points results in a spread in the observed limit of 73 ± 1 GeV/c^2. The width of the dark band around the observed limit in figure 6.11 represents $\pm 1\sigma$ contours of the systematic uncertainty.

Previous searches [62] have incorporated a systematic error into their results by conservatively "reducing the limit by 1σ". Sufficient information is given here for interpreters of the data to do the same if they wish. The question of how to treat systematic errors when combining independent search channels is still a topic of debate, but current results from the LEP working group quote a typical systematic uncertainty ~ 200 MeV/c^2 [61] in the combined limit.

6.6 Combination of independent search channels

A method has been developed at DELPHI for the combination of independent channels using a likelihood ratio method [63] [2]. This takes mass distributions for signal and background from each channel along with the candidates observed after a tight selection and uses the expected and observed relative likelihood to evaluate a limit. The 95% CL limit set running this program on all of the DELPHI data collected at 183 GeV was 85.7 GeV/c^2, compared to the expected limit of 86.5 GeV/c^2. Table 6.3 gives a summary of the results in each channel used in the combination.

Instead of a complicated likelihood ratio analysis, the results from all channels can simply be added and a limit set from the total number of events observed (using

---

[1]A simple method for combining 2 independent channels (1 and 2) could consider the probability of a more background-like experiment in *both* channels. Confidences then multiply - i.e. $CL_s(1 + 2) = CL_s(1) \cdot CL_s(2)$ - so their logarithms add. Combining many results from identical experiments would eventually yield a normal distribution, by the Central Limit Theorem [45], which suggests $\log CL_s$ as a more "natural" choice.

[2]The channels do not have to be entirely independent; see [64]

Channel	Background	Luminosity	Events	Signal
He^+e^-	$0.68 \pm 0.12 \pm 0.10$	52.3	1	0.26
$H\mu^+\mu^-$	$0.49 \pm 0.06 \pm 0.17$	54.0	2	0.43
$H\nu\bar{\nu}$	$0.50 \pm 0.08 \pm 0.10$	51.6	1	1.25
$Hq\bar{q}$	$3.74 \pm 0.20 \pm 0.18$	54.0	1	5.18
$(h \to q\bar{q})\tau^+\tau^-$	$0.34 \pm 0.07 \pm 0.04$	54.0	0	0.12
$(h \to \tau^+\tau^-)q\bar{q}$	$0.74 \pm 0.09 \pm 0.08$	54.0	1	0.24
total	$6.5 \pm 0.3 \pm 0.4$	-	6	7.48

Table 6.3: Expected background with statistical and systematic errors, integrated luminosity, number of observed events and expected signal in all channels used to produce a mass limit. The number of signal events is given at 85 GeV/c^2.

the PDG formula 5.1). The limit thus obtained is 86.3 ± 0.4 GeV/c^2, with an expected limit of 84.3 ± 0.4 GeV/c^2, where the uncertainty comes from interpolation of the details given for an 85 GeV/c^2 Higgs. As can be seen from this table, the total cross-section is dominated by the hadronic $Hq\bar{q}$ channel. Using this channel alone to perform an exclusion results in an observed 95% CL limit of 88.4 ± 0.3 GeV/c^2 and an expected limit of 83.0 ± 0.5 GeV/c^2. These results are summarised in table 6.4.

Information used	Likelihood ratio: all channels	Simple counting: all channels added	Simple counting: $Hq\bar{q}$ channel only
Expected limit	86.5	84.3 ± 0.4	83.0 ± 0.5
Observed limit	85.7	86.3 ± 0.4	88.4 ± 0.3

Table 6.4: Summary of the expected and observed limits obtained from the DELPHI data using the full likelihood information, simple counting by adding all channels and simple counting in the $Hq\bar{q}$ channel alone.

Examination of table 6.4 confirms that, despite the fact that the likelihood ratio approach gives the best expected limit, the final result depends crucially on the distribution of events observed. Simple counting using the $Hq\bar{q}$ channel alone performs better than the likelihood ratio method *in this case* thanks to a downward

93

fluctuation of background (of 10% significance). This is a fortunate result: one could as often expect to do just as significantly worse from considering the $Hq\bar{q}$ channel alone. The main advantage of the likelihood ratio method for exclusion is to dampen down these fluctuations by including more events and removing the dependence on hard cuts. The likelihood ratio also maximises the probability of discovery – an eventuality which has just been touched upon in this thesis but is covered in more detail elsewhere [61].

The combination of results from all four LEP experiments follows the same procedure, and resulted in an observed limit of 90.1 GeV/c^2, with an expected limit of 89.8 GeV/c^2 at 183 GeV [50]. These results have been updated with the inclusion of data from the 1998 running of LEP2 at 189 GeV to an observed limit of $m_H > 95.2$ GeV/c^2. Preliminary results including the 1999 data taken at 192 and 196 GeV indicate a combined limit of $m_H > 102.6$ GeV/c^2 [61] [3].

---

[3] At LEP2 the empirical formula predicting an exclusion limit just 2 GeV below the kinematic limit at $\sqrt{s} - 93$ GeV appears to hold rather well.

Chapter 7

Conclusions

A search has been performed for the Standard Model Higgs boson, using 51.59 pb^{-1} of data collected by the DELPHI detector at a LEP collision centre-of-mass energy of 183 GeV. The Higgs production mechanism $e^+e^- \to Z^* \to HZ^0$ was investigated, where the Higgs decays to b quarks and the Z to neutrinos. Different analysis techniques were presented and compared, with a Likelihood Ratio method promoted as the optimal way to perform a search.

In the absence of any departure of data from Standard Model background predictions, the Likelihood Ratio method was used to set a 95% confidence level lower limit on the Higgs mass of $m_H > 73.0$ GeV/c^2, using the neutrino channel alone. When combined with searches for other Z decay channels at 183 GeV, this contributed to the combined DELPHI 95% confidence level limit of $m_H > 85.7$ GeV/c^2.

These limits have since been superseded by higher energy data, with a current limit of $m_H > 102.6$ GeV/c^2 from the combination of all four LEP experiments.

Future prospects for Higgs searches

Recent studies have shown [65] that 200 pb^{-1} of data collected by each of the four LEP experiments at 200 GeV would bring the 95% confidence level exclusion limit to saturation at 109.1 GeV/c^2, with a probability greater than 50% of discovering a Higgs boson with m_H up to the kinematic limit of 108.8 GeV/c^2.

When LEP goes out of commission for the installation of the LHC in the year 2000, the mantle passes to the upgraded CDF and D0 experiments at Fermilab. Predicted exclusion and discovery limits at the Tevatron as a function of Higgs mass and integrated luminosity are shown in figure 7.1. The search will be extended up to 1 TeV once the LHC comes on-line in 2005 [66].
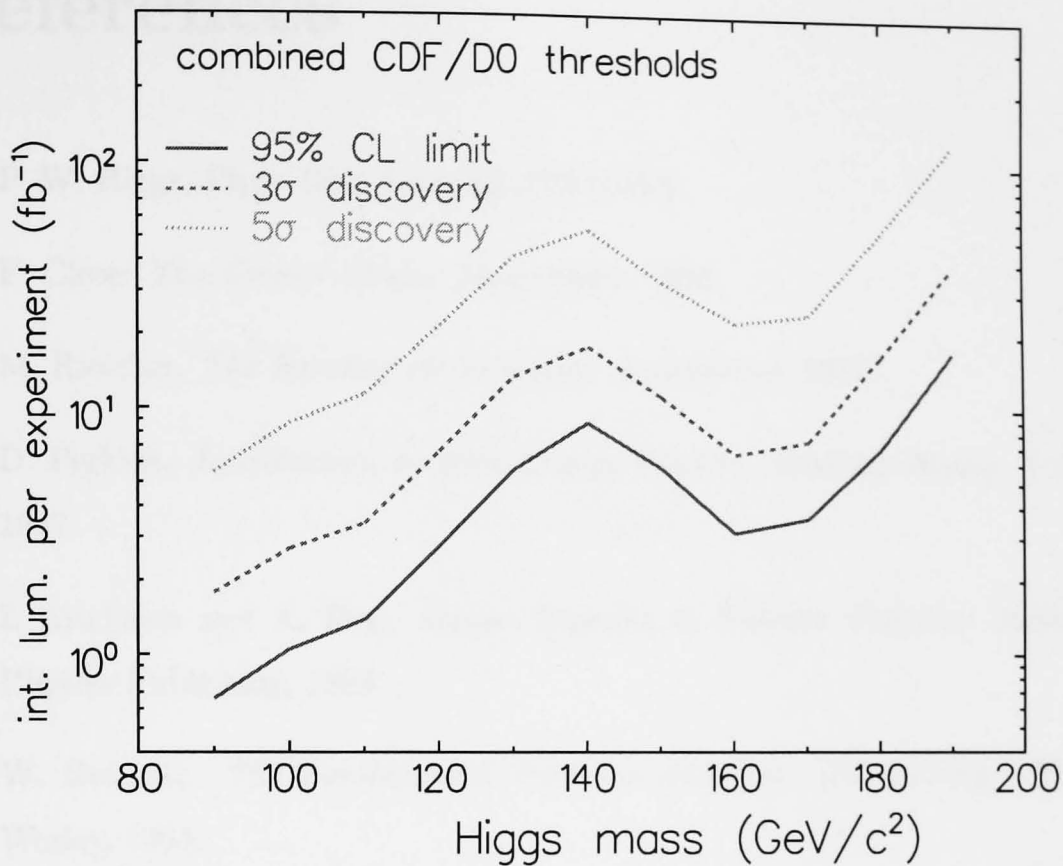
Figure 7.1: Luminosity required to achieve 95% confidence level exclusion, 3σ evidence and 5σ discovery at the Tevatron as a function of Higgs mass

Figure 1.7 shows that fits to electroweak precision data favour a low mass Higgs. Should the Higgs prove to be beyond the range of LEP2 and the Tevatron, then the prospects for its discovery at the LHC look promising [66]. If the Higgs boson reveals itself then the electroweak symmetry breaking sector of the Standard Model can be tested directly for the first time. However, should the Higgs prove more elusive, then the theoretical and experimental task of finding an alternative explanation for mass generation within or beyond the Standard Model could prove the most challenging yet.

References

[1] P. W. Higgs, Phys. Rev. Lett. **12**, 508 (1964).

[2] F. Close, *The Cosmic Onion*, Heinemann, 1983.

[3] M. Riordan, *The Hunting of the Quark*, Touchstone, 1987.

[4] D. Perkins, *Introduction to High Energy Physics*, Addison-Wesley, 3 edition, 1987.

[5] I. Aitchison and A. Hey, *Gauge Theories in Particle Physics*, Institute of Physics Publishing, 1993.

[6] W. Rolnick, *The Fundamental Particles and their Interactions*, Addison-Wesley, 1994.

[7] D. Griffiths, *Introduction to Elementary Particles*, Wiley, 1987.

[8] F. Halzen and A. Martin, *Quarks and Leptons: an Introductory Course in Modern Particle Physics*, Wiley, 1984.

[9] H. Goldstein, *Classical Mechanics*, Addison-Wesley, 1980.

[10] J. Schwinger, Ann. Phys. **2**, 407 (1957).

[11] J. Schwinger, Phys. Rev **125**, 397 (1962).

[12] Y. Nambu, Phys. Rev. Lett. **4**, 380 (1960).

[13] P. W. Anderson, Phys. Rev **110**, 827 (1958).

[14] J. Goldstone, Nuovo Cimento **19**, 154 (1961).

[15] T. W. B. Kibble, Phys. Rev. **155**, 1554 (1967).

[16] S.L. Glashow, Nucl. Phys. **22**, 579 (1961).

[17] S. Weinberg, Phys. Rev. Lett. **19**, 1264 (1967).

[18] A. Salam, J.C. Ward, Phys. Lett. **13**, 168 (1964).

[19] G. 't Hooft, Nucl. Phys. **33**, 173 (1971).

[20] J. Ellis et al., Nucl. Phys. **B106**, 292 (1976).

[21] Particle Data Group, The European Physical Journal **C3** (1998).

[22] G. Altarelli, T. Sjöstrand and F. Zwirner, Physics at LEP2, Yellow report 96-01, CERN, 1996.

[23] B. A. Kniehl, (1996), hep-ph/9610500.

[24] S. Weinberg, Phys. Rev. Lett. **36**, 294 (1976).

[25] J. A. Casas, J. R. Espinosa and M. Quiros, Phys. Lett. **B342**, 171 (1995).

[26] LEP Electroweak Working Group, A combination of preliminary electroweak measurements and constraints on the standard model, CERN-EP/99-15, 1999.

[27] D. Bardin et al., Phys. Lett. **B255**, 290 (1991).

[28] M. Davier and A. Hocker, Phys. Lett. **B419**, 419 (1998).

[29] DELPHI Collaboration, DELPHI Technical Proposal, Technical Report CERN-LEPC/83-3, CERN, 1983.

[30] DELPHI Collaboration, Nucl. Instrum. Meth. **A303**, 233 (1991).

[31] DELPHI Collaboration, Nucl. Instrum. Meth. **A378**, 57 (1996).

[32] V. Chabaud et al., Alignment of the DELPHI vertex detector, DELPHI 95-177 MVX 10, CERN, 1995.

[33] R. Brenner, Nucl. Instrum. Meth. **A386**, 6 (1997).

[34] P. Delpierre et al., Nucl. Instrum. Meth. **A386**, 11 (1997).

[35] T. J. Adye et al., Nucl. Instrum. Meth. **A349**, 160 (1994).

[36] V. Bocci et al., Nucl. Instrum. Meth. **A362**, 361 (1995).

[37] P. Charpentier et al., The DELPHI Data Acquisition System, in *Proc. Int. Conf. on Computing in High Energy Physics*, edited by Y. Watase and F. Abe, page 643, Tokyo, 1991, Universal Academy Press.

[38] T. Sjöstrand, (1995), hep-ph/9508391.

[39] T. Sjöstrand, Computer Physics Commun. **82**, 74 (1994).

[40] G. Marchesini et al., (1996), hep-ph/9607393.

[41] DELSIM reference manual, 1989, DELPHI 89-68/PROG 143.

[42] DELPHI Collaboration, *DELPHI Data Analysis Program (DELANA) User's Guide*.

[43] M. Kendall, *The Advanced Theory of Statistics*, Charles Griffin, 4 edition, 1983.

[44] W. T. Eadie et al, *Statistical Methods in Experimental Physics*, North Holland Publishing, 1971.

[45] R. J. Barlow, *Statistics: A Guide to the use of Statistical Methods in the Physical Sciences*, Wiley, 1989.

[46] A. L. Read, Optimal statistical analysis of search results based on the likelihood ratio, DELPHI 97-158 PHYS 737, 1997.

[47] R. D. Cousins, Why isn't every physicist a Bayesian?, UCLA-HEP-94-005, 1994.

[48] G. D'Agostini, Bayesian reasoning versus conventional statistics in high-energy physics, physics/9811046, 1998.

[49] G. D'Agostini, Probability and measurement uncertainty in physics: a Bayesian primer, hep-ph/9512295, 1995.

[50] P. Bock et al., LEP Higgs Working Group, (1998), CERN-EP/99-060.

[51] A. L. Read, Strategy for discovery in combining experiments, LEP Higgs working group internal note, 1998.

[52] S. Andringa et al., ISR in hadronic events at LEP: generators versus data, DELPHI 99-53 PHYS 824, 1999.

[53] W. de. Boer and C. F. Vollmer, Comparison of SPYTHIA and KORALZ at 183 GeV, DELPHI 98-10 PHYS 761, 1998.

[54] R. Keranen, Private communication.

[55] K. Hultqvist et al., Use of discriminant analyses in the H$\nu\bar{\nu}$ channel at $\sqrt{s} =$ 183 GeV, DELPHI 98-25 PHYS 767, 1998.

[56] T. Sjöstrand, Current updated notes describing new features in PYTHIA, **1999**, http://www.thep.lu.se/torbjorn/pythia.html.

[57] G. Borisov and C. Mariotti, Performance of b-tagging in DELPHI at LEP2, DAPNIA/Spp Report 97-06 and INFN/ISS Report 97-03.

[58] S. Catani et al., Phys. Lett. **B269**, 432 (1991).

[59] R. Brun and D. Lienart., HBOOK users guide (version 4), 1973, CERN program library, Y250.

[60] LEP working group for Higgs boson searches, Lower bound for the Standard Model Higgs boson mass from combining the results of the four LEP experiments, CERN-EP/98-046, 1998.

[61] P.Igo-Kemenes et al., LEP Higgs Working Group status report, 1999, LEPC meeting.

[62] DELPHI Collaboration, Phys. Lett. B **420**, 140 (1998), CERN-PPR/97-145.

[63] A. L. Read, Optimal Statistical Analysis of Search Results based on the Likelihood Ratio, DELPHI 95-140/PHYS 565, 1997.

[64] D. A. Evans and W. H. Barkas, Nucl. Instrum. Meth. **56**, 289 (1967).

[65] E. Gross, A. L. Read and D. Lellouch, Prospects for the Higgs Boson Search in e$^+$e$^-$ Collisions at LEP 200, in *Proc. Rencontres de Physique de la Valee' d'Aoste, La Thuille*, 1998.

[66] F. Pauss and M. Dittmar, Proceedings of the ASI summer school, 1998, PR-98-09.